CHAPTER 6

Printed Open-channel Microfluidics

The following three chapters in this dissertation presents some applications of surfaces with patterned wettability in fabricating microfluidic devices. This chapter details a novel maskless fabrication method developed to produce inexpensive open-channel microfluidic devices on fluorinated paper by directly depositing wettable material. This chapter combines an excerpt from a published article in *Advanced Functional Materials*,[248] co-authored with Dr. Chao Li, and an unpublished manuscript demonstrating an application of the printed devices for the on-chip lysis and colorimetric detection of trace contamination of water by *E. coli* bacteria, co-authored with Sarah Snyder.

6.1   Introduction

Paper has recently emerged as a promising materials platform for microfluidic devices due to its low cost, easy disposal, high surface area, capillary-based wetting, flexibility, and compatibility with a wide range of patterning and printing techniques.[249] Since the first report of using paper as a base material in microfluidics by Whitesides *et al.* in 2007,[250] a new era of paper-based microfluidic devices has arisen.[251–255] The ability to pattern wetting/non-wetting channels on paper has allowed multiplexed small-volume fluid control, both in two-dimensional lateral flow on a single surface,[256–261] and three-dimensional flow on stacked layers connected through pores.[262–267]

Generally, fluidic channels introduced on paper surfaces are composed of wettable domains bounded by non-wettable domains or air gaps.[268–271] In most cases, paper-based microfluidic channels have been developed to contain only water or aqueous solutions.[272] Few reported techniques used for generating patterned wettability on paper result in devices compatible with even a limited number of non-aqueous liquids.[273–275] Furthermore, the wettable channels in the paper-based microfluidic systems reported thus far show no selective wettability with liquids possessing different surface tensions and/or polarities.

In other words, all liquids wet these fluidic channels. Overall, there is no established technique that allows for the selective generation of all four "extreme wettabilities"[276,277] on paper-based microfluidic channels; that is, the four possible combinations of wetting of oil (oleophilic – OL or oleophobic – OP) and water (hydrophilic – HL and hydrophobic – HP) on a surface. The four

extreme wettabilities are: HP/OP (omniphobic, all liquids non-wetting), HP/OL (water non-wetting, oil wetting), HL/OP (water wetting, oil non-wetting), and HL/OL (omniphilic, all liquids wetting), as shown in Figure 6.1a.

In this work, we have developed a method of generating omniphobic fluorinated paper surfaces that are resistant to wetting by a broad range of liquids, including numerous low surface tension solvents. Further, we also developed two methodologies to introduce channels which are selectively wettable by liquids with varying surface tension and polarity on a paper surface. The first utilized masked oxygen plasma to selectively remove the fluorinated modifier from the paper to tune the wettability of the channel. This technique allowed us to realize the four extreme wettabilities with oil and water, as discussed above, on paper surfaces (Figure 6.1a). Such selective extreme wettabilities of fluidic channels, combined with improved fluidic control, made several new applications of paper-based microfluidic devices possible. The second was a maskless direct-printing technique developed to address the inconvenience of fabricating or purchasing masks in the first method. With the printing technique, we were able to fabricate HL/OL and HP/OL channels, depending on the material deposited.

6.1.1 Wettability

There are two key requirements for open-channel microfluidic devices defined by domains of contrasting wettability. Firstly, a highly non-wettable background, which has high advancing contact angles with the liquid, so that it may be effectively confined. High receding angles also help recover from overflow into the background, but are not strictly required. Secondly, the channels need to be highly wettable by the target liquid. In multi-phase immiscible liquid flows, such as those used in flow-focusing droplet generation, the target liquid may need to preferentially wet selected channel areas.

As described in Section 1.2, the engineering of liquid-repellent surfaces typically involves the manipulation of two key surface parameters: surface energy and roughness. These may be tuned to either enhance the non-wettability of the background, or the wettability of the channels.

Typically, the background needs to maintain all liquids in the system in a robust Cassie-Baxter state, maximizing θ_a and θ_r, such that the liquids may be effectively contained at high flow rates in the channel, as well as extended durations of usage. Hierarchically textured, re-entrant, low surface energy materials are ideal for making superomniphobic substrates for this purpose (see Section 1.2).

The liquid flowing within the channel should be in the fully wetted Wenzel state. The inherent contact angle of the liquid on the material of the channel must be < 90 °, so that any roughness enhances wetting. The wetting length of a liquid in a capillary tube is described by Washburn's equation as follows[278]

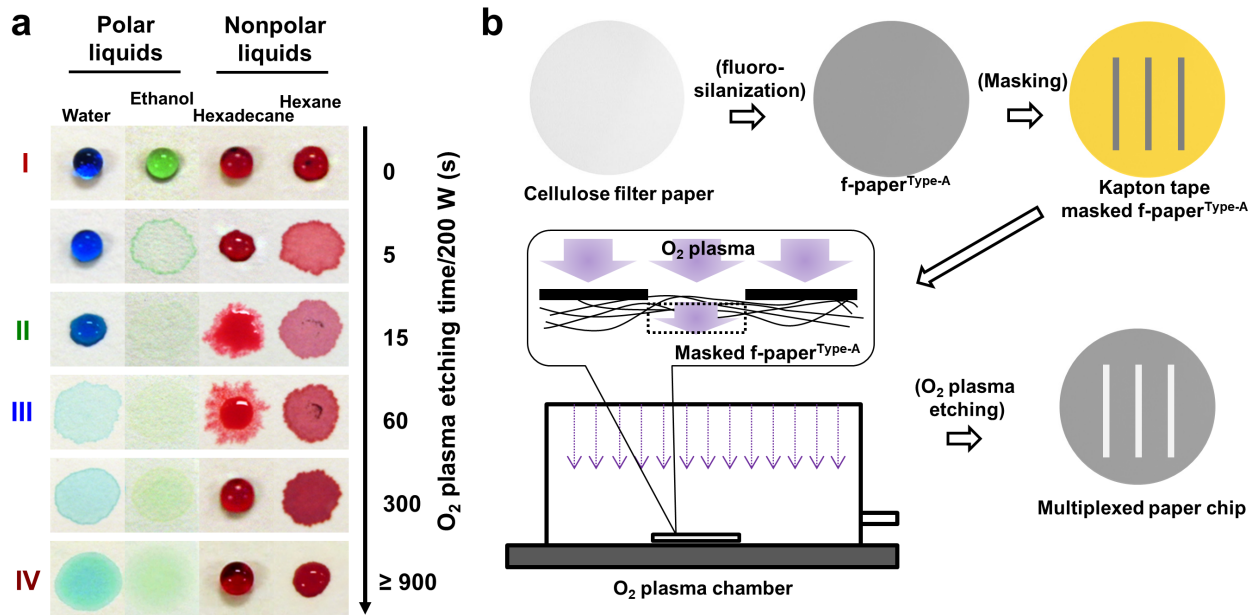**Figure 6.1:** (*a*) An illustration of the changes in wettability of an omniphobic paper (fluoro-paper A) surface on exposure to O_2 plasma for varying times. Short exposure time yields a hydrophobic and oleophilic surface. Further O_2 plasma exposure yields an omniphilic surface. Extended etching eventually yields a hydrophilic and oleophobic surface due to re-deposition of some of the fluorinated silane. Thus, it is possible to systematically transition between surfaces with all four extreme wettabilities by simply changing the O_2 plasma exposure time. (*b*) Schematic illustration of the procedure to make a wettability-patterned paper device by selective O_2 plasma etching of fluoro-paper A.

$$L^2 = \frac{\gamma D t \cos \theta}{4\eta} \tag{6.1}$$

where L is the wetting length, γ_{LV} is the liquid surface tension, D is the capillary diameter, θ is the intrinsic contact angle, and η is the viscosity of the liquid.

If the capillary tube were to be fully wettable, or "omniphilic" ($\theta = 0°$), L and the average wetting velocity of capillary flow (L/t) for the seven test liquids should increase with increasing surface-tension to viscosity ratio (γ_{LV} / η) as follows: acetone > water > hexane > chloroform > dimethylformamide > ethanol > hexadecane. However, on most real surfaces, a finite resistance to wetting exists, and there exists a contact angle typically proportional to the γ_{LV}. Water, with its anomalously high surface tension, tends to exhibit the slowest wetting velocities and lowest wetting lengths in partially wettable channels.

In multi-phase flows, it is usually desirable to enhance the selective wetting of one phase in defined areas of the channel to enhance the functionality of the device. As described in the introduction, our fabrication techniques can enable this with many combinations of immiscible liquids.

6.2 Fabrication of Omniphobic Paper Background

6.2.1 Paper Functionalization

Paper, made from cellulose fibers, is both textured and inherently hydrophilic and therefore must be chemically modified to prevent wetting. With fluoro-silanization, it is possible to produce omniphobic, or even superomniphobic cellulose paper that resists wicking or spreading of most liquids, including low surface tension solvents. Careful selection of paper texture and pre-processing yields a broad range of wettability and robustness of the composite interface with water and oil. The substrates were either cellulose filter papers (GE Life Sciences, Whatman Grade 3, pore size 6 m, thickness 390 μm) or cellulose copy paper (Boise X-9 Multiuse OX9001, OfficeMax). Fluorosilanes, (heptadecafluoro-1,1,2,2-tetrahydrodecyl trichlorosilane and heptadecafluoro-1,1,2,2-tetrahydrodecyl triethoxysilane), were purchased from Gelest. Asahiklin AK-225 (dichloropentafluoropropane) was purchased from SPI Supplies. All of the materials and reagents were used as received. See Table 6.1 and Figure 6.2 for a summary of the three types of fluoro-paper developed.

For fluoro-paper A, each batch of cellulose filter papers was treated with 400 μL of trichlorosilane per 400 cm^2 (an excess quantity) by vapor phase deposition in a vacuum oven (Precision Scientific, 50 °C, < 5 mmHg) for 18 hours (Figure 6.2, fluoro-paper A). After fluorosilanization, the paper was soaked in 250 mL AK-225 for 24 hours to remove the unreacted fluorosilanes. The re-entrant texture of the cellulose fibers, combined with the low surface energy of the fluoro-silane, yielded a porous omniphobic substrate, referred to as fluoro-paper A (Table 6.1, 6.2). The apparent advancing contact angle (θ_a^*) of water on fluoro-paper A was > 160°, and the robustness parameters A^*_{water} = 24.6 and $A^*_{hexadecane}$ = 4.5, indicated that both water and hexadecane were in a stable, non-wetted, Cassie-Baxter state (see Methods for details). In addition, even very low surface tension liquids, including hexane (non-polar, 18.4 mN/m, θ_a^*= 91°), and ethanol (polar, 22.3 mN/m, θ_a^*= 112°) did not wet this surface (Table 6.1).

For fluoro-paper B, the substrate was copy paper, and the treatment method was similar to that of fluoro-paper A (Figure 6.2, fluoro-paper B), but at a higher temperature, and longer time (70 °C, 24 hours). Compared to fluoro-paper A, fluoro-paper B has flattened fibers resulting in reduced overall roughness, which yielded receding contact angles close to zero. However, advancing contact angles with both water and hexadecane remained high (Table 1). While the hysteresis on this surface was significantly higher than on the fluoro-paper A surface, the A^* values remain $\gg$ 1, indicating that the paper still strongly resisted wetting by all liquids (A^*_{water} = 19.3, $A^*_{hexadecane}$ = 3.1).

For fluoro-paper C, the substrates were filter papers, pre-treated by O$_2$ plasma etching with a Plasmatherm 790 (chamber pressure 20 mTorr, O$_2$ flow rate 20 sccm, bias RF source power 200 W, etching time 10 min) to produce nanoscale fibrillar texture. The silanization process was similar to that for fluoro-paper A, but at a higher temperature, and for a longer duration (120 °C, 24

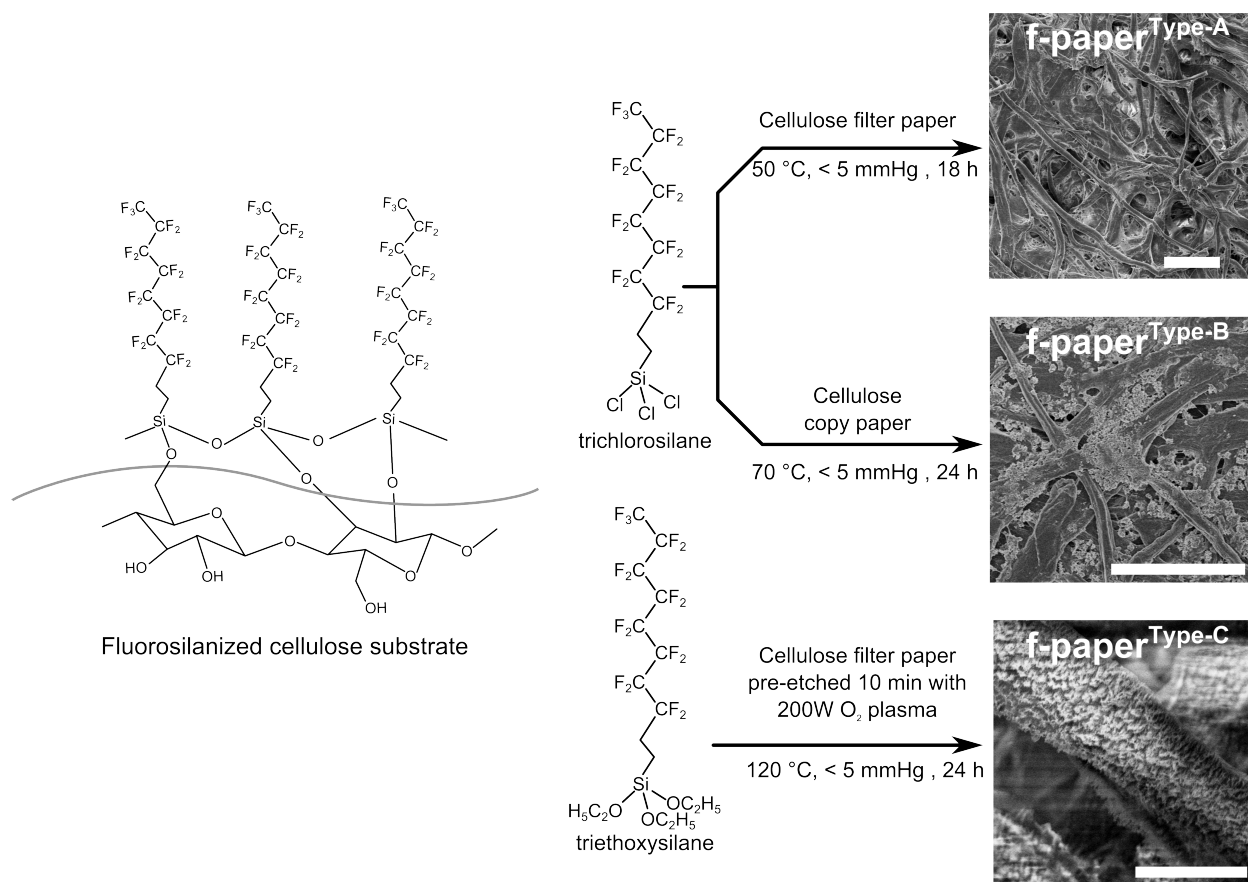**Figure 6.2:** Schematic illustration of the silanization procedures employed to prepare omniphobic fluoro-papers. Scale bars on the SEMs are 10 μm.

hours) (Figure 6.2, fluoro-paper C). The triethoxy functional silane was used instead of the trichloro functional silane to avoid embrittlement of the paper (already weakened by the extended plasma etching) by the hydrochloric acid byproduct produced during extended high temperature reactions with chloro-silanes. The micro- and nano-scale hierarchical texture due to the pre-functionalization etching made fluoro-paper C omniphobic, with significantly lower contact angle hysteresis than fluoro-paper A (Table 6.1).

6.2.2 Wettability Characterization

All contact angle measurements were obtained using a Ramé-Hart 200-F1 goniometer. 3 μL droplets were used for static contact angle measurement. The advancing and receding contact angles measurements were performed starting with a 3 μL droplet on the surface and then growing and shrinking it by adding and removing a small volume (~2μL) using a 2 mL micrometer syringe (Gilmont) while continually measuring contact angles. Contact angle hysteresis was calculated as the difference between advancing and receding contact angles. At least three measurements were performed on each sample surface. Typical error in measurements was ± 2°.

Table 6.1: Fabrication parameters and the resulting contact angles with water and hexadecane (HD) for each of the three different fluorinated paper substrates developed in this work.

Type	Substrate	Silanization conditions	Contact angles (°)				A^*		
			Water		Hexadecane		H_2O	HD	Media
			θ_a^*	θ_r^*	θ_a^*	θ_r^*			
A	filter paper	50 °C, < 5 mmHg, 18 h trichlorosilane	161	143	136	5	24.6	4.5	–
B	copy paper	70 °C, < 5 mmHg, 24 h trichlorosilane	153	0	113	0	19.3	3.1	–
C	filter paper	120 °C, < 5 mmHg, 24 h triethoxysilane	167	157	162	128	$> 45.0^a$	13.6	25.4

a. No breakthrough could be observed for the minimum measurable droplet size (1 μL)

To measure A^*, a series of droplets of varying volume were deposited on surfaces. A higher Laplace pressure can be expected from a smaller droplet due to the increase in curvature.[17] A decrease in the apparent contact angle of droplet will result from an increase in Laplace pressure as it causes the composite interface to sag deeper into the texture. The apparent contact angle was measured with the goniometer. If the apparent contact angle was below 90° with a specific droplet volume, the droplet was considered to be definitively in the wetted Wenzel state, and the corresponding Laplace pressure considered to be greater than the breakthrough pressure for the surface. A^* was then calculated as the Laplace pressure divided by the reference pressure for the liquid.

6.3 Fabrication of Wettable Channels

It is possible to treat the obtained superomniphobic or omniphobic paper samples with high power oxygen plasma to obtain the complete range of selective extreme wettabilities towards water and oil (Figure 6.1). Microfluidic with defined dimensions and wettabilities could be fabricated by selectively covering fluoro-paper A substrates with polyimide tape prior to O_2 plasma etching (Figure 6.1b). This process is described in detail in our manuscript.[248]

However, during optimization of a device geometry, it is useful to be able to pattern the channels with a mask-less technique to rapidly fabricate prototypes for testing. The method using Kapton tape in Figure 6.1 requires significant labor, or requires the purchase of pre-fabricated masks with a fixed design. Additionally, leakage of the oxygen plasma underneath the mask through the paper substrate decreases the effective patterning resolution. To improve usability and reduce the time required for the patterning process, we also developed a mask-free, direct printing technique to produce fluidic

channels of arbitrary geometry, capable of containing very low surface tension liquids (Figure 6.3a).

This maskless process involves the direct deposition of high surface energy material onto fluoro-paper B. Compared to fluoro-paper A, the near-zero θ_r for both water and oil on fluoro-paper B guaranteed no dewetting during application of the ink, allowing the precise deposition of continuous wettable channels. The retention of reasonably high θ_a on the background prevented the ink from wicking or spreading on the surface. The ink was deposited by directly applying a viscous solution through a tapered deposition nozzle attached to an XYZ motorized stage. The ink was a water-based polyurethane (Aleene's Fabric Fusion permanent fabric adhesive), dissolved in ethanol to make a 500 mg/mL solution, and then diluted 1 : 3 by volume with a 20 mg/mL sodium dodecyl sulfate aqueous solution to tune the surface tension and viscosity. The final solution was probe sonicated (Heat Systems Ultrasonic Processor Sonicator) for 2 min and filtered through a 0.2 μm syringe filter.
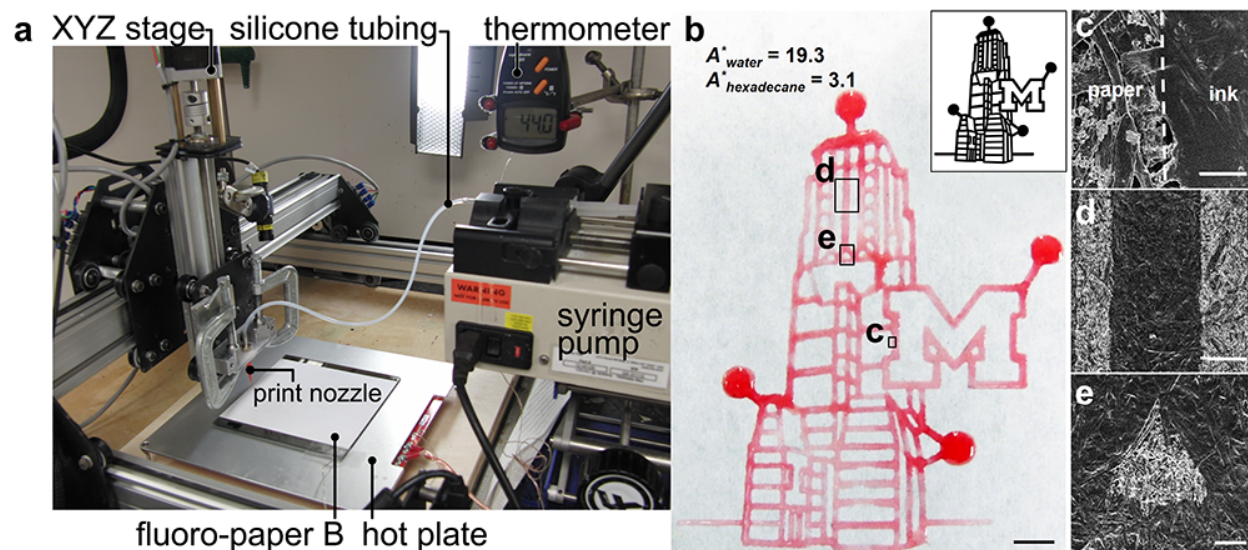

Figure 6.3: Mask-free, direct printing of fluidic channels on omniphobic paper. (*a*) The printing apparatus consisting of a syringe-pump feeding a nozzle attached to an XYZ motion stage. (*b*) A printed pattern on a fluoro-paper B surface. The channels have been filled with silicone oil (γ_{LV} = 19.8 mN/m), dyed red. The inset is the 5.3 × 4.4 cm pattern being printed. Scale bar is 5 mm. (*c-e*) SEM images highlighting the magnified texture for different areas on the patterned surface shown in (*b*) after the channel is filled with silicone oil. The corresponding areas are labeled as c, d, and e in (*a*). Scale bars are 50 μm for *c*, 500 μm for *d*, and 200 μm for *e*.

This ink formed uniform, transparent films on fluoro-paper B, with minimal dewetting (due to the low surface tension, low viscosity, and moderate evaporation rate of the ink), excellent adherence to the paper, and formed channels which were rapidly wet by most liquids other than water.

Figure 6.3 shows the lab-made printing apparatus. The printing head is a tapered polypropylene dispensing nozzle (24 gauge or 570 μm outer diameter, McMaster-Carr) connected via silicone tubing (1/16" inner diameter, McMaster-Carr) to a syringe pump (KD Scientific Model 200) operating at 1 mL/h. A motorized XYZ motion stage (Shapeoko 2) allowed selective deposition. The motion of

each axis was computer-controlled, as was the syringe pump. The fluoro-paper B substrates were temporarily attached to glass plates with a spray adhesive, which were then mounted to a carefully leveled hot plate held at 45 °C.

The minimum width of the printed lines, and the interstitial spacing between lines, were 700 μm and 400 μm respectively. A line drawing of the Lurie Bell Tower at the University of Michigan (5.3 × 4.4 cm) was successfully printed on fluoro-paper B and filled with a low viscosity silicone oil (γ_{LV} = 19.8 mN/m) (Figure 6.3 b-e). Patterns for the XYZ platform were generated by drawing them in vector graphics software (Inkscape) and then converting them to G-code commands. The pattern chosen was a line drawing of the Lurie Bell Tower at the University of Michigan, with an overall size of 5.3 cm × 4.4 cm. When ~25 μL of low viscosity silicone oil (dyed with Oil Red O) was placed in each of the four reservoirs, the whole pattern was completely filled, with wetting driven only by capillary forces, demonstrating the capability to fabricate relatively complex wettable channel geometries.

6.4   Increasing Channel Wettability

Note that the liquid filling the channels in the demonstration in Figure 6.3 was specifically chosen to maximize the wetting length, as follows from the Washburn Equation. The silicone oil exhibits $\theta_a \approx 0°$ on the polyurethane channels, low viscosity, and is also practically non-volatile, enabling complete filling of the complex pattern before the liquid evaporated.

However, aqueous solutions are predominant in most biomedical applications, and the relatively high water $\theta_a \approx 45°$ on the polyurethane severely limited the maximum wetting length and wetting velocity, especially in channels with widths < 1 mm. Extensive experimentation was performed with various hydrophilic polymers, including cellulose acetate, polyvinyl acetate, poly(vinyl alcohol), poly(vinyl pyrrolidone), cross-linked polyethylene glycol diacrylate, and direct-printing of polydopamine. A polymeric ink with a combination of good adhesion to the fluorinated paper, very low water contact angles, and no swelling or dissolution during extended exposure to water proved elusive. Adding silica nanoparticles did improve wetting somewhat as the this decreased the contact angle according to Wenzel's equation as discussed in Section 1.2.3.1.

The addition of photocatalytic titanium dioxide (TiO$_2$) nanoparticles proved to be critical to achieving superomniphilic channels with fast wetting, including water. Anatase TiO$_2$ is a well known photo-catalyst that becomes extremely hydrophilic on exposure to ultraviolet light. Exposing the printed channels to 254 nm ultraviolet light causes the accelerated degradation of organic compounds in contact with it, yielding extremely low contact angles. The same water-based polyurethane was used as a binder, with 30wt.% 32 nm anatase nanopowder, but the solvent was switched to pure acetone to better disperse the TiO$_2$. This change required some minor modifications to the printing apparatus for solvent compatibility (Figure 6.4).

6.5 Application: On-chip Lysis and Detection of *Escherichia coli* Bacteria

6.5.1 Introduction

The coliform, *Escherichia coli*, is a major pathogen worldwide due to its ability to cause fatal diarrheal and extraintestinal diseases.[279] Currently, the 'gold standard' for the determination of *E. coli* contamination are methods that use automated polymerase chain reaction (PCR) and fluorescence detection.[280] While those systems can provide accurate results within 24 hours, they rely on expensive, complex instrumentation and user expertise. Thus, there has been recent interest in developing paper-based detection devices to not only significantly reduce cost, but to also decrease result retrieval time. By printing the TiO_2–loaded superomniphilic ink as described in the previous section, we fabricated an integrated device capable of detecting dilute concentrations of bacteria. This all-in-one coliform lysis and colorimetric detection device could be employed as an affordable, portable detector for water or food contamination.

To detect *E. coli*, we utilized chlorophenol red-β-D-galactopyranoside (CPRG) as a substrate for the enzyme, β-galactosidase (β-gal). β-gal is an enzyme present inside all coliforms, including *E. coli*. When β-gal cleaves the glycosidic bond within the CPRG substrate, the CPRG is converted to chlorophenol red, with an accompanying color change from vibrant yellow to a deep red.[281] Several works have employed this method, utilizing a paper-based μPAD and a hydrophobic sol-gel patterned paper-based device to detect *E. coli* at a concentration of 10^1 colony forming units (CFU)/mL in 12 hours and a concentration of 10^7 CFU/mL within 30 minutes, respectively.[274,282] Still, these devices require at least two steps for sample analysis: lysing the bacterial cells to release the β-gal enzyme off-chip and adding the lysed cells to the paper-based device for detection. This is due to the fact that most paper-based microfluidics systems can contain only high surface tension liquids for extended periods.[272] However, recently developed paper devices have shown the capability to contain low surface tension liquids, including lysing solutions with high concentrations of surfactants.[248,273–275,283–286] This work leverages these advances and presents, to the best of our knowledge, the first time that *E. coli* has been lysed and detected through β-gal on a simple, paper-based microfluidic device.

6.5.2 Materials and Methods

6.5.2.1 Device Fabrication

Pieces of the fluorinated paper were adhered to glass slides with solvent resistant double-sided tape (3M 9629PC) and placed onto a leveled heated stage (~70 °C) in a lab-built printing apparatus (Figure 6.4b). This consisted of an XYZ motion stage (Shapeoko 2) holding a tapered
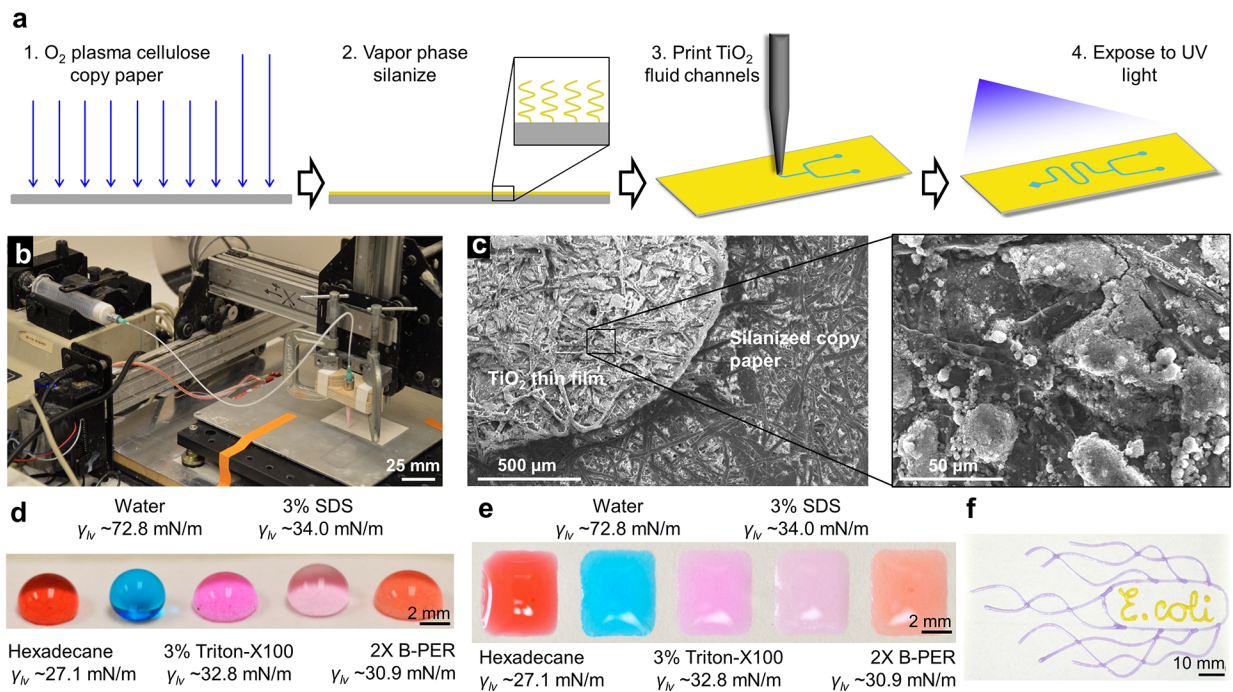
Figure 6.4: The fabrication and characterization of the paper-based *E. coli* detection devices. (*a*) The steps required to manufacture a complete *E. coli* detection device, including O_2 plasma cleaning, vapor phase silanization with a fluorinated silane, printing of the TiO_2 channels and exposure of the devices to 254 nm UV light, (*b*) the omniphilic channel printing apparatus modified from the one in Figure 6.3a, (*c*) SEM images of the TiO_2 thin film on top of the silanized copy paper. The inset highlights the nanoscale roughness of the printed TiO_2 thin film. (*d,e*) Liquid drops on the omniphobic and superomniphilic regions, respectively, and (*f*) a channel in the shape of a single *E. coli* bacterium filled with dyed silicone oil, demonstrating the ability to confine low surface tension liquids and to print any desired microfluidic channel with this technique.

polypropylene dispensing nozzle (20 gauge or 610 μm outer diameter, McMaster-Carr) connected via polytetrafluoroethylene tubing (1/32" inner diameter, McMaster-Carr) to a syringe pump (KD Scientific Model 200) which dispensed the solution at 2.25 mL/h from a glass syringe. The motion and operation of the pump and XYZ stage were computer-controlled with GCODE commands, which were generated from design files produced in Inkscape, an open-source vector drawing software. This apparatus allows the mask-free patterning of arbitrary polymer solutions on a variety of substrates with ~500 μm resolution. Two passes were performed to ensure uniform coverage of the TiO$_2$ ink on the fluorinated paper. Once deposited, the ink was exposed to 254 nm UV light in a sterilizer cabinet (purchased from Salon Sundry) for 5 hours to render it wettable by all liquids prior to use.

6.5.2.2 Device Testing

Dynamic contact angles were measured on the fluorinated paper with a Ramé-Hart 200-F1 goniometer, using the sessile drop technique. Dyed deionized water, hexadecane (Alfa Aesar), 3 wt.% aqueous solutions of Triton X-100 (MP Biomedicals) and sodium dodecyl sulfate (Hoefer) surfactants, and 2X B-PER Bacterial Protein Extraction Reagent (purchased from Fisher Scientific) were used to test the capacity of the printed devices to contain a broad range of liquids (Figure 6.4d,e). The pendant drop method was used to measure the surface tensions of these liquids with the goniometer.

6.5.2.3 Mixing Channel Design

An approximate model of the cell lysis device was generated in COMSOL 5.2 to guide the design of the channel to ensure thorough mixing of the cell lysis reagents and the *E. coli*, in order to enhance the reproducibility and speed of the assay. The central segment of the device was modeled as a laminar flow channel, with a no-slip boundary condition at the solid-liquid contact at the channel base, and a slip boundary condition for the liquid-air interfaces at the top and sides. A chemical species was introduced at one inlet of the flow channel, and its concentration was plotted to evaluate the effectiveness of mixing of various geometries. The results were compared to photographs taken of aqueous food-dye solutions (McCormick) mixing in the channels.

Due to the laminar flow within microfluidic channels, with a low Reynolds number of approximately 2.25 (assuming the density of the fluid is ρ = 1,000 kg/m^3, the velocity of the fluid is u = 1 mm/s, the characteristic linear dimension is L = 2 mm, and the kinematic viscosity of water is η = 8.9 × 10^{-11} Pa·s), it is difficult to achieve complete, homogeneous mixing of two liquids. Therefore, we designed our device with two inlets leading into a serpentine mixing zone that ends at a detection patch. We simulated how adding 2, 3, 4 or 7 turns to the serpentine mixing zone affects the mixing of the two fluid streams with a simplified COMSOL model of the central section of the device. Figure 6.5a shows the concentration profiles obtained for the 0 and 7 turn open-channel devices. It is clear that increasing the amount of turns in the serpentine mixing section effectively

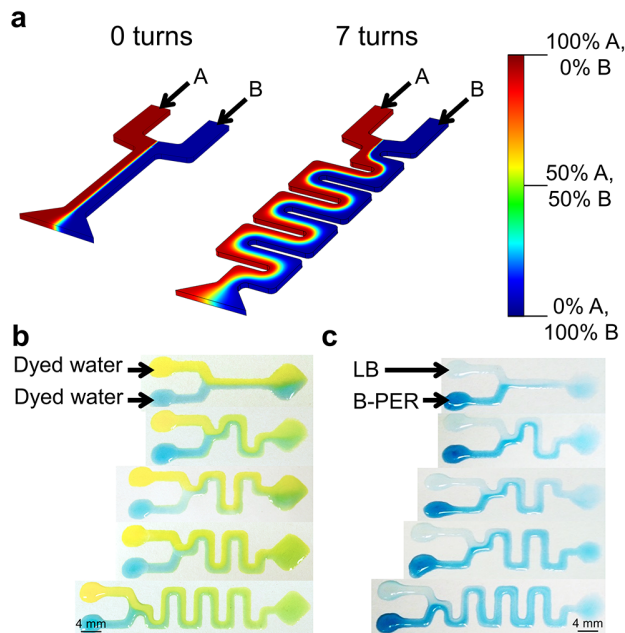increases the mixing between the two fluid streams.

Figure 6.5: Optimization of device design to achieve complete mixing. (*a*) Concentration profiles generated from COMSOL models of lysis devices with zero or seven turns in the mixing channel. Dark red represents a 100% concentration of liquid A and dark blue represents a 100% concentration of liquid B. (*b-c*) Images demonstrating the effective mixing in the serpentine region of the device with (*b*) dyed water and (*c*) LB and 2X B-PER. The addition of more turns in the serpentine region increased mixing, allowing for nearly homogeneous mixing in the 7-turn device.

After fabricating all five devices, we experimentally tested the mixing effectiveness of the serpentine regions by adding water dyed yellow into one inlet and water dyed blue in the other. The results shown in Figure 6.5b exhibit that adding more turns in the serpentine region increased mixing: there was a clearly defined interface in the detection region of the 0 turn device and as more turns were added, that interface became less clear until it was almost entirely mixed in the detection region of the 7 turn device. This matched the trend observed in the COMSOL model.

We also tested the mixing capability of all five devices for the *E. coli* assay by adding LB Broth (Lennox), the bacteria medium, in one inlet and blue-dyed 2X Bacterial Protein Extraction Reagent (B-PER), the lysis buffer, in the other, shown in Figure 6.5c. These results followed the same trend as those in Figure 6.5b, however, the two streams appeared to effectively mix within fewer turns when compared to the number of turns it took the dyed water to mix. This can be attributed to the Marangoni effect, which describes the mass transfer across an interface with a surface tension gradient,[287] as LB has an approximate surface tension of 72 mN/m while 2X B-PER has an approximate surface tension of 31 mN/m. The Marangoni flow opposing the pressure-driven and capillary flows was clearly observable during the filling of the channels.

6.5.2.4 *E. coli* Culture and Growth

Colonies of *Escherichia coli* (UTI89), were grown overnight at 37 °C onto LB broth (Lennox) agar (from Fisher Scientific) plates and all colonies were used within two weeks of growth. To perform experiments, one colony scraped from the LB agar plate was grown in LB Broth (Lennox, MP Biomedicals) on a shaker at 37 °C with 10 mM isopropyl β-D-1-thiogalactopyranoside (IPTG, purchased from Invitrogen). When the optical density at 600 nm reached 0.6 ± 0.1 (measured with a Biochrom Ultrospec 2100 pro UV/Visible Spectrophotometer), indicating an approximate concentration of 10^7 colony forming units (CFU)/mL, the *E. coli* were tested on the serpentine devices. Here, the term colony forming unit is not necessarily equivalent number of cells, as even a viable bacterium may fail to form a colony when cultured. The total concentrations of cells in all experiments performed were quantified by simultaneously plating on an LB agar plate while testing the devices. For the sensitivity tests, one colony forming unit was grown in LB until the optical density reached 0.6 ± 0.1. The *E. coli* in LB was serially diluted down to approximately 10^2 CFU/mL and 1 mL was placed into 99 mL of sterile LB, yielding an effective cell concentration of 1 CFU/mL. The *E. coli* were incubated with 10 mM IPTG and samples were taken out at various time points. At each time point, the withdrawn sample was used to measure optical density and to induce a color change on the diamond-shaped devices.

6.5.2.5 Lysis-on-a-chip Assay

1 μL of chlorophenol red-β-D-galactopyranoside (CPRG) (purchased from Sigma-Aldrich) dissolved in 2X Bacterial Protein Extraction Reagent (B-PER, purchased from Fisher Scientific) at a concentration of 3 mg/mL was placed in the detection region of the device and allowed to evaporate. *E. coli* in LB and 2X B-PER were pipetted into their respective inlets and were allowed to wet the omniphilic regions of the device. Characterization images were taken on a Nikon D3200 camera with fixed exposure and lighting settings.

6.5.2.6 Image Thresholding

All thresholding to identify the CPRG color change from digital photographs was performed in MATLAB R2014a. Since the CPRG reagent is initially yellow and gradually transforms to a deep red, all three color channels (Red, Green, and Blue) need to be considered simultaneously. Figure 6.6 shows a schematic of all RGB colors and the colors within the white box represent all possible colors that can be observed as the assay transforms from a bright yellow to a deep red, within the thresholding limits of R > 140, G < 200, and B < 200.

6.5.3 Results

To optimize the design of the lysis-on-a-chip assay, two detection patch shapes, circles and diamonds, were considered because once the assay is performed, sensitive detection relies on the edge
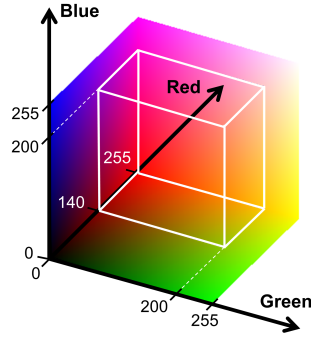
Figure 6.6: RGB schematic with a white outlined box showing the colors contained within the thresholding limits of R > 140, G < 200, and B < 200.
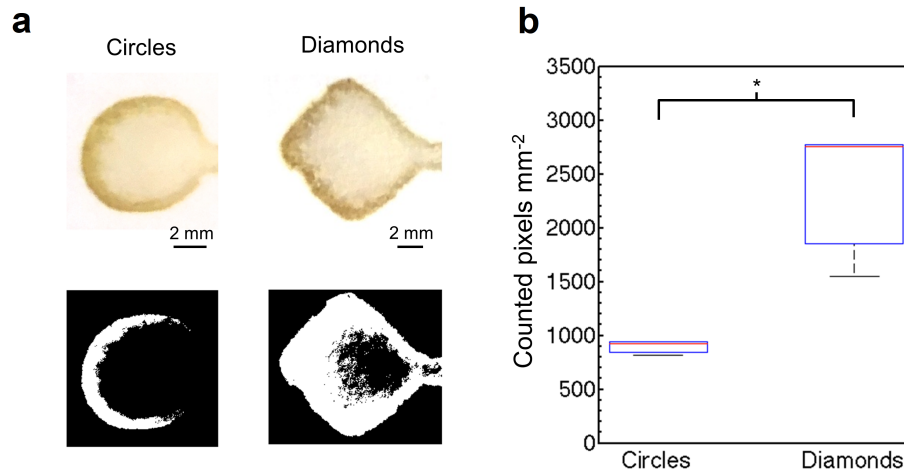

Figure 6.7: (*a*) Bright-field images and corresponding processed images via thresholding for both circular and diamond-shaped detection patches. (*b*) Counted pixels per unit area of the processed images for both circular and diamond-shaped detection patches. With a higher number of counted pixels, diamond-shaped detection patches exhibit a statistically significant ($p = 0.0228$) increase in sensitivity compared to circular detection patches.

concentrating coffee ring effect.[288] Using the thresholding limits discussed above, we investigated which shape would be more optimal: circles or diamonds. Figure 6.7a shows the bright-field images of the circular and diamond-shaped patches along with their respective processed images via thresholding, where a white pixel indicates a pixel with RGB values within these limits. While it is visually clear that the diamond-shaped patch has more white pixels or 'hits', we also quantified this difference in Figure 6.7b, a plot of the white counted pixels per unit area for both the circles and the diamonds. The statistically significant ($p = 0.0228$) difference in counts can be attributed to the increased perimeter to surface area ratio of the diamonds: for circles, the perimeter to surface area ratio is $2\pi r/\pi r^2 = 2/r$ and for diamonds, the ratio is $4r/r^2 = 4/r$. Thus, diamond-shaped detection patches better enhance the coffee ring effect.

To perform the lysis-on-a-chip assay, *E. coli* in LB with isopropyl-*D*-1-thiogalactopyranoside
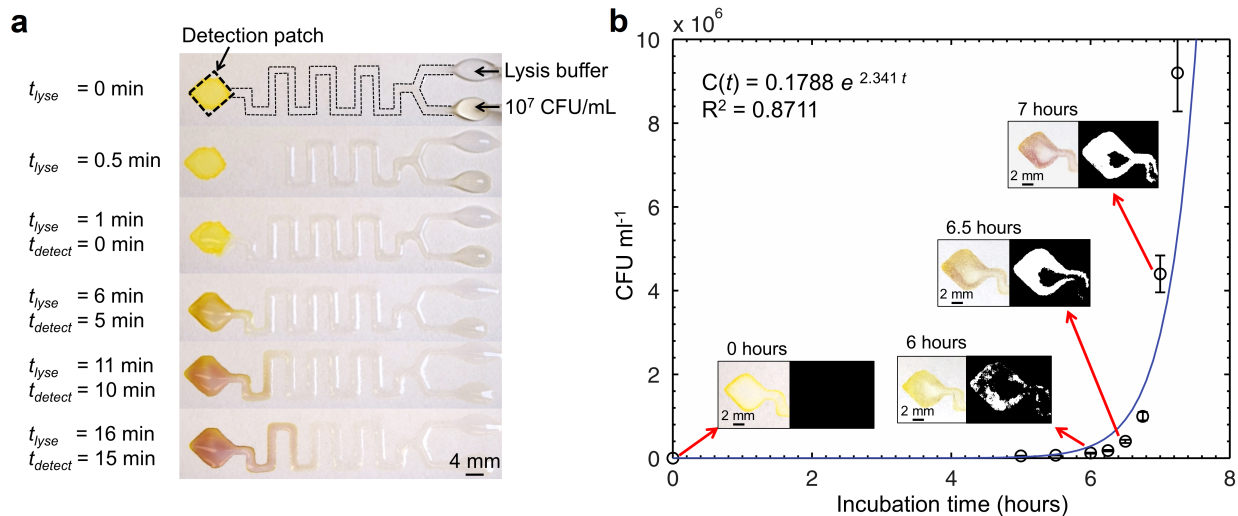
114

Figure 6.8: (*a*) *E. coli* lysed on chip at a concentration of ~10^7 CFU/mL with the *E. coli* inlet, 2X B-PER lysis buffer inlet and the CPRG detection patch labeled. The *E. coli* spent approximately one minute mixing with the lysis buffer in the serpentine region before reaching the detection patch, and there was a noticeable color change within 5 minutes at the detection patch. After 15 minutes, the color change nearly reached completion. (*b*) The growth curve and corresponding color change images with their respective processed images on the lysis devices for ~1 CFU/mL incubated in medium over time. After 6 hours of incubation, there was a noticeable onset of color change.

(IPTG, a lactose-like molecule used to induce β-gal production)[289] and 2X B-PER were added to their respective inlets in the 7 turn mixing devices, as shown in Figure 6.8a. The 7 turn serpentine channel devices allowed for a residence time of about one minute, providing both diffusion across the interface and chaotic advection as mechanisms for mixing.[290] Figure 6.8a shows the time-lapse images of the *E. coli* (at a concentration of ~10^7 CFU/mL) mixing with the lysis buffer in the serpentine region of the device and the resultant color change after the solution reaches the detection patch. A color change initially becomes observable within 5 minutes after the liquid reaches the detection patch, but the change nearly reaches completion after about 15 minutes in the patch. Thus, the devices were not only able to contain the lysis buffer, but they successfully lysed the *E. coli*, releasing the β-gal within the cells and causing the CPRG to become chlorophenol red.

For real-world applications, coliform detection devices need to be sensitive to much lower bacterial concentrations.[291] To address this issue, we incubated 1 CFU/mL of *E. coli* in LB at 37 °C and tested the inoculum at various time points. Figure 6.8b shows the growth curve with the corresponding color changes and processed images within the diamond-shaped patches indicated at their respective time points. After 6 hours, the color change started to become apparent to the naked eye and after 7 hours, the color change nearly reached completion. Therefore, with minimal incubation time (~6 hours), the diamond-shaped devices were able to detect a concentration of 1 CFU/mL, a concentration that is more applicable outside of the laboratory.

6.5.4 Conclusion

In this work, we demonstrated the capability to create an all-in-one lab-on-a-chip device that can lyse and detect pathogenic *E. coli* within minutes. The device was composed of omniphilic channels fabricated on omniphobic paper with a direct printing technique, allowing rapid maskless fabrication of arbitrary channel geometries. The materials were engineered to contain the low surface tension lysing solution, and the channel was designed with a serpentine shape to ensure effective, homogeneous mixing of the *E. coli* and the lysing solution prior to detection. After lysing, the enzyme, β-galactosidase, was used to determine the presence of *E. coli* (at a concentration of 10^7 CFU/mL) in the contaminated sample with a yellow to red colorimetric assay. A dilute sample at only 1 CFU/mL was detectable by incubation prior to introduction to the device, allowing detection within 6 hours. While this device was only shown to detect *E. coli*, the printing fabrication method discussed in this chapter allows for versatility in developing essentially any 2D open-channel paper-based microfluidic device, opening the door to a plethora of potential bio-applications.

CHAPTER 7

Open-channel, Water-in-Oil Emulsification
in Hybrid Paper-Based Microfluidic Devices

This chapter is adapted from an article published in *Lab on a Chip*, equally co-authored with Dr. Chao Li.[292] It details the fabrication of a laser-cut paper-based microfluidic device capable of containing low surface tension liquids at higher flow rates than the method described in Chapter 6, enabling the first demonstration of water-in-oil emulsification in an open-channel device.

7.1 Introduction

The majority of microfluidic devices discussed in the literature are composed of covered or closed capillaries. As discussed in Chapter 6, in recent years, there have been multiple reports on open-channel devices in which one to three sides surrounding the liquid channel have been removed.[293–295] Such open-channel devices have several distinguishing advantages, including their inherently large liquid-vapor interface,[294] easy accessibility to the flowing fluid,[296–298] relatively rapid and low-cost fabrication methodology,[299] ease of use, and low fluid shear force,[300] making them particularly useful for many biological and biomedical applications.[301,302] One significant application of microfluidic devices is the generation of monodisperse emulsions and particles of precisely tunable composition and size.[303,304] Such devices rely on the co-axial flow of two or more immiscible phases through a geometric constriction, with the resulting shear forces breaking-up the inner phase(s) into droplets suspended in the outer fluid.[305]

However, reports of droplet generation in open channel devices have been very limited. This is because relatively high flow rates are required to maintain a stable emulsification interface within the channel.[303,306,307] That is, the outer phase flow rate must be sufficient to confine the inner phase to the flow-focusing region. The inner phase must not be allowed to overflow into the inlet channels or past the constriction without being emulsified. Liquids at these flow rates are easier to contain in closed capillaries with physical walls.[248] Water-in-oil emulsions, required for creating monodisperse droplets composed of an aqueous phase, are particularly difficult to generate with open-channel devices. This is because the low-γ_{LV} liquid in the outer (oil) phase must be confined while flowing

117

at sufficiently high flow rates to induce emulsification of the inner (aqueous) phase without any physical confinement. Monodisperse droplets composed of an aqueous phase are desirable for many life science and biomedical applications. These include the fabrication of hydrophilic microparticles for drug delivery, and the encapsulation of cells within hydrophilic polymers or hydrogels.[305,308,309]

To confine liquids in open channels, typically a wettability barrier is employed in lieu of solid channel walls (physical confinement). The wettability barrier is achieved by employing either a contrast in solid surface energy and / or texture between the channels used for fluid confinement and the background.[250,273,286,295,310–313] Compared to water (γ_{LV} = 72.1 mN/m), liquids with low surface tension (γ_{LV} < 30 mN/m) are much more difficult to confine in open channels, as they readily spread on most surfaces. Materials with very low surface energy and precisely engineered textures are necessary to maintain a sufficiently high advancing contact angle with low surface tension liquids.[5,40,43] This explains why most open-channel microfluidic devices reported in the literature are usually only compatible with water or other high-surface-tension aqueous solutions.[272–275]

Oil-water interfaces are commonplace in many chemical reactions and biological systems.[314] This makes methodologies for the fabrication of open-channel microfluidic devices compatible with all liquids relevant to a wide range of academic and commercial interests. For example, Whitesides *et al.* previously developed a methodology for fabricating paper-based microfluidic devices using fluoro-silanized paper.[273] When the devices were infused with perfluorinated oil, liquids with surface tension as low as 15 mN/m could be physically confined within the folded paper. In our first approach to fabricating paper-based microfluidics, as discussed in Chapter 6, selective wettability between polar and nonpolar liquids was also achieved by selective treatment of fluorinated paper with oxygen plasma. This combination of wettabilities enabled several novel open-channel microfluidic devices, among which was the first demonstration of open-channel oil-in-water microfluidic emulsification, which was used to fabricate hydrophobic polymer microparticles. However, due to the limited flow rate of oil in that system, which employed wettability-patterning alone, achieving water-in-oil emulsification remained challenging.[248]

The question of how to maximize the liquid flow rate in open channels has been previously studied.[315–317] The flow rate for a given liquid in an open channel, with a constant cross-sectional area, is increased by augmenting the ratio of the wetted interface to the free air-liquid interface.[315] Based on this principle, a higher flow rate can be expected from an open channel with a wettable floor and two wettable sidewalls, compared to an open channel with only a wettable floor. Thus, for our devices, the channel floor and the two side-walls needed to be selectively wet by the outer oil phase, and allow for a high-enough flow rate for water-in-oil emulsification. Simultaneously, the upper surface of the emulsification device needed to completely repel both water and oil, in order to confine these liquids within the wettable channel. This implied that the upper surface has to be "superomniphobic",[77] achieving very high contact angles with both water and oil (See Section 1.2.4).

7.2 Device Overview

As discussed previously in Chapter 6, a robust superomniphobic surface may be fabricated from paper which is plasma etched to introduce hierarchical nanotexture and then treated with a hydrophobic fluoro-silane. This "fluoro-paper C" could then be laser-cut into the desired channel geometry, selectively plasma-treated to create hydrophobic-oleophilic sidewalls, and adhered to a hydrophobic-oleophilic substrate – namely, the bidentate PDMS silane discussed in Chapter 5. Without this treatment, if the substrate were in its inherent omniphilic state, the water droplets would have sank to the bottom of the channel (due to their higher density) and displaced the oil. This would have prevented the motion of the dispersed aqueous-phase droplets and stopped the device from functioning. Open channels fabricated with this combination of superomniphobic paper channels and hydrophobic/oleophilic sidewalls and floor can even confine hexane (γ_{LV} = 18.4 mN/m at 20°C), or hexadecane (γ_{LV} = 27.5 mN/m at 20°C) at sufficiently high flow rates for emulsification (up to 2 mL/min in 2 mm wide channels). The fully-assembled emulsification device is shown in Figure 7.1a. From top to bottom, it consisted of a PMMA tubing holder, a PMMA spacer to keep the holder from touching the liquid in the channel, and the fluoro-paper channel on the smooth hydrophobic/oleophilic substrate. The flow-focusing nozzle[306] used in our device was a trapezoidal constriction in the channel (Figure 7.1d). The water-in-oil emulsification behavior was then studied with this open-channel device.

7.3 Experimental Details

7.3.1 Preparation of Superomniphobic Fluoro-paper Substrates

A superomniphobic, robust liquid barrier for both water and oil was fabricated by producing nano-fibrillar texture on top of the filter paper microfibers using oxygen plasma etching prior to fluoro-silanization as in our previous work (see fluoro-paper C in Section 6.2). The ultralow surface energy of the grafted fluorosilane, combined with the hierarchical micro- and nano-structures (Figure 7.1d, i), yielded high advancing and receding contact angles with both water and oil on the treated paper surface. This produced superomniphobic "fluoro-paper" enabled droplets of both water and various oils to readily bounce off its surface (Figure 7.2, Table 7.1).

7.3.2 Preparation of Open-channel Flow-focusing Devices

A schematic of the entire fabrication process is presented in Figure 7.3. The superomniphobic fluoro-paper was attached to solvent-resistant double-sided tape (3M 444) on the back side, and laser cut with the desired dimensions (Full Spectrum Laser H-Series) using patterns designed in Inkscape, an open-source vector design software. The laser-cut side-walls also showed a significantly smoother surface texture than the as-etched upper surface. This was because the hierarchical nanotexture was eliminated and many of the microfibers were fused together (Figure 7.1d, ii). To make the channel
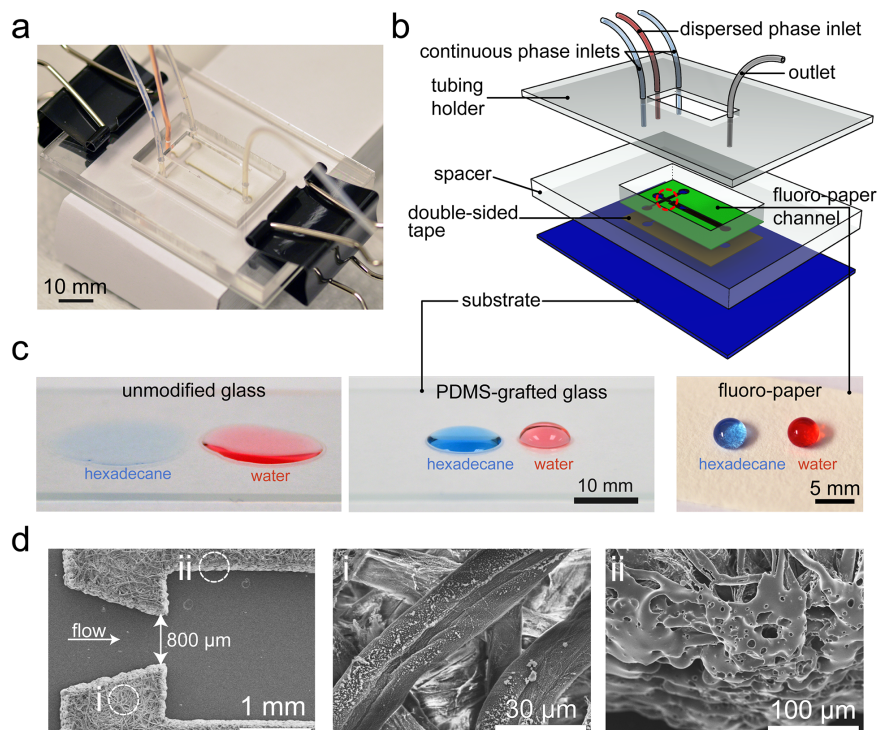
Figure 7.1: (*a*) A photograph of the open-channel emulsification device. (*b*) A schematic of the emulsification device, (*c*) droplets of the hexadecane (blue) and water (red) on an unmodified glass substrate (far left), and on a substrate with a grafted PDMS thin film (middle). This modification is necessary to allow the continuous phase to preferentially wet the channel and allow the emulsified droplets to flow in the channel. Both liquids are completely repelled by the fluoro-paper (far right). (*d*) SEM of the flow-focusing section of the channel (nozzle width 800 μm) highlighted in (*b*), with detailed views of (*i*) the upper surface with plasma-etched nanofibrillar texture and (*ii*) the laser-cut edge of the channel.
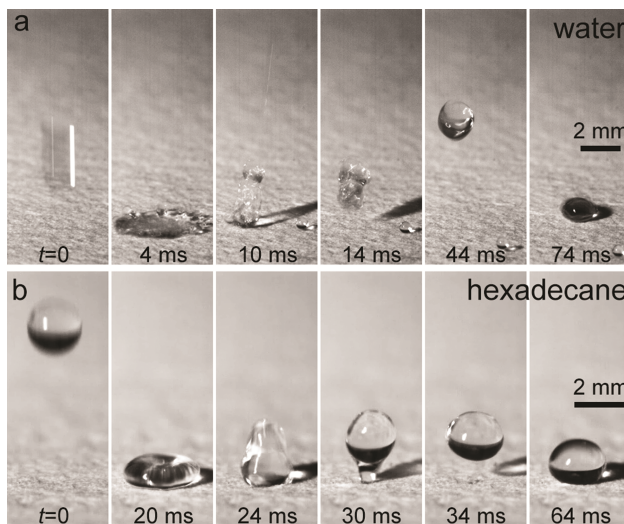

Figure 7.2: Frames from a high-speed video of (*a*) water and (*b*) hexadecane droplets bouncing off the fluoro-paper from a height of 10 cm and 1 cm, respectively. The water droplet bounced several more times before coming to rest.

Table 7.1: Contact angles and hysteresis for water and hexadecane on superomniphobic fluoro-paper, unmodified glass, and PDMS-grafted glass.

Substrate	Liquid	θ_a (°)	θ_r (°)	$\Delta\theta$
Fluoro-paper	Water	167	157	10
	Hexadecane	162	151	11
Unmodified glass	Water	12	0	12
	Hexadecane	31	0	31
PDMS-grafted glass	Water	115	96	19
	Hexadecane	39	32	7
PDMS-grafted silicon wafer	Water	105	100	5
	Hexadecane	36	34	2

walls hydrophobic and oleophilic to ensure sufficient flux of the carrier fluid, they were selectively exposed to O_2 plasma between a glass slide and a laser-cut PMMA mask with the same channel geometry to protect the top surface (Harrick Plasma PDC-001, 30W, 250 mTorr, 0.4 sccm O_2, 5 min).

The channel substrate was either a glass slide or silicon wafer, cleaned with glassware detergent and deionized water, air-dried, and then exposed to a vapor of 1,3-dichlorotetramethyldisiloxane (Gelest SID3372.0) for 10 min at room temperature, then thoroughly rinsed with toluene. This process yielded a robust hydrophobic/oleophilic PDMS-grafted monolayer that enhanced the flux of oil in the channel, and allowed submerged aqueous droplets to slide (Table 7.1). The laser-cut, adhesive-tape-backed fluoro-paper channel was then adhered to the substrate, and assembled with laser-cut PMMA components as shown in Figure 7.1a,b.

7.3.3 Materials

Deionized water was generated with a Pall Corporation Cascada RO-water purification system. Hexadecane was purchased from Fisher Scientific. FD&C Red 40 food coloring (McCormick) was used to dye water for visibility. Oil Blue N (Alfa Aesar) was used to dye hexadecane. Ethylene glycol (Acros Organics) and poly(vinyl alcohol) (98% hydrolyzed, 88 kDa, Acros Organics) were used to tune the surface tension, density, and viscosity of the aqueous dispersed phase according to the literature.[294] The outer fluid was hexadecane with 10 wt.% Span 80 nonionic surfactant (TCI Chemicals) to enhance emulsification. Model drug delivery hydrogel particles were fabricated from cross-linked polyethylene glycol diacrylate (PEGDA, Mn = 700, Sigma-Aldrich), photo-initiated with 1 wt.% 2-Hydroxy-2-methyl-1-phenyl-propan-1-one (Ciba Darocur 1173), and loaded with 25 wt.% of an 800 μg/mL doxorubicin aqueous solution (drug purchased from Adooq Bioscience).
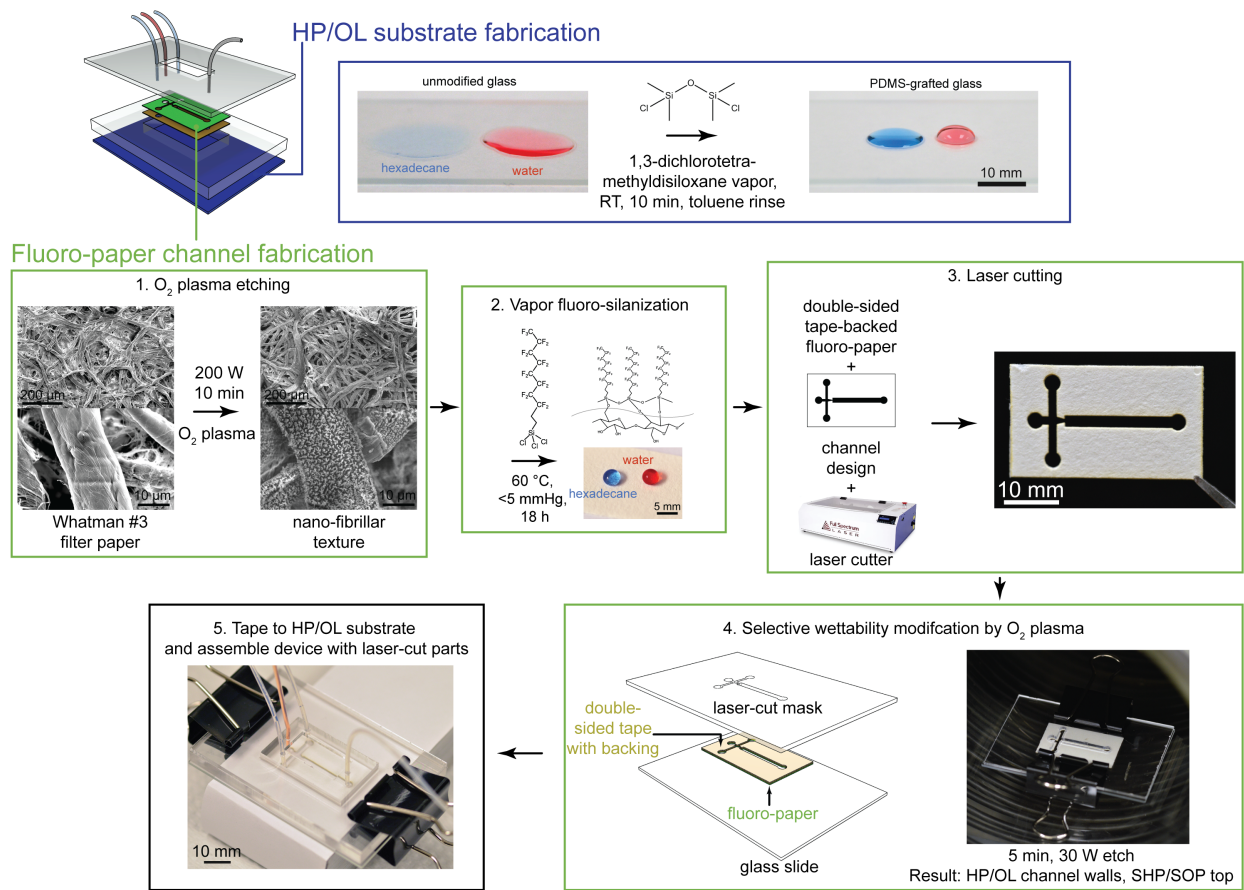
Figure 7.3: Overview of the fabrication process for the major components of the open-channel flow-focusing emulsification device – namely, the hydrophobic/oleophilic substrate, the laser-cut fluoro-paper channel with superomniphobic top surface, and the hydrophobic/oleophilic walls.
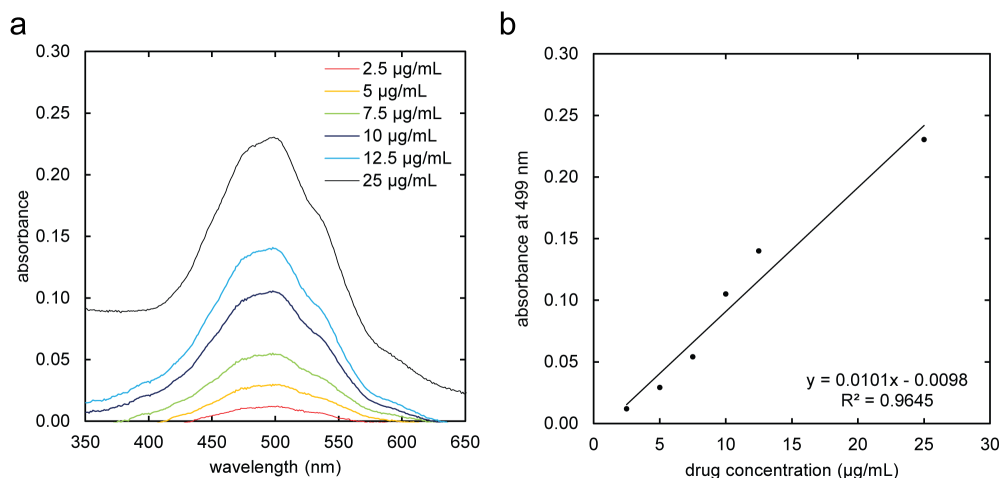
Figure 7.4: (*a*) Absorbance spectra for varying concentrations of aqueous doxorubicin solutions and (*b*) the calibration curve generated from these absorbance spectra for determining doxorubicin concentration released from the particles.

7.3.4 Open-channel Emulsification and Particle Generation

The organic continuous phase and aqueous dispersed phase flow rates were independently controlled with syringe pumps (KD Scientific KDS-230). Flow through the flow focusing geometry of the channel forced the formation of monodisperse droplets of aqueous solutions or hydrophilic polymer precursors. The polymer precursor droplets were flowed past a 365 nm UV LED spot source (Henkel EQ CL10, 3% intensity, 6 mm spot diameter, placed 5 mm above the channel) to initiate the photocuring reaction. A silicon wafer was substituted for the glass slide for the particle generation experiments as it was necessary to localize the transmission of UV light to the flow-focusing region. Stable operation was observed for over an hour with this configuration. The droplets or particles were collected from the channel by applying vacuum into a jar serving as a reservoir. Particles were rinsed with hexane and water to remove surfactant and unreacted monomer, then filtered, collected, and stored in hexane until imaging or drug delivery studies.

7.3.5 Drug Release

Drug release measurement was performed by placing 350 mg of dry particles into a vial with 2 mL deionized water. Visible absorbance spectra were periodically collected for 1 mL of the supernatant transferred to a cuvette, then returned to the vial. The absorbance at 499 nm was compared to a reference curve generated by measuring aqueous doxorubicin solutions of known concentration to determine the concentration of doxorubicin released from the particles, and therefore the percentage released compared to the total drug content (Figure 7.4).

7.3.6 Characterization Methods

Photographs and videos were recorded with a digital camera (Nikon D3200). Image analysis for particle sizing was performed with ImageJ. Fluorescent images were obtained with a Nikon Eclipse 80i. SEM images were acquired with a Hitachi SU8000 ultra-high resolution SEM with an accelerating voltage of 10 kV. UV-visible spectra were collected with an Agilent/Varian Cary 50. High speed video was captured with a Fastec Imaging HiSpec 1 at 500 fps for water and hexadecane droplets released from a microsyringe at 10 cm and 1 cm above the fluoro-paper substrate, respectively. All contact angle measurements were obtained using a Ramé-Hart 200-F1 goniometer. The advancing and receding contact angles measurements were performed starting with a 3 μL droplet on the surface and then growing and shrinking it by adding and removing a small volume (~ 2 μL) using a 2 mL micrometer syringe (Gilmont) while continually measuring contact angles. Contact angle hysteresis was calculated as the difference between advancing and receding contact angles. At least three measurements were performed on each sample surface. Typical error in measurements was ± 2°.
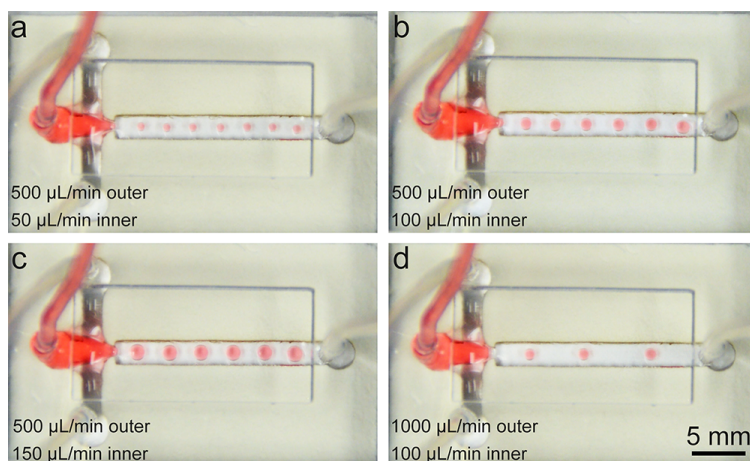

Figure 7.5: Water-in-hexadecane emulsification under varying flow conditions with the device shown in Figure 7.1. The continuous organic phase (clear) is composed of hexadecane + 10 wt.% Span 80, and the dispersed aqueous phase (red) is composed of water + 10 wt.% glycol, 2 wt.% polyvinyl alcohol.

7.4 Results

When the outer flow rate was held constant and the inner flow rate increased, the size of aqueous-phase droplets was found to increase (Figure 7.5a-c, Table 7.2). A similar trend has been previously observed with closed-channel microfluidic emulsification.[303,306,307] On the other hand, when the inner flow rate is kept constant, and the outer flow rate is increased in closed-channel devices, typically there is a transition from "dripping" to "jetting" emulsification. In jetting emulsification, the inner liquid extends into an elongated thread downstream from the flow-focusing channel and the break-up into droplets occurs at its tip.

Table 7.2: Dimensions of droplets from open-channel emulsification of water in hexadecane (Figure 7.5).

Outer flow (μL/min)	Inner flow (μL/min)	Droplet diameter (μm)	Droplet center-to-center distance (μm)
500	50	820 ± 40	2400 ± 100
500	100	1200 ± 50	3000 ± 100
500	150	1430 ± 60	3000 ± 100
1000	100	1130 ± 60	5800 ± 500

This results in significantly reduced emulsion droplet size.[306] This transition was not observed with the water in hexadecane emulsification using the open channels reported here. Rather, increasing the outer flow rate, while maintaining a constant inner flow rate, only increased the spacing between the emulsified droplets without significantly changing the droplet diameter (Figures 7.5b,d, Table 7.2).

Monodisperse particle generation was also achieved within our open-channel microfluidic devices by the *in situ*, photo-initiated, cross-linking of droplets produced by the emulsification of a precursor solution. This precursor solution was composed of polyethylene glycol diacrylate (PEGDA, Mn = 700), with 1 wt.% 2-Hydroxy-2-methyl-1-phenyl-propan-1-one as a radical photoinitiator, and 25 wt.% 800 μg/mL doxorubicin aqueous solution. The selection of doxorubicin as a model drug was based on its long-established use as a potent chemotherapy drug, its significant water solubility, and its bright color which facilitated visual observation of particles and UV-visible drug release studies.[318,319] The flow-focusing region was narrowed, as well as tapered, and the continuous phase channels were angled at 45° compared to the device in Figure 7.5 to enhance stable emulsification of the more viscous polymer precursor (Figures 7.6 & 7.7a). An inner flow rate of 10 μL/min and an outer flow rate of 750 μL/min was used in our experiments. After the emulsified aqueous phase droplets passed under a 365 nm UV LED spot lamp downstream of the flow focusing device, the droplets cross-linked into hydrogel microparticles (Figure 7.7a). The microparticles were then collected and analyzed. As the droplets were confined by the shallow liquid film in the channel, when cross-linked, the resulting hydrogel microparticles possess a morphology similar to flattened disks (Figure 7.7b,c).[320] The particles were also noticeably elongated and skewed along one axis due to the shear force in the flow direction (725 ± 30 μm × 560 ± 30 μm).

The size of the microparticles could be altered by altering the flow conditions within an open-channel device, possessing a fixed geometry (Table 7.3). While holding the outer flow rate constant at 750 μL/min, increasing the inner flow rate to 15 and 25 μL/min yielded larger particles. These particles are shown in the left and middle panels of Figure 7.7d. Additionally, reducing the outer flow rate to 500 μL/min, with an increased inner flow rate of 15 μL/min also made the particles significantly less skewed along the flow direction, reducing the aspect ratio (Table 7.3). The evaluation of drug release from the doxorubicin-loaded particles in Figures 7.7b,c was performed by

Table 7.3: Dimensions of particles from open-channel emulsification of PEGDA-25% aqueous doxorubicin solution in hexadecane, as shown in Figure 7.7.

Outer flow (μL/min)	Inner flow (μL/min)	Particle major axis (μm)	Particle minor axis (μm)	Aspect ratio
750	10	730±30	560±30	1.29
750	15	1260±30	980±30	1.29
750	25	1600±80	1200±100	1.31
500	15	1080±60	950±50	1.13

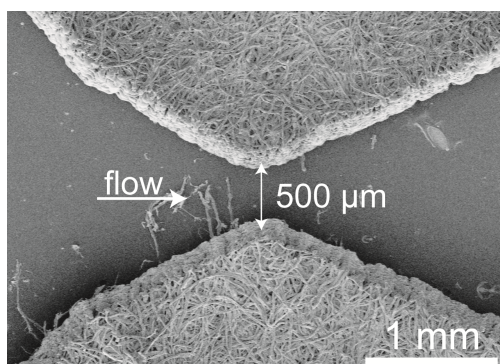**Figure 7.6:** An SEM micrograph for the flow-focusing region on the device used for drug delivery particle fabrication (nozzle width 500 μm). This modification was made to reduce the particle size and improve the emulsification stability with the more viscous polymer precursor solution.

placing 350 mg of dry particles into a vial with 2 mL deionized water. Visible absorbance spectra were periodically collected from 1 mL of the supernatant transferred to a cuvette, then returned to the vial. The absorbance at the 499 nm peak was compared to a reference curve generated by measuring aqueous doxorubicin solutions of known concentration. This allowed for the determination of the percent of the drug present in the particles, as well as the amount that was released into the solution (Figure 7.7e).

7.5 Conclusions

In conclusion, we have fabricated the first open-channel microfluidic devices capable of water-in-oil emulsification. This capability was enabled by the combination of a superomniphobic background, and channel walls which are simultaneously hydrophobic and oleophilic. The robust all-liquid repellent, superomniphobic fluoro-paper kept all liquids, including the low-surface-tension outer organic phase, from overflowing from the open fluid channels, even at high flow rates. The hydrophobic and oleophilic laser-cut and plasma-treated sidewalls and b-PDMS floor of the open channels greatly enhanced the flow rate of the continuous organic phase, enabled the emulsification of the aqueous phase, and prevented the aqueous phase from pinning on various surfaces of the microfluidic device. We also utilized the fabricated open channel devices for the fabrication of
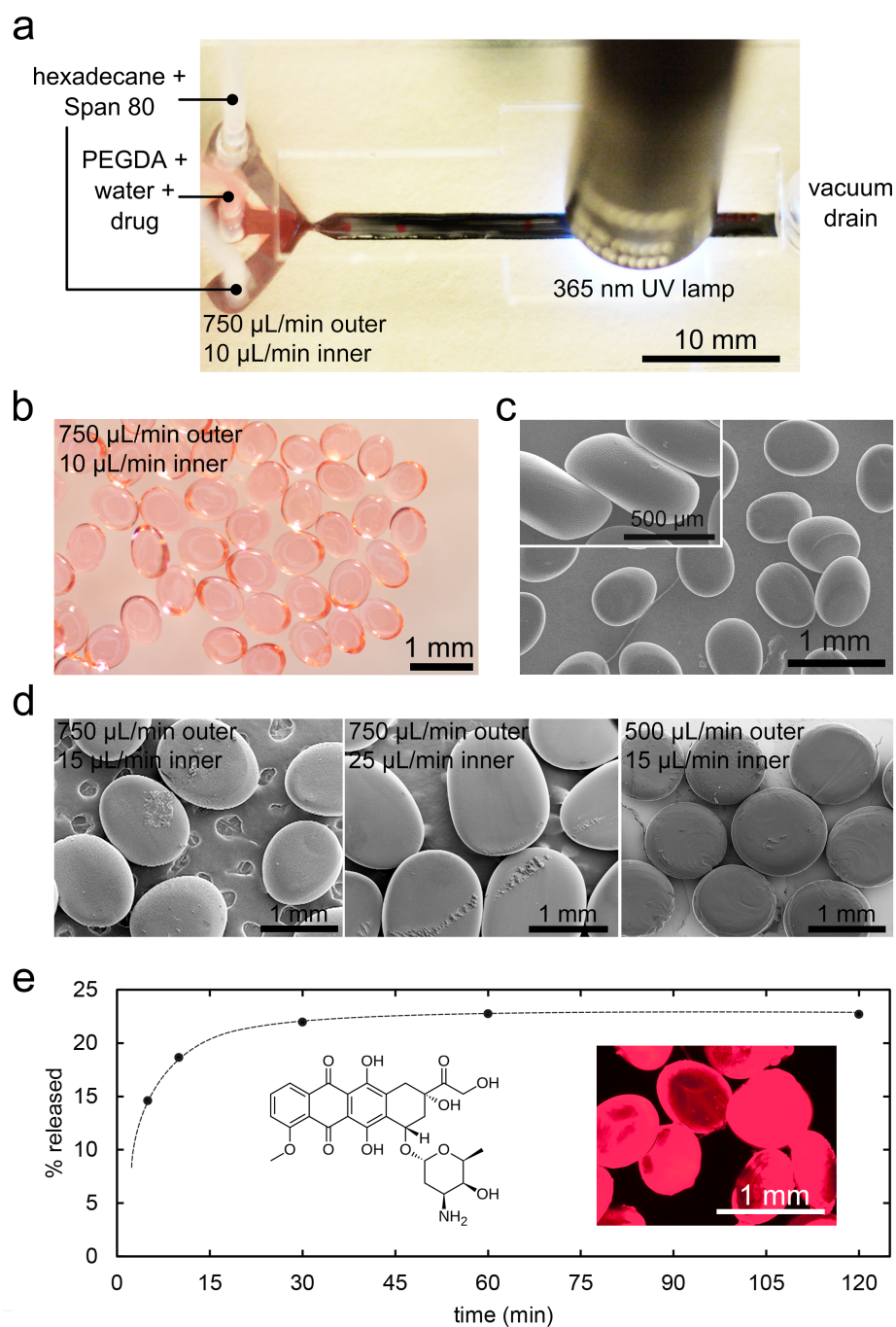
Figure 7.7: (*a*) An optical image of the emulsification device, modified with a UV lamp for the fabrication of doxorubicin-loaded PEGDA hydrogel microparticles (dispersed phase: 74.3% PEGDA, 0.7% photoinitiator, 25% 800 μg/mL aqueous doxorubicin solution, continuous phase: 10 wt.% Span 80 in hexadecane). (*b*) An optical image and (*c*) scanning electron micrographs for the microparticles fabricated using our open channel water-in-oil emulsification device. (*d*) Doxorubicin release profile obtained by monitoring light absorbance of water above a known mass of particles. Insets show the structure of doxorubicin and a fluorescent micrograph of doxorubicin-loaded PEGDA microparticles.

hydrogel based, relatively monodisperse microparticles capable of incorporating doxorubicin, a hydrophilic chemotherapy drug. This work represents an extension of the capability of low-cost, rapidly-produced, open channel microfluidic devices to fabricate hydrophilic microparticles for drug delivery, and potentially the encapsulation of cells within different polymers, both of which are highly desirable within the biological and biomedical fields.

7.6 Acknowledgements

<div style="text-align: center;">

CHAPTER 8

Microfabricated, Open-channel Microfluidic Devices on Nanotextured Silicon

</div>

This chapter briefly presents a prototype for a photolithographic method for fabricating open-channel microfluidic devices in silicon, with dimensions which are roughly an order of magnitude lower than those of the devices in Chapters 6 & 7.

8.1   Introduction

While the previous two chapters on open-channel microfluidic devices pushed the boundaries of the minimum γ_{LV} liquid that may be constrained and discussed the broad range of applications that this ability enables, the fabrication methodologies (plasma-patterning, printing, laser-cutting) remain relatively imprecise, producing channels with widths down to 200 μm at best. This is limiting especially for flow-focusing emulsion generation, as droplets generated in these devices at stable flow rates were still practically at the millimetric scale, whereas the most attractive biomedical applications of such monodisperse particles would require particles at least an order of magnitude smaller.

Conventional closed-channel microfluidic devices typically use photolithographic processes performed in cleanroom environments to fabricate molds from cross-linked photoresist, such as SU-8. These molds are then used to fabricate channels in poly(dimethyl siloxane). Bonding the PDMS structures to glass substrates then creates closed micro-capillaries of the desired geometry, with minimum channel widths as low as a few micrometers. To explore the limits of open-channel microfluidics, we developed a method capable of fabricating channels with near-ideal wettability contrast with most liquids, *i.e.*, $\theta_a^* \gg 0°$ on the background, and $\theta_a^* \approx 0°$ within the channel, down to channel widths of 25 μm.

8.2   Fabrication Method

A schematic of the fabrication process is shown in Figure 8.1. Nanoscale texture was desired both on the background and within the channels to enhance non-wetting, and wetting respectively. While the background would be coated with a fluorinated silane to yield maximum θ_a^*, the channels

<div style="text-align: center;">

129

</div>

would be selectively coated with photoactive TiO_2 to yield superomniphilic channels. Patterned devices were produced with or without sidewalls in addition to wettability contrast. Microfabrication was performed in the Lurie Nanofabrication Facility, generally following standard protocols.

Silicon wafers (University Wafer, P-type, test grade, 500 μm thickness, 1.5 nm native oxide layer, ⟨100⟩ orientation) were pre-cleaned with oxygen plasma and then first exposed to an anisotropic plasma etch in a combination of sulfur hexafluoride and oxygen in a STS Pegasus 4 DRIE tool. This produces a dense array of anisotropic nanostructured silicon, known as nanograss, or "black silicon" due to its non-reflective properties which has found use in a variety of applications, including solar cells.[321,322] Increasing SF_6 was found to increase the density of these nanostructures, but limited the etched area to the center of the wafer, whereas increasing O_2 spread the etched area outwards but greatly reduced the nanograss density at the center. It was found that the optimal etch conditions in this tool was a multiple step method, with 1200W coil power, 40W platen power, 35 mTorr chamber pressure throughout, with 3 min 225:200 sccm SF_6:O_2 to etch the outer edge, followed by 1.5 min 275:200 sccm SF_6:O_2 to fully etch the center.

This completely etched wafer was then patterned with positive photoresist (Shipley SPR 220-3.0, 3 μm thick) to define the channel geometry. Figure 8.2 is an image of the mask, where the black regions represent the photoresist as well as a diagram of the emulsification device used for testing. It contains several flow devices as well as a number of straight channels for testing. The flow focusing device is based on the design used in Figure 7.7a, but miniaturized. The overall dimension is 30 mm × 9 mm. There are two, rather than three, inlets the center one for the dispersed phase and the outer one for the carrier phase, as well as an outlet port. The flow-focusing orifice width varies from 15 μm to 200 μm, and the rest of the channels are 350 μm wider than the width of the constriction, yielding an ~40°angled taper into and out of the constriction. This geometry was transferred to an inexpensive emulsion-on-polyester film photomask (Advance Reproductions).

For the channels with sidewalls, a standard Bosch process etch (STS Pegasus DRIE) was then used to anisotropically etch the exposed silicon, yielding 50 μm deep channels with vertical sidewalls, while the nanograss on the background was protected by the photoresist. Then, a second nanograss etch was performed to maximize roughness within the channels to enhance wettability. For the channels without sidewalls, these two steps were omitted.

Next, physical vapor deposition of a 100 nm thick film of titanium dioxide was performed in an Angstrom Engineering Evovac electron beam evaporator. This highly directional deposition coated the bottom of the channels better than the sidewalls, but some accumulation was observed throughout in SEM (Figure 8.4).

Finally, the photoresist was stripped in a bath of N-methylpyrrolidone (NMP) held at 100 °C. A probe ultrasonicator was used to remove residual photoresist and TiO_2, and was particularly necessary for channels without sidewalls, as TiO_2 covering the edge of the photoresist strongly
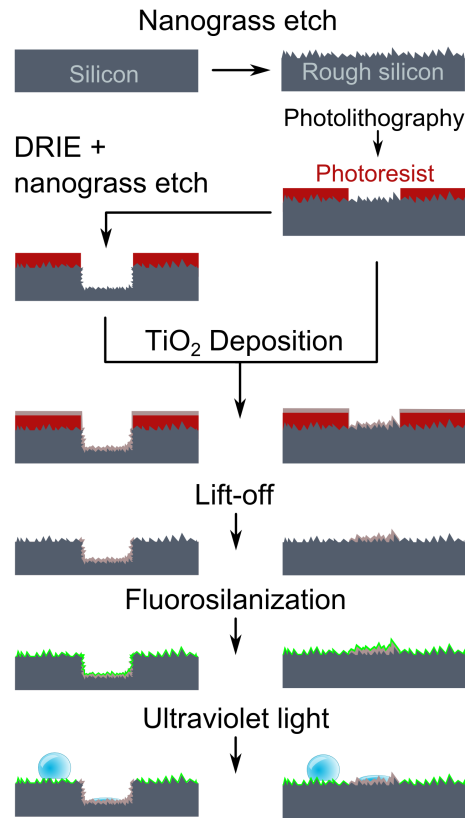
Figure 8.1: Schematic of the lithographic fabrication process to produce superomniphilic TiO_2-coated silicon nanograss channels or trenches on a superhydrophobic/oleophobic fluorosilanized silicon nanograss background.
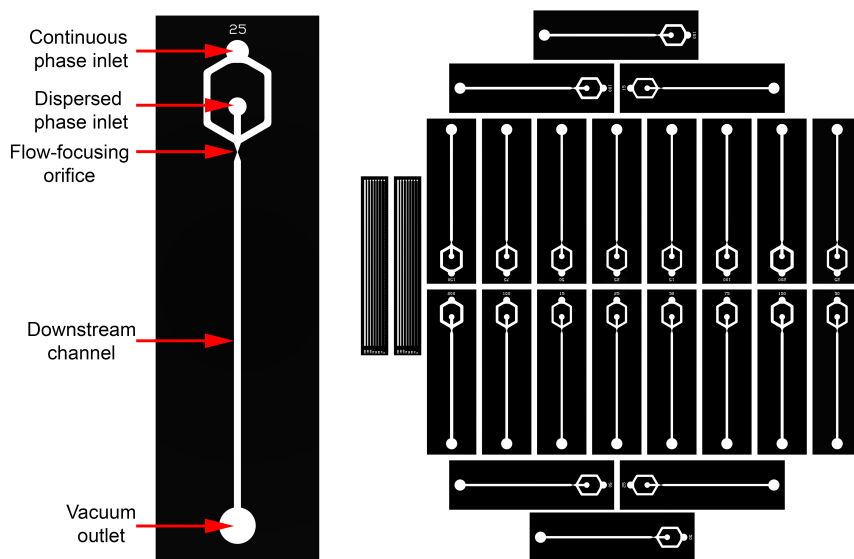

Figure 8.2: Diagram showing the design of a flow-focusing device, as well as the overall mask layout.
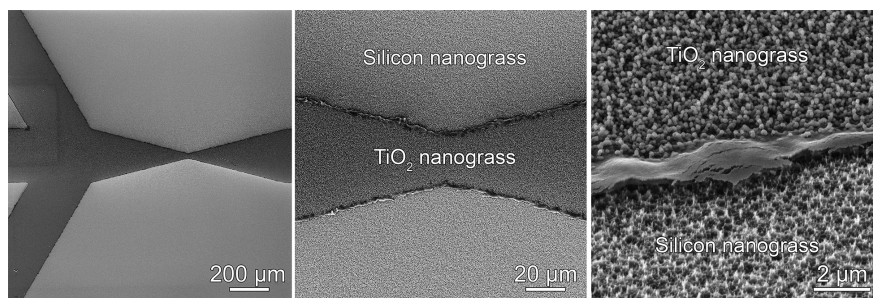
Figure 8.3: SEM images of the bare silicon nanograss and TiO$_2$-coated nanograss in a planar emulsification device. The residue at the edge of the channel is likely to be TiO$_2$ which was on the photoresist sidewalls and was not completely removed.

adhered it to the substrate. Samples were rinsed thoroughly with water while removing from the NMP bath to prevent accumulation of particles, then rinsed with isopropanol and dried with air. Fluorosilanization was performed by first cleaning the surface with low power oxygen plasma (30W, 15 min, Harrick Plasma PDC-001) and exposing the wafer to a vapor of perfluorodecyltrichlorosilane (Gelest) for 3 h at 120 °C under a cover on a hot plate. At this stage, the entire wafer was non-wettable, as both SiO$_2$ and TiO$_2$ react well with chlorosilanes. However, three hours of exposure to 254 nm UV light caused the photoactive TiO$_2$ to selectively degrade the fluorinated silane, yielding highly wettable superomniphilic channels.[323] This UV exposure process could be used repeatedly whenever channels become contaminated to completely restore their wetting properties. After exposure, channels retained their superomniphilicity for at least several days when stored in ambient light in air.

Emulsification tests were performed by flowing liquid into the inlets with syringe pumps (KD Scientific KDS 200) attached to poly(tetrafluoroethylene) tubing, which connected to 21 gauge stainless steel needles held just above the device inlets in a laser-cut poly(methyl methacrylate) block. Another PTFE tube was held above the outlet, and connected to a dry vacuum pump via a glass jar acting as a catch basin, in order to keep the device from flooding. The entire assembly could be tilted so that gravity could assist with stable emulsification.

8.3 Results

8.3.1 Structures

Figure 8.3 shows the structure of the planar channels. The reason for the color change on the channel backgrounds after applying and then stripping the photoresist is unknown. There was no readily apparent change in the nanotexture in SEM relative to pristine silicon nanograss. There was also no detrimental effect on the non-wettability of the background. The nanograss within the channels was rounded due to the deposition of TiO$_2$, but most of the roughness remained intact. Some residual photoresist and planar TiO$_2$ is observable at the boundary between the channels and background.
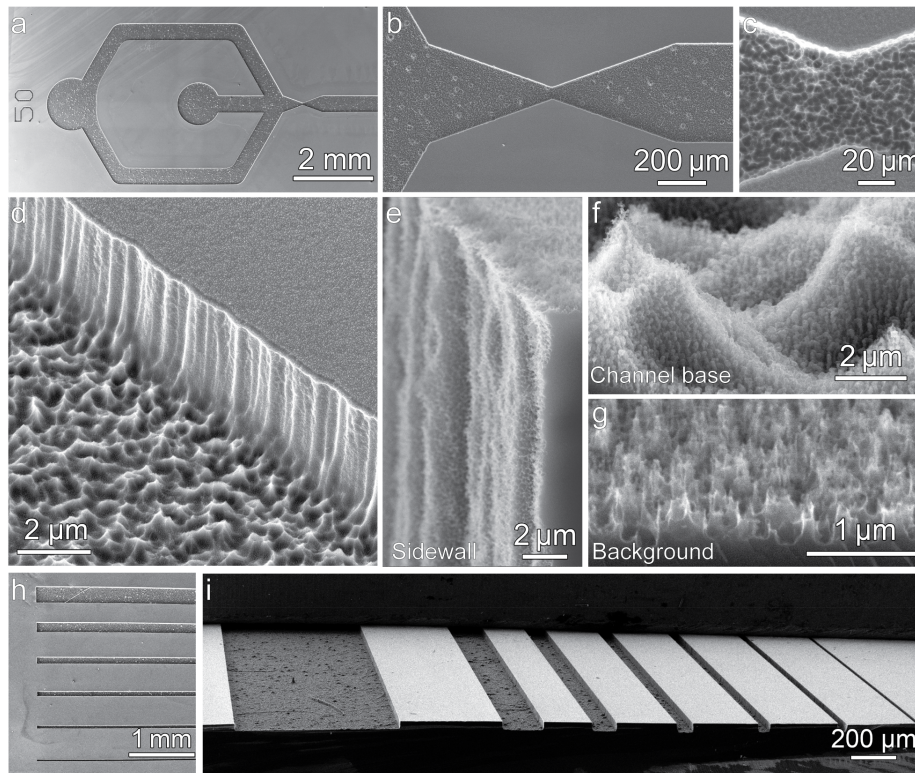
Figure 8.4: SEM images of the trench geometry devices and test channels. (*a–c*) Note the better definition of the edges of the channels than in Figure 8.3, as the deep groove effectively undercuts the photoresist on the background and makes lift-off significantly more effective. (*d*) The difference in texture of the nanograss at the base of the channel compared to the initial nanograss etched on a smooth wafer is evident, but doesn't seem to have significant consequences for wettability. (*e–g*) Close-ups of the sidewalls, channel base, and background. The silicon nanograss is finely textured and has sharp edges, which are rounded by the deposition of TiO_2. Due to the highly directional deposition, the sidewalls are coated much less than the base. (*h,i*) Images of the test channels of widths including 200,150,100,75,50, and 25 μm showing consistent etch depth to 50 μm and well-defined sidewalls.

Table 8.1: Contact angles of various liquids on the fluorosilanized silicon nanograss background

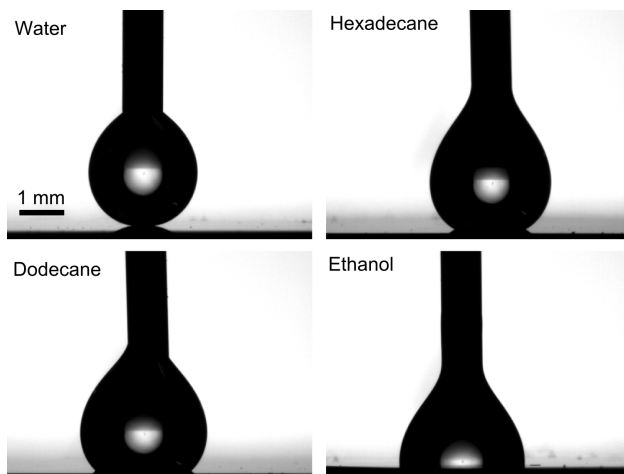| Liquid	γ_{LV} (mN/m)	θ_a^*/θ_r^* (°)
Water	72.1	171/169
Hexadecane	27.5	153/0
Dodecane	23.8	138/0
Ethanol	22.1	90/0

Figure 8.5: Goniometer images of water, hexadecane, dodecane, and ethanol advancing contact angles on the fluorosilanized silicon nanograss

Figure 8.4 shows the structure of the trench channels. Reasonably well defined 50 μm deep channels were obtained down to the 25 μm width, but the 10 μm. Aside from the rounding due to TiO$_2$ deposition within the channels, as on the planar samples, the nanograss on the channel base has a distinct texture compared to that on the background. It is very likely that the trenches affect the behavior of the second nanograss etch as they affect the flow of the reactive gases in the plasma-etching tool.

8.3.2 Wettability

The fluorosilanized silicon nanograss background exhibits very high advancing contact angles due to its low surface energy and high roughness (Figure 8.5). Contact angles with various liquids are reported in Table 8.1. However, the lack of re-entrant geometry means that the background does not maintain low-γ_{LV} liquids in a low-$\Delta\theta$ Cassie-Baxter state. As long as the channels do not overflow, this is not a significant concern. Fabricating nanoscale re-entrant texture would be significantly more difficult to incorporate into this lithographic process. Any contamination in the background with wetted liquids could be readily removed with volatile organic solvents such as acetone if necessary.

The TiO$_2$ coated nanograss, after silanization and exposure to UV, was ideally superomniphilic, exhibiting $\theta_a^* \approx 0°$ with all liquids (Figure 8.6). However, within the narrow channels still exhibited a finite advancing contact angle with water despite the clear presence of a condensed vapor front
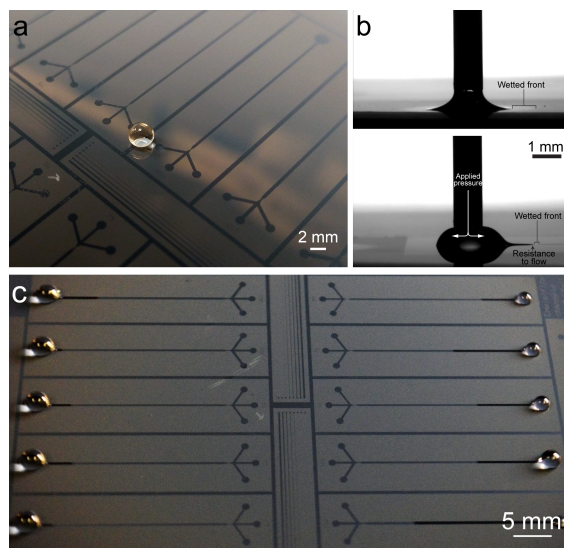
Figure 8.6: (*a*) Water droplet on a fluorosilanized planar substrate prior to UV, showing that the backgrounds and channels are all highly non-wetting. (*b*) Top: water on a silanized TiO$_2$ substrate after 3 h UVC exposure. If the drop were released from the needle, it would spontaneously spread into a thin film. Note the wetted front around the edge of the droplet where vapor from the droplet is condensing on the substrate. Bottom: however, the same material in a planar channel which is 400 μm still exhibits a finite resistance to wetting under pressure driven flow, as indicated by a non-zero contact angle behind the wetted front. (*c*) This resistance to wetting means that channels do not spontaneously fill with water even when there is a Laplace pressure applied from a curved droplet. The length of wetting is also erratic due to the presence of defects in the channel that impede wicking.

ahead of it. This hemi-wicking behavior was found to be insufficient to permit water to flow at high rates within the narrowest channels, and also would not allow it to spontaneously wet the entire downstream channel, let alone wick past the flow-focusing orifice. Pressure-driven flow rates with water were extremely limited, < 15 μL/min through the 50 μm wide device even when it was tilted by 45°to drive the flow forwards with gravity. This compares poorly to the hybrid device in Chapter 7, which achieved outer flow rates of > 750 μL/min with hexadecane without tilting the device.

Subsequent experiments focused on the trench geometry. In agreement with the findings in Chapter 7, the addition of side-walls to the open wettable channel greatly improved wettability by all liquids, and in this configuration both water and hexadecane would readily wet the entire device when a 5 μL droplet was placed into the central inlet, even through the 15 μm wide $\times$ 50 μm deep constriction (Figure 8.7). Wicking times were significantly faster for devices with wider orifices, *e.g.*, for the 100 μm wide $\times$ 50 μm deep device, water wicked to the end in 1.2 seconds and hexadecane in 13.7 seconds. Note that water wicks significantly faster than hexadecane, which consistent with wetting in a fully-wettable capillary according the Washburn relation (Equation 6.1), as opposed to the partially wettable capillaries with finite contact angles produced by selective oxygen plasma in Chapter 6. Under pressure-driven flow, water flow rates of 50 μL/min were achieved through

the 50 μm wide × 50 μm deep orifice with the channel held horizontally, which is reasonable considering that the cross-sectional area of this orifice is only about 6% of the one in the laser-cut device in Figure 7.6.
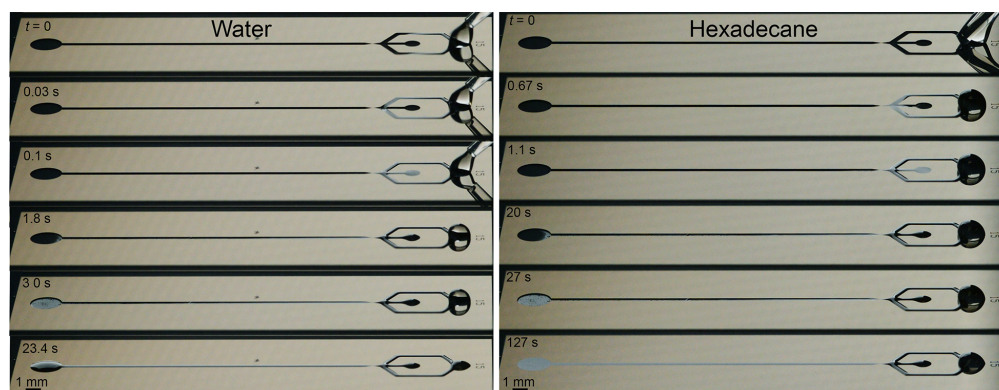
Figure 8.7: Timelapse photographs of water and hexadecane wetting 50 μm deep trench emulsification devices with 15 μm wide flow-focusing orifices. Due to the higher viscosity of hexadecane, it is considerably slower despite its lower surface tension.

8.3.3 Emulsification

The 100 μm wide × 50 μm deep device was used to generate microscale droplets of hexadecane, dyed with oil red O, in a carrier fluid composed of water + 2 wt.% sodium dodecyl sulfate (SDS) surfactant (Figure 8.8). The aqueous flow rate was 15 μL/min, and the inner flow was 0.1 μL/min, and appears to produce droplets with diameters comparable to the 100 μm wide orifice. The droplet production rate was too fast to capture without high-speed videography. In both of these respects, the performance of these devices far exceeds that of the paper-based devices demonstrated in the previous chapters. Further quantitative characterization is necessary. Future work will focus on generating water-in-oil emulsions and cross-linked particles from UV-curable acrylates such as TMPTA and PEGDA, as well as bio-medically relevant hydrogels such as agarose and calcium alginate. These microparticles could be ideal for capturing single viable cells for subsequent culturing and analysis.

Figure 8.8: Photograph of flow-focusing emulsification of hexadecane in water in an open-channel device with a 100 μm wide, 50 μm deep orifice.

CHAPTER 9

Spheroidal Cell Culture on
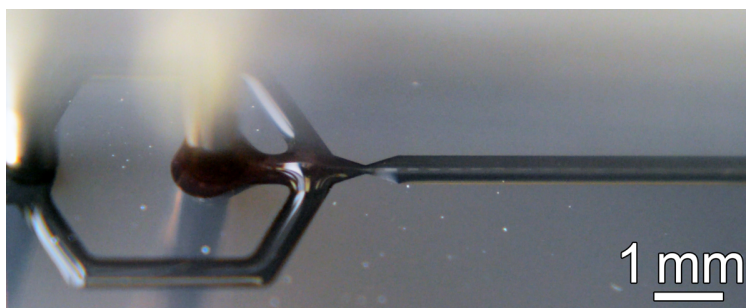# Hierarchical Superhydrophobic Surfaces

This chapter briefly outlines a method for fabricating a surface capable of maintaining stable droplets of media containing cancer cell cultures in the Cassie-Baxter state for extended periods. The curvature of the droplet and limited solid-liquid contact causes the cells to aggregate into spheroids, which are more accurate models of tumor growth *in vivo*. This approach improves stability and ease-of-use relative to existing hanging drop plates. This is a collaborative effort with Prof. Geeta Mehta. Pooja Mehta performed the cell culture experiments. Alex Kate Halvey assisted with substrate design and fabrication.

9.1   Introduction

9.1.1   Background

The evaluation of potential cancer therapeutics requires rigorous, high-throughput screening to test their efficacy with broad range of variables and a large number of replicates to ensure statistical validity. The prohibitive cost and time required for clinical trials in humans limits their use to treatments which have the highest chance of success. Testing in animal models is also time-consuming, and questions have been raised about their relevance to human biology in light of false positive results later contradicted in human testing. It is therefore necessary to improve the ability of *in vitro* cell culture, which is comparatively rapid and inexpensive, to accurately reproduce *in vivo* cancer biology. This capability allows the rapid screening of drugs and drug delivery systems, allowing optimization of parameters prior to committing to extensive testing *in vivo*.[324–326] Additionally, rapid and accurate replication of cancer biology *in vitro* could enable greater individualization of treatments. Cancer biology is frequently highly complex, and varies from patient to patient. A small number of cancer cells extracted from the patient may be used to generate large populations of three-dimensional cell cultures. This enables precise study of a genetically pure cell line, as well as potentially enabling rapid screening of therapeutics for their efficacy before treating the patient.[327,328]

It is now well-known that conventional two-dimensional cell culture fails to capture important aspects of how cancer cells grow and differentiate *in vivo*, due to key differences in the environmental conditions. Numerous methods have been developed that attempt to replicate the *in vivo* microenvironment, in terms of geometry, mechanical properties, and surface chemistry. Various porous scaffolds fabricated from biological materials or synthetic biocompatible polymers have been employed with varying effectiveness to stimulate cells to accurately reproduce native tissue. However, it is simpler to generate and image free-floating spheroidal cell cultures, and they are more likely to accurately reproduce *in vivo* behavior as no foreign extracellular materials are present that could their biology. The cells self-organize into free-floating microscale spherical aggregates which closely resembles the early growth and propagation stage of some malignant cancers. Such spheroids better reproduce critical physiological conditions such as the diffusion of oxygen, nutrients, waste, and drugs which are insufficiently replicated by two-dimensional cell cultures.[329,330] Additionally, spheroids may be used with microfabrication techniques to rapidly generate complex tissues.[331]

There are numerous ways of producing spheroidal cultures, including well plates with non-adhesive surface treatments, agitated culture vessels, hanging drops, and microfluidic devices.[325] Of these, hanging drop plates are relatively common, as they are relatively simple and can produce individual spheroids in each drop, enabling precise assays.[330,332] Typically, individual 10–20 μL droplets of cells in media are adhered to some hydrophobic, but high-$\Delta\theta$ surface (such as a polystyrene petri dish lid, a PDMS microfluidic device, or a high-$\Delta\theta$ superhydrophobic polystyrene surface). The substrate is inverted during cell culture such that the bottom surface of the droplet, where cells tend to aggregate due to gravity, only contacts air and prevents cell attachment. The high curvature of the droplet, due to the hydrophobicity of the substrate, also accelerates cell aggregation into a spheroid. Specialized commercial high-throughput hanging drop plates now exist. The key drawback of this suspended configuration is the risk of droplets falling or spreading during routine plate handling. This could be catastrophic for a spheroidal culture experiment which can take several days to weeks to complete. Replacing the air interface at the base of the hanging drop with a superhydrophobic substrate should significantly improve the stability of such a system and prevent such loss of time and effort.

9.1.2   Design of a Superhydrophobic Spheroidal Cell Culture Substrate

A deep well with a high θ^*, low-$\Delta\theta$ superhydrophobic surface that minimizes solid-liquid contact area could potentially replicate the performance of a hanging-drop plate, while retaining the inherent stability of a conventional well plate. While a droplet in a superhydrophobic well could oscillate or bounce due to mechanical shock, ideally it would return to its original location under gravity. To ensure spheroidal growth, the droplet must remain in a stable non-wetted Cassie-Baxter state for extended periods of time. Retaining superhydrophobicity in a cell-culture environment can

be challenging, however. Cell media contains salts and other additives that reduce its surface tension. Cells excrete proteins that can readily adhere to the hydrophobic substrate. The incubation environment is held at high relative humidity, to minimize the loss of droplet volume to evaporation. As previously discussed, under such vapor conditions, superhydrophobic surfaces are vulnerable to wetting due to condensation of droplets within the superhydrophobic texture itself.[56] The small, spherical droplet of culture media (typically < 20 μL) also applies some Laplace pressure on the entrapped air pockets. It is therefore important to fabricate a surface with very high robustness to wetting under pressure or condensation. As discussed in Section 1.2.5, this is done by reducing the smallest texture features to nanoscale dimensions.[63] Nanotextured superhydrophobic surfaces typically exhibit extremely low $\Delta\theta$ and high robustness to wetting even when immersed for extended periods at elevated pressures.[333–335]

Reducing the texture length scale below the wavelength of visible light also reduces light scattering, making such a surface effectively transparent. Inverted microscopes, in which the objective lenses point upwards through the sample, are commonly used in cell biology. Imaging spheroids from the underside of the droplet is preferable to limit image distortion, as cells tend to accumulate at the bottom interface due to gravity. A well plate uniformly coated with a transparent nanotextured superhydrophobic coating could be ideal for imaging. Numerous transparent, robust superhydrophobic surfaces have been previously demonstrated in the literature, using a wide array of methods.[57,105,107,124,336] Naturally, methods relying on photolithographic patterning are difficult or impossible to apply to a high-aspect ratio well capable of containing a mobile droplet on a low-$\Delta\theta$ superhydrophobic surface. Uniform application of a superhydrophobic coating with dip, spray, or spin coating methods to a well plate can also be challenging, due to the difficulty of applying a uniform thin film of coating solution and maintaining uniformity during drying. Bottom-up growth of superhydrophobic nanotexture could be more amenable to uniform, conformal deposition on high-aspect-ratio structures. There are numerous solution-phase or vapor-phase approaches that have been demonstrated to produce low-$\Delta\theta$ transparent superhydrophobic surface.[337,338] However, most of these require tight control over the deposition conditions to simultaneously optimize low $\Delta\theta$, high robustness, and high transparency.

Even if the superhydrophobic surface appears transparent to the naked eye, any material in the imaging path of a microscope can introduce distortion. In addition, certain fluorescent cell stains, such as DAPI, are excited by near-ultraviolet light,[339] which is absorbed by many hydrophobic organic materials. Therefore, it may be simpler and more effective to incorporate macro-scale pores below the droplet that allow completely unobstructed imaging through the base of the drop. An open mesh substrate crimped into a well array geometry, covered uniformly in nanotexture and a highly hydrophobic modifier, could be an ideal method for generating and maintaining cell spheroids *in vitro*.

Table 9.1: Nominal dimensions of aluminum meshes used in this work, and D^* as calculated using Equation 1.12

Mesh size	Wire diameter	Wire spacing	D^*
30×30	0.29	1.52	3.61
20×20	0.25	1.30	3.55
16×16	0.23	1.14	3.50
14×14	0.20	0.86	3.13
12×12	0.14	0.56	3.00

9.2 Superhydrophobic Surface Fabrication

9.2.1 Hierarchically Textured Fluorosilanized Aluminum

A highly pressure-resistant, hierarchically nanotextured superhydrophobic surface may be produced from aluminum by acid etching, then immersion in boiling water, then treating the surface with a fluorosilane to lower the surface energy. The process used was similar to that used for Surface # 4 in the drag reduction project (see Section 3.7), which in turn was adapted from methods previously reported in the literature for super-repellent surfaces.[139]

The substrates were 6061 T6 aluminum alloy plates or 5052 alloy aluminum meshes with varying dimensions (McMaster-Carr, Table 9.1). First, the surfaces of the plates and meshes were abraded with a fine wire brush, washed with soap and deionized water, then dried with compressed air. This removes any surface oxides and contaminants and exposes pure aluminum. To form wells to hold the cell culture droplets, the substrates were indented with a ball bearing (radius $\approx$ 3 mm) using a drill press. The substrates were then immersed in 2.5 M hydrochloric acid (Fisher Scientific) held at 60°C on a hot plate until they were uniformly etched and all of the original planar surface was removed. This created a micro-structured surface, most likely due to enhanced etching along the grain boundaries of the aluminum alloy.[340] Depending on the effectiveness of pre-cleaning, the exact aluminum alloy, and the geometry of the sample, complete etching was achieved between 5 and 20 minutes, and was monitored by periodic visual inspection of the sample. While there is some evident variation in the morphology of the microtexture due to variation of the effectiveness of the acid etch, this does not appear to have a significant effect on the water contact angles or pressure stability of the resulting superhydrophobic substrates. Following etching, the majority of loosely adhered aluminum particles were removed with a combination of agitation in a water bath sonicator, rinsing in water, and drying with compressed air. The etched aluminum was then boiled in deionized water for one hour, which caused the conformal growth of γ-boehmite (AlO(OH)) nano-platelets (Figures 9.1 & 9.2).

To make the etched substrates superhydrophobic, they were exposed to 1H,1H,2H,2H-Heptadecafluorodecyl triethoxysilane (Gelest) vapor for 48 h at 60 °C at ~5 mTorr in a vacuum

oven. All samples exhibited $\theta^* > 170°$ with $\Delta\theta$ approaching $0°$. All crimped meshes were capable of suspending 10 μL droplets of deionized water (2.7 mm diameter) with good stability except the 12×12 which had slightly excessive spacing and allowed droplets to penetrate (Figure 9.3). Note that the crimping and acid etching process can make meshes slightly sparser than the nominal initial dimensions, as the wires are inevitably distorted by the crimping process and slightly thinned by the etching process. The resistance to wetting of the samples under pressure and time was evaluated by placing the samples into a cylinder of DI water at a depth of 30 cm ($P \approx 3$ kPa). The samples appeared highly reflective, indicating the presence of trapped air, or a plastron.[2] While this diminished over time due to dissolution of the excess plastron into the water,[335] the surfaces remained completely non-wetted when removed from the water column > 30 h later.

9.2.2 Design for High-Throughput

To improve ease of handling, particularly during imaging, and increase overall throughput, we adapted the mesh substrates to a higher density multiwell cell culture plate form factor. Rather than crimping the meshes as described above, the sidewalls to contain the droplets were formed by drilling an array of sixty 6 mm diameter holes in a ~6 mm thick sheet of 6061 aluminum alloy, using standard 96-well plate spacing. This geometry improved lateral droplet confinement. The meshes and sidewalls were treated as described above to make them superhydrophobic. The meshes were clamped to the base of the sidewalls, using screws and laser-cut poly(methyl methacrylate) mounting plates, and secured within a modified well plate incorporating a water reservoir along its perimeter (Figure 9.4). This reservoir reduces droplet evaporation during cell culture by maintaining a saturated environment. This assembly was placed between a standard well plate lid and a 6 well plate filled with water, and the sides sealed with Parafilm during culturing. For imaging, the center assembly was removed from this bottom well plate, to accommodate the working distance of the inverted microscope used for imaging. All parts should ideally be re-usable with sterilization, and the meshes easily exchanged in the assembly if necessary.

9.3 Cell Culture and Imaging Methods

Cell culture reagents were purchased from Life Technologies, unless otherwise specified. Prior to any cell culture experiments, the substrates were cleaned by thoroughly washing in sterile phosphate-buffered saline solution (PBS) and deionized water, then sterilized with a germicidal ultraviolet lamp. Crimped planar and mesh samples were placed in polystyrene petri dishes during culturing. Excess water added to the dish adjacent to the superhydrophobic substrates to maintain high humidity. The multiwell plate was used as described above.

A high grade serous ovarian adenocarcinoma cell line, OVCAR-8 (provided by Dr. Nouri Neamati, University of Michigan), was used. Spheroidal culture was performed using previously published methods.[327,330] Cells were cultured in growth media until 70% confluency, then diluted to
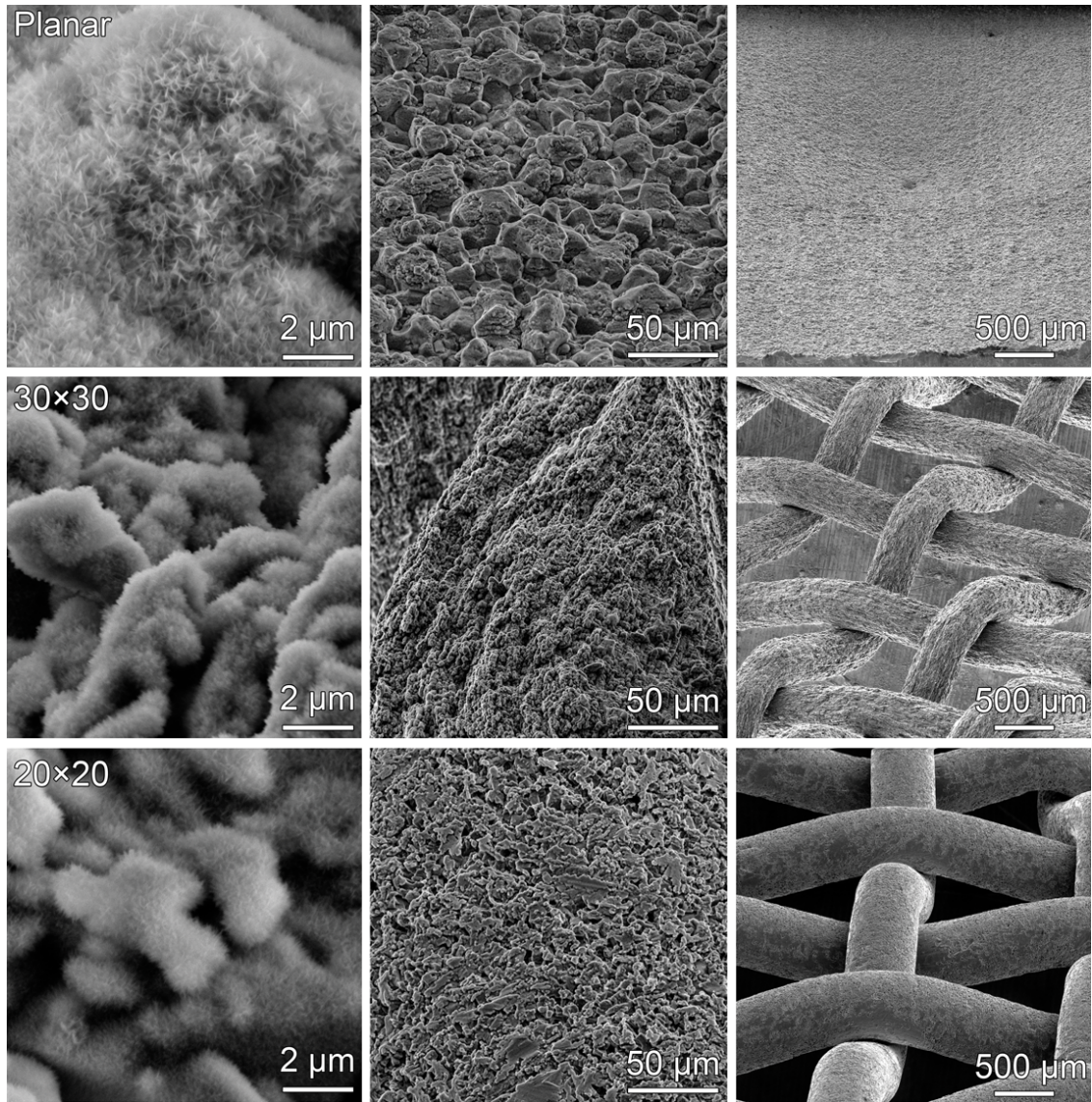
Figure 9.1: SEM images of the various length scales of texture on the finer scale substrates initially tested: etched, boiled, fluorosilanized aluminum plates, 30×30, and 20×20 meshes.
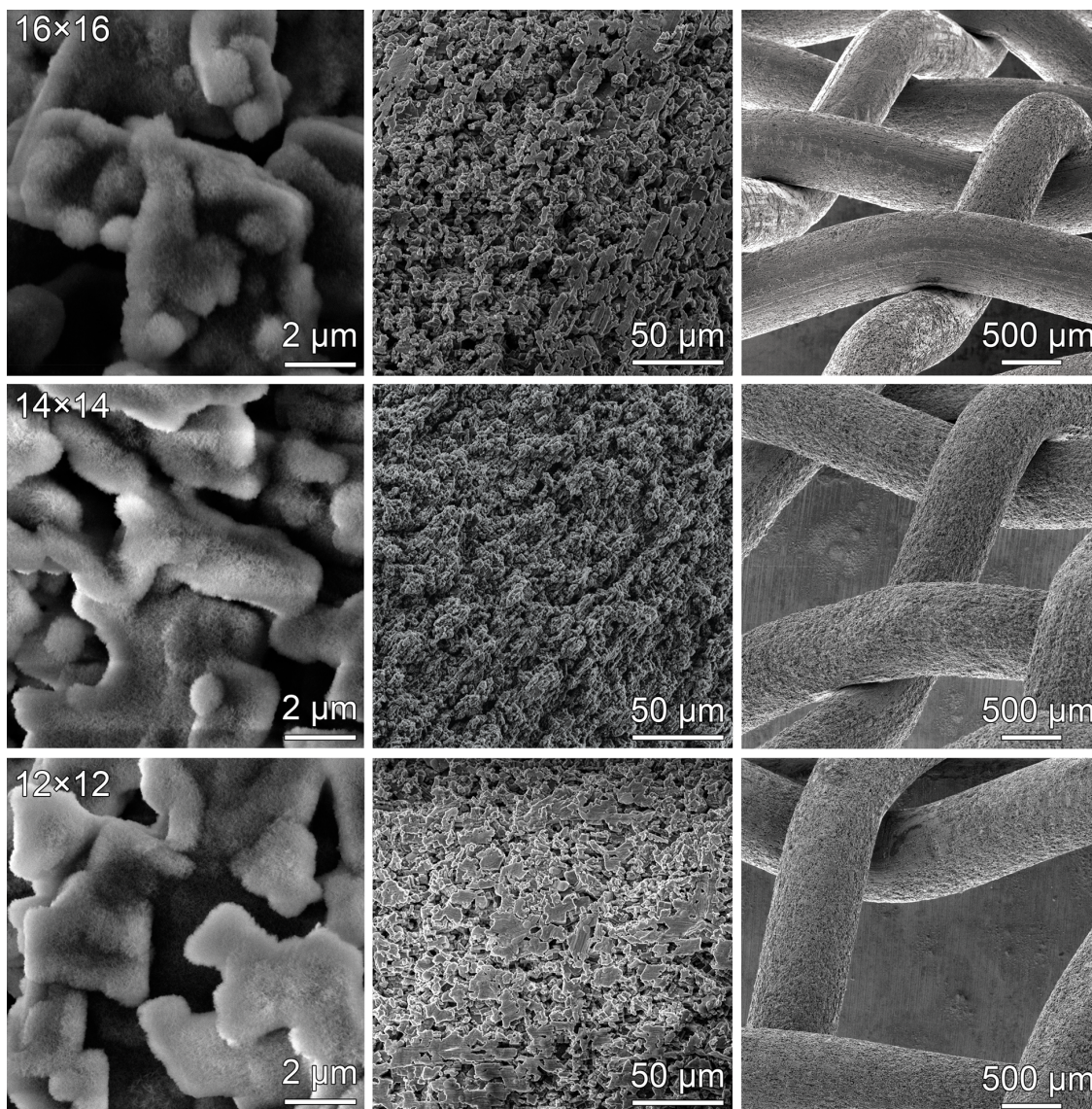
Figure 9.2: SEM images of the coarser etched, boiled, fluorosilanized meshes (16×16, 14×14, and 12×12).
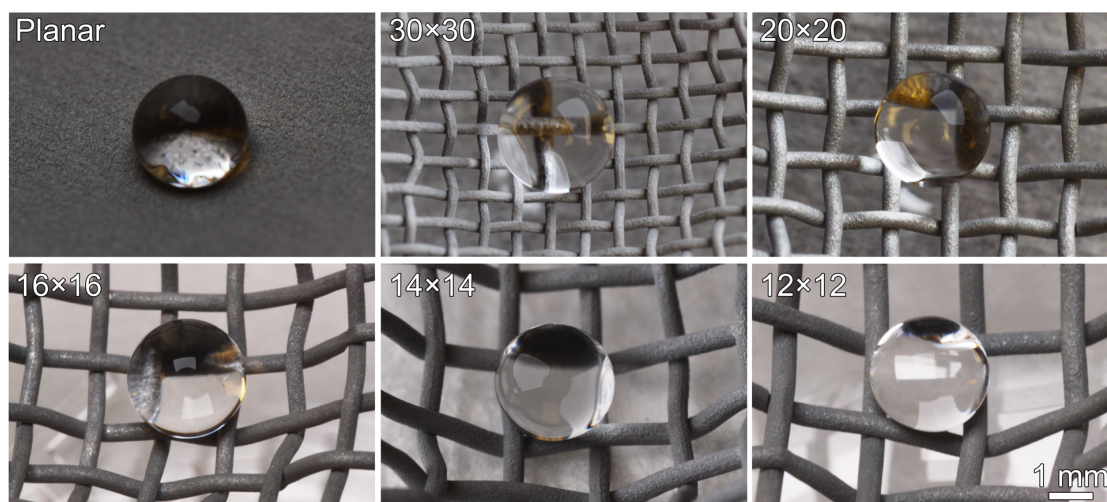
Figure 9.3: Photographs of 10 μL water droplets placed on the various crimped superhydrophobic substrates.
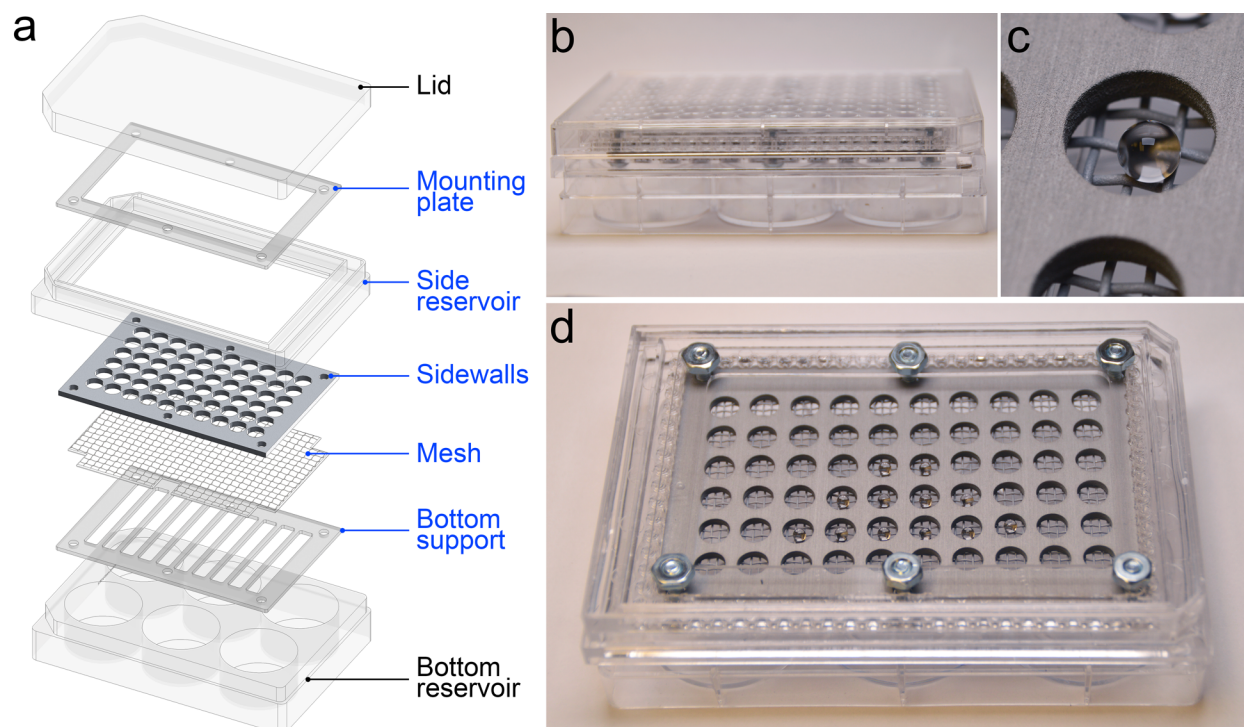
Figure 9.4: (*a*) Schematic of a superhydrophobic etched fluorosilanized aluminum well plate with mesh base for imaging. Photographs of: (*b*) the complete well-plate assembly; (*c*) a 10 μL water droplet in a well; (*d*) the central assembly, highlighted in blue on the schematic in (*a*).
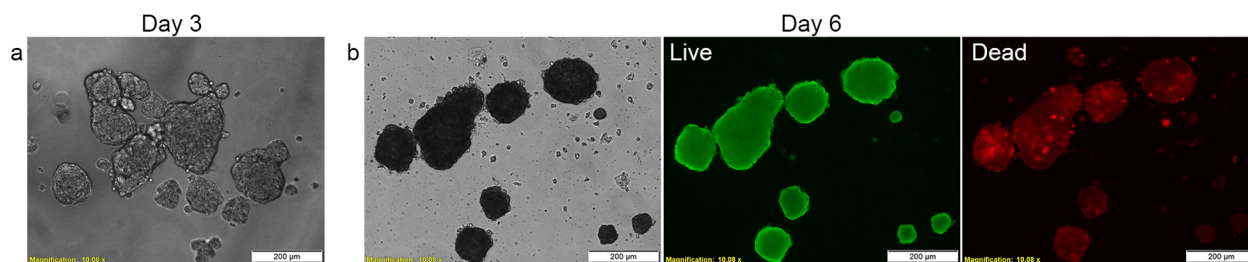
Figure 9.5: Micrographs of cells grown on the planar substrate taken after transferring droplets to a cover slip. (*a*) Bright-field image for day 3 (*b*) Bright-field and Live/Dead assay for day 6. No completely coalesced spheroids were observed.

the final seeding density of 500 or 1000 cells/10 μL droplet of media (RPMI 1640 supplemented with 10% fetal bovine serum and 1X antibiotics/antimycotics). Incubation was performed at 37 °C in a humidified in a 5% CO_2 atmosphere for up to seven days. Cell growth was monitored with periodic imaging, and cell medium was replenished on alternate days as necessary. Crimped mesh substrates in petri dishes could be imaged directly in the inverted microscope (Olympus IX81 equipped with an ORCA R2 cooled CCD camera and CellSens software). For *in situ* imaging in the fabricated well plate, the bottom reservoir plate was removed to accommodate the working distance of the microscope.

Cell viability was evaluated with a standard Live/Dead fluorescent assay (ThermoFisher Scientific). A staining solution of 8μM Calcein AM and 16μM ethidium homodimer-1 was introduced to the media droplet, with a subsequent incubation of 1 h. Viable cells were selectively stained fluorescent green with calcein-AM due to ongoing intracellular esterase activity, while the plasma membrane breakdown in dead cells enabled their DNA to be stained fluorescent red with ethidium homodimer-1. The stained cells were carefully transferred to glass coverslips and imaged using a laser scanning confocal microscope (Olympus IX81, equipped with a Yokogawa CSU-X1 confocal scanning laser unit, Andor iXon x3 CCD camera, and Metamorph 7.8 software), with constant gain and exposure settings between samples. Viable spheroidal cultures should only contain a few dead cells, primarily in the oxygen-deficient core.

9.4   Results

9.4.1   Preliminary Results

The initial trial on 30×30 crimped meshes and crimped aluminum sheets (Figure 9.1) yielded promising results. Cells began to aggregate by day 3 on both substrates. The separate spheroids on the planar substrate did not fully coalesce by day 6 (Figure 9.5). However, on the mesh, a fully coalesced spheroid formed in each droplet by day 6. The droplets were transferred to a coverslip for bright-field and fluorescent imaging (Figure 9.6).

The 16×16 mesh, with its significantly increased open area, significantly improved the rate of
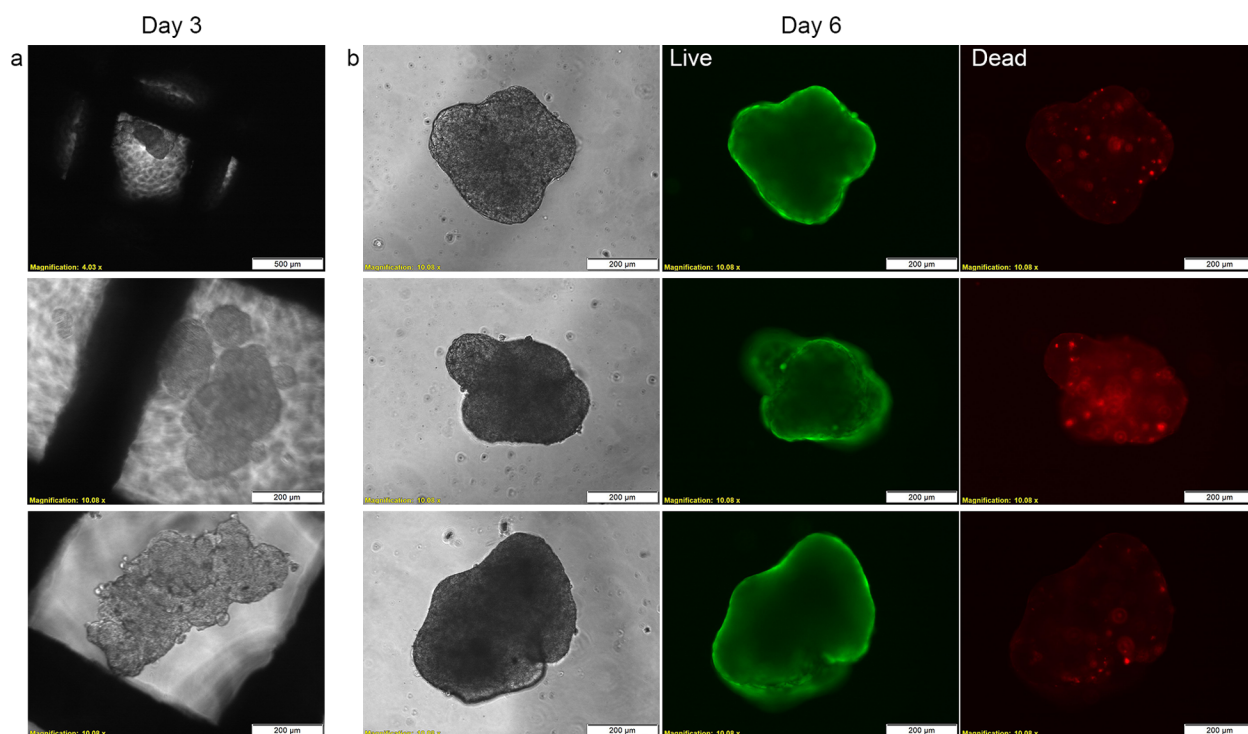
Figure 9.6: Micrographs of cells grown on the 30×30 crimped mesh substrate. (*a*) *In situ* bright-field image for day 3 and (*b*) Bright-field and Live/Dead assay images of single coalesced spheroids in three separate droplets after transferring to a cover slip at day 6.
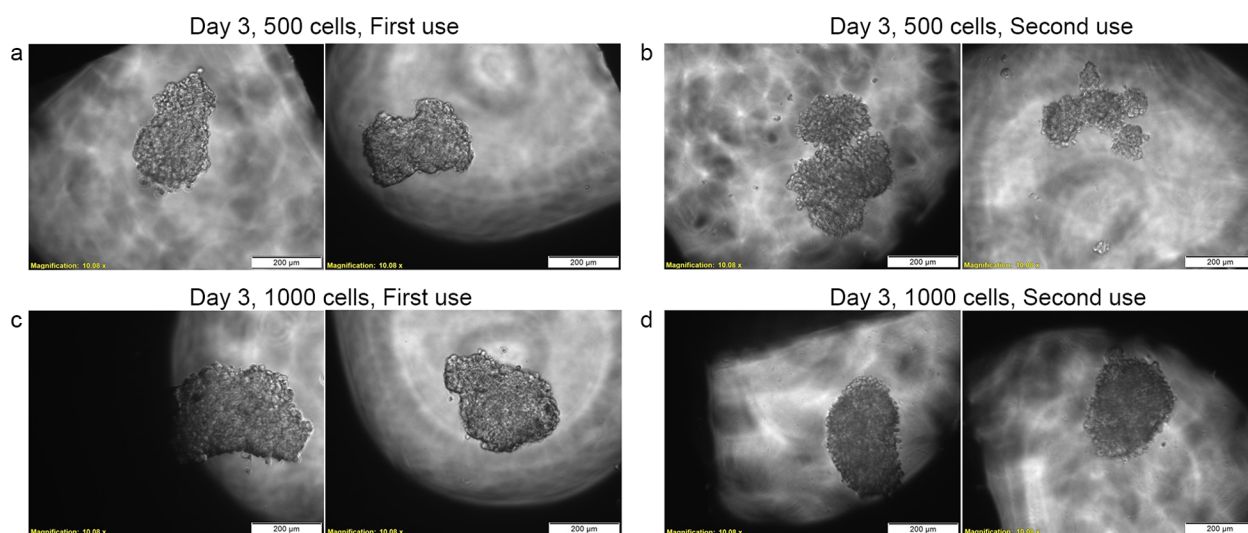
Figure 9.7: *In situ* bright-field micrographs of cells grown taken after three days of growth on the 16×16 crimped mesh substrate over two different trials. 500 cells/10 μL density, (*a*) first trial (*b*) second trial, and 1000 cells/10 μL density, (*c*) first trial (*d*) second trial.

146
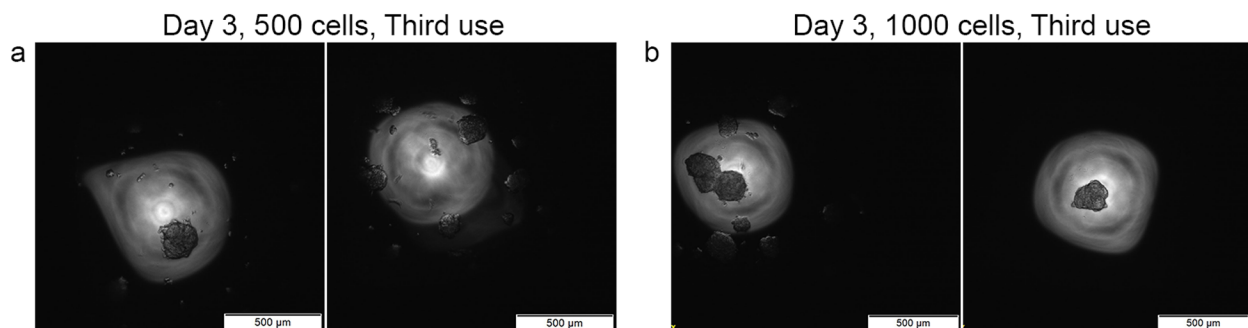
Figure 9.8: *In situ* bright-field micrographs of OVCAR8 spheroids taken after three days of growth on the 60 well plate with 14×14 mesh growth surface.

coalescence. Spheroids were fully-formed by day 3 in two separate trials on the same substrate with 1000 cells/10 μL, suggesting that the substrates can be successfully re-used to generate spheroids (Figure 9.7). However, 500 cells/10 μL yielded less consistent results. Attempting to grow cells on even coarser crimped meshes placed in petri dishes yielded unsatisfactory results. The 14×14 mesh apparently allowed the suspended droplets to partially contact the underlying petri dish. The cultures which were initially spheroidal started to spread when they contacted the flat dish. The 12×12 mesh proved to be too unstable for cell culture conditions, and all droplets passed completely through it to the underlying petri dish.

9.4.2 Ongoing work: Testing in Multiwell Plate

The 14×14 mesh was selected for initial testing. Though media droplets wetted the petri dish in tests on the crimped mesh, there was no apparent break-down of the non-wetted state, and it should function when no substrate is present immediately below the mesh. The first revision of the multiwell plate design used spacers laser-cut from standard 96 well plates, with no water reservoir around the perimeter. The excess air volume contained in this design prevented sufficient humidity to prevent droplet evaporation, causing them to shrink to films suspended within the mesh squares. Unexpectedly, cells apparently grew in a monolayer across the water film surface, spanning adjacent wires in the mesh. However, the well-array as shown in Figure 9.4 successfully prevented 15 μL droplets from evaporating for extended periods of time. Viable spheroids of OVCAR8 were successfully generated in this device (Figure -9.8), though spheroid quality and formation time was somewhat inferior compared to the earlier crimped plates and further optimization may be required.

Future work will focus on the validation of this platform for typical tasks performed with spheroidal cell cultures, including a chemotherapy drug assay, and co-culture with non-cancerous cells such as 3T3 fibroblasts, to study cell-cell interactions which are relevant to *in vivo* biology. Practical tests will also be performed, including stability testing to confirm improvement over conventional hanging drop plates. Preliminary testing to generate controlled lateral impacts with a pendulum showed that conditions which caused 25/25 20 μL water droplets to fall from a commercial

hanging drop plate caused only the merging of two droplets on the 60 well 14×14 mesh plate out of 25, showcasing the improved stability. Compatibility will be tested with large scale sterilization techniques, such as ethylene oxide, as well with automated plate readers. The reusability of these substrates over multiple sterilization and culture cycles will be tested. These tests may suggest future revisions to the plate design to further improve overall ease of use and functionality. Subsequent projects will focus on using the optimized platform for biological experiments with greater novelty.

CHAPTER 10

Summary and Future Outlook

10.1   Robust Omniphobic Surfaces

Surfaces capable of repelling a multitude of liquid and solid contaminants have a vast array of potential applications, some of which were discussed throughout this work. Longevity is critical for all of these usage areas; however, this issue is insufficiently explored in the literature. The work presented in this thesis has made some major strides in the design and fabrication of surfaces that are robust, in all senses of the word. They were subjected to mechanical abrasion, droplet impact or immersion in high-pressure flows, exposure to low-surface tension solvents, acids, bases, and even fluorinated liquids, irradiation, high temperatures, and micro-organisms and showed good retention of non-wettability in most cases.

However, much work remains to be done to produce a scalable, substrate-independent coating that simultaneously achieves all of the desirable characteristics: omniphobicity, solid-repellence, transparency, and robustness to a broad range of harsh environmental conditions. The surfaces in each of the first four chapters excelled in one aspect or another, but none were ideal for all applications. The hierarchical surface in Chapter 2 showed highly pressure-resistant superomniphobicity, but were neither scalable nor mechanically robust. The durable superhydrophobic coatings in Chapter 3 were not transparent, nor strongly pressure resistant, especially under high shear flows, and allowed low surface tension liquids to wet. The smooth omniphobic coatings in Chapter 4 repelled a broad range of liquids and are transparent, but remained vulnerable to elevated temperature, swelled or dissolved on exposure to some solvents, were far less durable than the textured superhydrophobic coatings, and were not ideally temperature resistant. The abrasion resistance requirements for a smooth omniphobic coating are far more stringent than that those for a textured superhydrophobic coating, as any surface scratching can greatly increase hysteresis with low surface tension liquids.

The grafted PDMS chains in Chapter 5 even repelled fluorinated liquids in addition to solids, appeared to be impervious to mild abrasion, were not irreversibly damaged when wetted, and were far more heat-resistant than the previous coating. However, they had significantly reduced contact angles and exhibited optimal $\Delta\theta$ only on select hydroxide-rich surfaces, and relied on a vapor-phase

deposition which may not be scalable to large substrates. Reducing solid adhesion remained largely unexplored in this work except on these grafted PDMS surfaces, but for many applications the repulsion of solid contaminants such as ice, polymers, wax, minerals, proteins, micro-organisms, and even larger organisms like barnacles, is even more critical than ensuring that most liquids can dewet. Studying the adhesion mechanisms of the more complex heterogeneous solids and producing surfaces capable of indefinitely resisting their attachment will require significant investigation. While liquid-like tethered polymers do appear to be promising, a single repellent chemistry may not be capable of producing a "truly omniphobic" surface, but perhaps mixed chemistries will.

Better understanding of the mechanisms by which grafted PDMS chains or densely-crosslinked PDMS repel liquids, especially those solvents that strongly swell elastomeric PDMS or dissolve linear PDMS, will be necessary to optimize these grafted surfaces. It remains unclear why certain strong solvents (*e.g.*, toluene) for PDMS readily recede from PDMS brushes while others (*e.g.*, hexane) spontaneously wet. Other liquids such as isopropanol consistently exhibit anomalously high hysteresis compared to very similar liquids such as ethanol and 1-propanol. One of a variety of highly surface-sensitive spectroscopy techniques may be able to reveal how the PDMS chains conform in the presence of different liquids.[341] Combining such a detailed investigation with a systematic study of different capping agents (alkyl chains with varying lengths, fluorinated alkyl chains, or other functional groups) may enable the development of brushes that repel a broader range of liquids with higher contact angles without compromising low solid adhesion.

There are a few potential routes to a generalizable and durable surface. The deposition of a hard PDMS elastomer, as mentioned in Section 5.7, may be one method to produce a durable smooth omniphobic coating, but such systems remain far too brittle to improve durability relative to FPU + F-POSS thus far. A vast array of additives exist for PDMS matrices alone, and thorough exploration of these reinforcing fillers, including modified inorganic nanoparticles, polyhedral silsesquioxanes, and reactive non-siloxane copolymers may yet reveal an optimal formula which is relatively impervious to abrasion damage and shows excellent adhesion to a broad range of substrates. More extensive synthetic approaches may be necessary to exceed the performance of existing commercial products, such as the synthesis of reactive reinforcing fillers, or the modification of matrix polymer components with reinforcing side groups prior to formulation and deposition. The combination of a sol-gel deposition of silicon dioxide and subsequent treatment with PDMS may also be an alternative to yield a substrate-independent modification technique. The matrix could also be a tougher polyurethane or epoxy polymer with grafted PDMS functionality - as long as the matrix resists scratching or disintegration, surface grafted PDMS chains may act as solid-state lubricants that reduce abrasion damage.

10.2   Marine Drag Reduction

The published work on drag reduction in turbulent flows discussed in Section 3.7 was enlightening as to the necessary properties for superhydrophobic surfaces that reduce rather than increase drag. However, ongoing testing suggests that maintaining a stable non-wetted state under unbounded, high pressure, high velocity, turbulent flow is even more challenging than previously expected. Scaling these coatings to the towed submersible model remains the subject of future testing, and the key requirement will be balancing the reduction of microscale roughness to reduce form drag while sufficiently shielding the nanoscale texture from damage. The development of new methods for scalable fabrication of geometries with segmented air pockets that resist plastron depletion under hydrodynamic shear could also be necessary, as the thick air layers initially visible on immersed coated surfaces seem to be vulnerable to lateral displacement under flow or pressure gradients.

Other challenges will arise from use in a marine environment: corrosion, bio-fouling initiated by various microorganisms, as well as other practical considerations such as ensuring that the fuel savings can justify the cost of materials and application. It may be necessary to combine active air-replenishment technologies such as air injection through porous substrates[151,342] and solid-repellent chemistries, such as the tethered PDMS brushes, to improve the long-term stability of drag-reducing superhydrophobic surfaces.

10.3   Open-Channel Microfluidics

Paper-based and open-channel microfluidic devices largely remain confined to the laboratory. The technologies in Chapters 6 – 7 are excellent demonstrations for the potential uses in chemical and biomedical analysis of novel open-channel devices with patterned omniphobicity and could be useful for future research, but remain far from large-scale adoption. Demonstration of truly scalable surface treatment patterning methods, such as roll-to-roll deposition of omniphobic background modifiers and wettable channel materials, will be necessary to fulfill their promise to be inexpensive, disposable devices.

Another interesting research direction could leverage the potential for controllability of fluids within devices. Selective deposition of the photoactive TiO_2-containing ink in combination with the hydrophobic-oleophilic ink could be used to fabricate a selectively photo-responsive device, perhaps for an on-demand separation process. Selective exposure to ultraviolet light through a simple mask could also be utilized for sequential activation of fluidic valves, for example, and may be necessary for more complex assays that require sequential addition of reagents at set times rather than the simple single-step mixing of two reagents followed by colorimetric detection demonstrated in Section 6.5.

While the nanostructured silicon open-channel devices in Chapter 8 successfully demonstrated precise, microscale confinement of low-surface-tension liquids, they have production costs and

scalability comparable to conventional PDMS closed-channel microfluidic devices rather than paper-based devices. An application needs to be developed that leverages their fundamentally unique aspects, most notably, a large liquid-air interface and the confinement of low-surface-tension liquids. A likely route may be to utilize the flow-focusing emulsification design to carry out a confined reaction or assay within water-in-oil droplets that requires the presence of oxygen or another gaseous reagent. Alternatively, the fabrication of an organ-on-a-chip device that requires long-term maintenance of a living tissue could be significantly simpler on an open device.

10.4 Spheroidal Culture on Superhydrophobic Surfaces

The spheroidal culture substrate in Chapter 9 is a promising proof-of-concept design, but will require significant development. In addition to the validation experiments for stability and functionality already discussed in the chapter, the need for large-scale production and ease of use will demand reduction of part complexity to that of the commercial hanging drop plates. An improved geometry could confine each droplet in a conical well with a single hole at the base for imaging purposes, which should improve stability and reliability. It could be possible to stamp this geometry in a single operation from a sheet of aluminum, prior to the etching/boiling/silanization process already discussed. More scalable bottom-up deposition methods for hierarchical texture on injection-molded plates could also be considered, such as hydrothermal synthesis of nanowires as discussed in Chapter 2.

The potential to grow spheroids in stable droplets on low-hysteresis superhydrophobic surfaces opens the potential to deliberately agitate droplets during growth, while maintaining localization of small initial cell populations. This could potentially accelerate the formation of tightly-packed spheroidal clusters. Inducing liquid flows within the media droplet due to motion may also be useful for simulating physiologically relevant conditions, such as those experienced by free-floating malignant cancer cells in the bloodstream or in ascites.

10.5 Closing Remarks

On the whole, the field of liquid- and solid- repellent surfaces remains full of fascinating engineering challenges and open scientific questions, as we continue to aim for an ideal surface that remains unaffected by virtually all substances and resists virtually all damage. The work in this thesis represents only a small part of a global effort towards that goal, and the exceptionally high demand for these repellent surfaces in all walks of life ensures that this research area will remain highly active for the foreseeable future.

REFERENCES

1. B. Bhushan and Y. C. Jung. Natural and Biomimetic Artificial Surfaces for Superhydrophobicity, Self-cleaning, Low Adhesion, and Drag Reduction. *Progress in Materials Science* **56** (1) (2011), 1–108. doi: 10.1016/j.pmatsci.2010.04.003.

2. G. McHale, M. I. Newton, and N. J. Shirtcliffe. Immersed Superhydrophobic Surfaces: Gas Exchange, Slip and Drag Reduction Properties. *Soft Matter* **6** (4) (2010), 714. doi: 10.1039/b917861a.

3. Y. Liu, Z. Liu, Y. Liu, H. Hu, Y. Li, P. Yan, B. Yu, and F. Zhou. One-Step Modification of Fabrics with Bioinspired Polydopamine@Octadecylamine Nanocapsules for Robust and Healable Self-Cleaning Performance. *Small* **11** (4) (2014), 426–431. doi: 10.1002/smll.201402383.

4. A. K. Kota, G. Kwon, W. Choi, J. M. Mabry, and A. Tuteja. Hygro Responsive Membranes for Effective Oil-Water Separation. *Nature Communications* **3** (2012), 1025. doi: 10.1038/ncomms2027.

5. A. Tuteja, W. Choi, M. L. Ma, J. M. Mabry, S. A. Mazzella, G. C. Rutledge, G. H. McKinley, and R. E. Cohen. Designing Superoleophobic Surfaces. *Science* **318** (5856) (2007), 1618–1622. doi: 10.1126/science.1148326.

6. A. Tuteja, W. Choi, G. H. McKinley, R. E. Cohen, and M. F. Rubner. Design Parameters for Superhydrophobicity and Superoleophobicity. *MRS Bulletin* **33** (8) (2008), 752. doi: 10.1557/mrs2008.161.

7. J. D. Smith, R. Dhiman, S. Anand, E. Reza-Garduno, R. E. Cohen, G. H. McKinley, and K. K. Varanasi. Droplet Mobility on Lubricant-Impregnated Surfaces. *Soft Matter* **9** (6) (2013), 1772–1780. doi: 10.1039/c2sm27032c.

8. T. S. Wong, S. H. Kang, S. K. Tang, E. J. Smythe, B. D. Hatton, A. Grinthal, and J. Aizenberg. Bioinspired Self-repairing Slippery Surfaces with Pressure-stable Omniphobicity. *Nature* **477** (7365) (2011), 443–447. doi: 10.1038/nature10447.

9. M. J. Owen and D. E. Williams. Surface Modification by Fluoroalkyl-functional Silanes. *Journal of Adhesion Science and Technology* **5** (4) (1991), 307–320. doi: 10.1163/156856191X00378.

10. E. F. Hare, E. G. Shafrin, and W. A. Zisman. Properties of Films of Adsorbed Fluorinated Acids. *The Journal of Physical Chemistry* **58** (3) (1954), 236–239. doi: 10.1021/j150513a011.

11. C. Urata, B. Masheder, D. F. Cheng, and A. Hozumi. Unusual Dynamic Dewetting Behavior of Smooth Perfluorinated Hybrid Films: Potential Advantages over Conventional Textured and Liquid-Infused Perfluorinated Surfaces. *Langmuir* **29** (40) (2013), 12472–12482. doi: 10.1021/la402714s.

12. H. Hu, G. Liu, and J. Wang. Clear and Durable Epoxy Coatings that Exhibit Dynamic Omniphobicity. *Advanced Materials Interfaces* **3** (14) (2016), 1600001. doi: 10.1002/admi.201600001.

13. L. Yu, G. Y. Chen, H. Xu, and X. Liu. Substrate-Independent, Transparent Oil-Repellent Coatings with Self-Healing and Persistent Easy-Sliding Oil Repellency. *ACS Nano* **10** (1) (2016), 1076–1085. doi: 10.1021/acsnano.5b06404.

14. T. Young. An Essay on the Cohesion of Fluids. *Philosophical Transactions of the Royal Society of London* **95** (0) (1805), 65–87. doi: 10.1098/rstl.1805.0005.

15. J. J. Jasper. The Surface Tension of Pure Liquid Compounds. *Journal of Physical and Chemical Reference Data* **1** (4) (1972), 841–1010. doi: 10.1063/1.3253106.

16. J. R. Rumble, ed. *CRC Handbook of Chemistry and Physics*. 98th. CRC Press, Taylor & Francis Group, 2017.

17. H.-J. Butt, K. Graf, and M. Kappl. *Physics and Chemistry of Interfaces*. 3rd. Weinheim, Germany: Wiley-VCH, 2013.

18. Diversified Enterprises, Inc. *Tables of Polymer Surface Characteristics*. 2018. url: https://www.accudynetest.com/polymer_tables.html.

19. S. Fordham. On the Calculation of Surface Tension from Measurements of Pendant Drops. *Proceedings of the Royal Society of London A: Mathematical, Physical and Engineering Sciences* **194** (1036) (1948), 1–16. doi: 10.1098/rspa.1948.0063.

20. E. Y. Arashiro and N. R. Demarquette. Use of the Pendant Drop Method to Measure Interfacial Tension between Molten Polymers. *Materials Research* **2** (1999), 23–32. doi: 10.1590/S1516-14391999000100005.

21. F. Schulman and W. A. Zisman. The Spreading of Liquids on Low-Energy Surfaces. V. Perfluorodecanoic Acid Monolayers. *Journal of Colloid Science* **7** (5) (1952), 465–481. doi: 10.1016/0095-8522(52)90030-5.

22. M. Barquins and J. Cognard. Adhesion Characteristics of Gold Surfaces. *Gold Bulletin* **19** (3) (1986), 82–86. doi: 10.1007/BF03214647.

23. M. Takenaga, S. Jo, M. Graupe, and T. R. Lee. Effective Van Der Waals Surface Energy of Self-Assembled Monolayer Films Having Systematically Varying Degrees of Molecular Fluorination. *Journal of Colloid and Interface Science* **320** (1) (2008), 264–7. doi: 10.1016/j.jcis.2007.12.048.

24. D. W. Grainger and C. W. Stewart. Fluorinated Coatings and Films: Motivation and Significance. *Fluorinated Surfaces, Coatings, and Films*. 2001. Chap. 1, pp. 1–14. doi: 10.1021/bk-2001-0787.ch001.

25. H. B. Eral, D. J. C. M. 't Mannetje, and J. M. Oh. Contact Angle Hysteresis: A Review of Fundamentals and Applications. *Colloid and Polymer Science* **291** (2) (2013), 247–260. doi: 10.1007/s00396-012-2796-6.

26. L. Gao and T. J. McCarthy. Contact Angle Hysteresis Explained. *Langmuir* **22** (14) (2006), 6234–6237. doi: 10.1021/la060254j.

27. R. E. Johnson and R. H. Dettre. Contact Angle Hysteresis: I. Study of an Idealized Rough Surface. *Contact Angle, Wettability, and Adhesion*. Ed. by F. M. Fowkes. Vol. 43. ACS Advances in Chemistry. Washington, D.C.: American Chemical Society, 1964. Chap. 7, pp. 112–135. doi: 10.1021/ba-1964-0043.ch007.

28. A. Marmur. Wetting on Hydrophobic Rough Surfaces: To Be Heterogeneous or Not to Be? *Langmuir* **19** (20) (2003), 8343–8348. doi: 10.1021/la0344682.

29. A. Marmur. Thermodynamic Aspects of Contact Angle Hysteresis. *Advances in Colloid and Interface Science* **50** (1994), 121–141. doi: 10.1016/0001-8686(94)80028-6.

30. J. Drelich. Guidelines to Measurements of Reproducible Contact Angles Using a Sessile-Drop Technique. *Surface Innovations* **1** (4) (2013), 248–254. doi: 10.1680/si.13.00010.

31. G. Macdougall and C. Ockrent. Surface Energy Relations in Liquid/Solid Systems I. the Adhesion of Liquids to Solids and a New Method of Determining the Surface Tension of Liquids. *Proceedings of the Royal Society of London A: Mathematical, Physical and Engineering Sciences* **180** (981) (1942), 151–173. doi: 10.1098/rspa.1942.0031.

32. C. Furmidge. Studies at Phase Interfaces. I. the Sliding of Liquid Drops on Solid Surfaces and a Theory for Spray Retention. *Journal of Colloid Science* **17** (4) (1962), 309–324. doi: 10.1016/0095-8522(62)90011-9.

33. R. N. Wenzel. Resistance of Solid Surfaces to Wetting by Water. *Industrial & Engineering Chemistry* **28** (8) (1936), 988–994. doi: 10.1021/ie50320a024.

34. X. Dai, B. B. Stogin, S. Yang, and T.-S. Wong. Slippery Wenzel State. *ACS Nano* **9** (9) (2015), 9260–9267. doi: 10.1021/acsnano.5b04151.

35. A. B. D. Cassie and S. Baxter. Wettability of Porous Surfaces. *Transactions of the Faraday Society* **40** (0) (1944), 546–551. doi: 10.1039/tf9444000546.

36. G. McHale. Cassie and Wenzel: Were They Really So Wrong? *Langmuir* **23** (15) (2007), 8200–8205. doi: 10.1021/LA7011167.

37. D. Quéré. Rough Ideas on Wetting. *Physica A: Statistical Mechanics and its Applications* **313** (1) (2002), 32–46. doi: 10.1016/S0378-4371(02)01033-6.

38. S. Shibuichi, T. Yamamoto, T. Onda, and K. Tsujii. Super Water- and Oil-Repellent Surfaces Resulting from Fractal Structure. *Journal of Colloid and Interface Science* **208** (1) (1998), 287–294. doi: 10.1006/jcis.1998.5813.

39. A. Ahuja, J. A. Taylor, V. Lifton, A. A. Sidorenko, T. R. Salamon, E. J. Lobaton, P. Kolodner, and T. N. Krupenkin. Nanonails A Simple Geometrical Approach to Electrically Tunable Superlyophobic Surfaces. *Langmuir* **24** (1) (2008), 9–14. doi: 10.1021/la702327z.

40. A. Tuteja, W. Choi, J. M. Mabry, G. H. McKinley, and R. E. Cohen. Robust Omniphobic Surfaces. *Proceedings of the National Academy of Sciences* **105** (47) (2008), 18200–18205. doi: 10.1073/pnas.0804872105.

41. L. Cao, H.-H. Hu, and D. Gao. Design and Fabrication of Micro-textures for Inducing a Superhydrophobic Behavior on Hydrophilic Materials. *Langmuir* **23** (8) (2007), 4310–4314. doi: 10.1021/la063572r.

42. L. Cao, T. P. Price, M. Weiss, and D. Gao. Super Water- and Oil-Repellent Surfaces on Intrinsically Hydrophilic and Oleophilic Porous Silicon Films. *Langmuir* **24** (5) (2008), 1640–1643. doi: 10.1021/la703401f.

43. T. Liu and C.-J. Kim. Repellent Surfaces. Turning a Surface Superrepellent Even to Completely Wetting Liquids. *Science* **346** (6213) (2014), 1096–1100. doi: 10.1126/science.1254787.

44. W. Barthlott and C. Neinhuis. Purity of the Sacred Lotus, or Escape from Contamination in Biological Surfaces. *Planta* **202** (1) (1997), 1–8. doi: 10.1007/s004250050096.

45. K. Koch and W. Barthlott. Superhydrophobic and Superhydrophilic Plant Surfaces: An Inspiration for Biomimetic Materials. *Philosophical Transactions. Series A, Mathematical, Physical, and Engineering Sciences* **367** (1893) (2009), 1487–509. doi: 10.1098/rsta.2009.0022.

46. K. Koch, H. F. Bohn, and W. Barthlott. Hierarchically Sculptured Plant Surfaces and Superhydrophobicity. *Langmuir* **25** (24) (2009), 14116–14120. doi: 10.1021/la9017322.

47. A. K. Kota, Y. Li, J. M. Mabry, and A. Tuteja. Hierarchically Structured Superoleophobic Surfaces with Ultralow Contact Angle Hysteresis. *Advanced Materials* **24** (43) (2012), 5838–5843. doi: 10.1002/adma.201202554.

48. Q. S. Zheng, Y. Yu, and Z. H. Zhao. Effects of Hydraulic Pressure on the Stability and Transition of Wetting Modes of Superhydrophobic Surfaces. *Langmuir* **21** (26) (2005), 12207–12212. doi: 10.1021/la052054y.

49. T. Deng, K. K. Varanasi, M. Hsu, N. Bhate, C. Keimel, J. Stein, and M. Blohm. Nonwetting of Impinging Droplets on Textured Surfaces. *Applied Physics Letters* **94** (13) (2009), 133109. doi: 10.1063/1.3110054.

50. K. Murugadoss, P. Dhar, and S. K. Das. Role and Significance of Wetting Pressures during Droplet Impact on Structured Superhydrophobic Surfaces. *The European Physical Journal E* **40** (1) (2017), 1. doi: 10.1140/epje/i2017-11491-x.

51. L. Wang and T. J. McCarthy. Covalently Attached Liquids: Instant Omniphobic Surfaces with Unprecedented Repellency. *Angewandte Chemie International Edition* **55** (1) (2016), 244–248. doi: 10.1002/anie.201509385.

52. D. F. Cheng, C. Urata, M. Yagihashi, and A. Hozumi. A Statically Oleophilic but Dynamically Oleophobic Smooth Nonperfluorinated Surface. *Angewandte Chemie International Edition* **51** (12) (2012), 2956–2959. doi: 10.1002/anie.201108800.

53. Y. Wang and X. Gong. Special Oleophobic and Hydrophilic Surfaces: Approaches, Mechanisms, and Applications. *Journal of Materials Chemistry A* **5** (8 2017), 3759–3773. doi: 10.1039/C6TA10474F.

54. P.-G. de Gennes, F. Brochard-Wyart, and D. Quéré. *Capillarity and Wetting Phenomena: Drops, Bubbles, Pearls, Waves*. Springer, 2004. doi: 10.1007/978-0-387-21656-0.

55. M. Nosonovsky and B. Bhushan. Lotus Versus Rose: Biomimetic Surface Effects. *Green Tribology: Biomimetics, Energy Conservation and Sustainability*. Ed. by M. Nosonovsky and B. Bhushan. Berlin, Heidelberg: Springer Berlin Heidelberg, 2012, pp. 25–40. doi: 10.1007/978-3-642-23681-5_2.

56. B. Mockenhaupt, H.-J. Ensikat, M. Spaeth, and W. Barthlott. Superhydrophobicity of Biological and Technical Surfaces under Moisture Condensation: Stability in Relation to Surface Structure. *Langmuir* **24** (23) (2008), 13591–13597. doi: 10.1021/la802351h.

57. X. Deng, L. Mammen, H.-J. Butt, and D. Vollmer. Candle Soot as a Template for a Transparent Robust Superamphiphobic Coating. *Science* **335** (6064) (2012), 67–70. doi: 10.1126/science.1207115.

58. Z. Chu and S. Seeger. Superamphiphobic Surfaces. *Chemical Society Reviews* **43** (8) (2014), 2784. doi: 10.1039/c3cs60415b.

59. A. J. Meuler, S. S. Chhatre, A. R. Nieves, J. M. Mabry, R. E. Cohen, and G. H. McKinley. Examination of Wettability and Surface Energy in Fluorodecyl POSS/Polymer Blends. *Soft Matter* **7** (21) (2011), 10122. doi: 10.1039/c1sm05994g.

60. K. Golovin, D. H. Lee, J. M. Mabry, and A. Tuteja. Transparent, Flexible, Superomniphobic Surfaces with Ultra-Low Contact Angle Hysteresis. *Angewandte Chemie International Edition* **52** (49) (2013), 13007–13011. doi: 10.1002/anie.201307222.

61. A. R. Bielinski, M. Boban, Y. He, E. Kazyak, D. H. Lee, C. Wang, A. Tuteja, and N. P. Dasgupta. Rational Design of Hyperbranched Nanowire Systems for Tunable Superomniphobic Surfaces Enabled by Atomic Layer Deposition. *ACS Nano* **11** (1) (2016), 478–489. doi: 10.1021/acsnano.6b06463.

62. T. Maitra, C. Antonini, M. Auf der Mauer, C. Stamatopoulos, M. K. Tiwari, and D. Poulikakos. Hierarchically Nanotextured Surfaces Maintaining Superhydrophobicity Under Severely Adverse Conditions. *Nanoscale* **6** (15) (2014), 8710–8719. doi: 10.1039/c4nr01368a.

63. K. Rykaczewski, W. A. Osborn, J. Chinn, M. L. Walker, J. H. J. Scott, W. Jones, C. Hao, S. Yao, and Z. Wang. How Nanorough is Rough Enough to Make a Surface Superhydrophobic During Water Condensation? *Soft Matter* **8** (33) (2012), 8786. doi: 10.1039/c2sm25502b.

64. L. Shen, W. Qiu, B. Liu, and Q. Guo. Stable Superhydrophobic Surface Based on Silicone Combustion Product. *RSC Advances* **4** (99) (2014), 56259–56262. doi: 10.1039/c4ra10838h.

65. T. Verho, C. Bower, P. Andrew, S. Franssila, O. Ikkala, and R. H. Ras. Mechanically Durable Superhydrophobic Surfaces. *Advanced Materials* **23** (5) (2011), 673–678. doi: 10.1002/adma.201003129.

66. F. Wang, S. Yu, J. Ou, M. Xue, and W. Li. Mechanically Durable Superhydrophobic Surfaces Prepared by Abrading. *Journal of Applied Physics* **114** (12) (2013), 124902. doi: 10.1063/1.4822028.

67. L. Wu, J. Zhang, B. Li, L. Fan, L. Li, and A. Wang. Facile Preparation of Super Durable Superhydrophobic Materials. *Journal of Colloid and Interface Science* **432** (2014), 31–42. doi: 10.1016/j.jcis.2014.06.046.

68. X. Zhu, Z. Zhang, X. Men, J. Yang, K. Wang, X. Xu, X. Zhou, and Q. Xue. Robust Superhydrophobic Surfaces with Mechanical Durability and Easy Repairability. *Journal of Materials Chemistry* **21** (39) (2011), 15793. doi: 10.1039/c1jm12513c.

69. Y. Lu, S. Sathasivam, J. Song, C. Crick, C. Carmalt, and I. Parkin. Robust Self-Cleaning Surfaces that Function when Exposed to Either Air or Oil. *Science* **347** (6226) (2015), 1132–1135. doi: 10.1126/science.aaa0946.

70. T. Sun, L. Feng, X. Gao, and L. Jiang. Bioinspired Surfaces with Special Wettability. *Accounts of Chemical Research* **38** (8) (2005), 644–652. doi: 10.1021/ar040224c.

71. J. Genzer and K. Efimenko. Recent Developments in Superhydrophobic Surfaces and Their Relevance to Marine Fouling: A Review. *Biofouling* **22** (5) (2006), 339–360. doi: 10.1080/08927010600980223.

72. B. Leng, Z. Shao, G. de With, and W. Ming. Superoleophobic Cotton Textiles. *Langmuir* **25** (4) (2009), 2456–2460. doi: 10.1021/la8031144.

73. C. Lee and C.-J. Kim. Underwater Restoration and Retention of Gases on Superhydrophobic Surfaces for Drag Reduction. *Physical Review Letters* **106** (1) (2011), 014502. doi: 10.1103/PhysRevLett.106.014502.

74. S. Pan, A. K. Kota, J. M. Mabry, and A. Tuteja. Superomniphobic Surfaces for Effective Chemical Shielding. *Journal of the American Chemical Society* **135** (2) (2013), 578–581. doi: 10.1021/ja310517s.

75. G. Kwon, A. K. Kota, Y. Li, A. Sohani, J. M. Mabry, and A. Tuteja. On-Demand Separation of Oil-Water Mixtures. *Advanced Materials* **24** (27) (2012), 3666–3671. doi: 10.1002/adma.201201364.

76. Y. Su, B. Ji, K. Zhang, H. Gao, Y. Huang, and K. Hwang. Nano to Micro Structural Hierarchy Is Crucial for Stable Superhydrophobic and Water-Repellent Surfaces. *Langmuir* **26** (7) (2010), 4984–4989. doi: 10.1021/la9036452.

77. A. K. Kota, G. Kwon, and A. Tuteja. The Design and Applications of Superomniphobic Surfaces. *NPG Asia Materials* **6** (7) (2014), e109. doi: 10.1038/am.2014.34.

78. D. Wu, J.-N. Wang, S.-Z. Wu, Q.-D. Chen, S. Zhao, H. Zhang, H.-B. Sun, and L. Jiang. Three-Level Biomimetic Rice-Leaf Surfaces with Controllable Anisotropic Sliding. *Advanced Functional Materials* **21** (15) (2011), 2927–2932. doi: 10.1002/adfm.201002733.

79. J.-Y. Lee, S. Pechook, D.-J. Jeon, B. Pokroy, and J.-S. Yeo. Three-Dimensional Triple Hierarchy Formed by Self-Assembly of Wax Crystals on CuO Nanowires for Nonwettable Surfaces. *ACS Applied Materials & Interfaces* **6** (7) (2014), 4927–4934. doi: 10.1021/am4059759.

80. M. J. Bierman and S. Jin. Potential Applications of Hierarchical Branching Nanowires in Solar Energy Conversion. *Energy & Environmental Science* **2** (10) (2009), 1050–1059. doi: 10.1039/B912095E.

81. H. J. Fan, P. Werner, and M. Zacharias. Semiconductor Nanowires: From Self-Organization to Patterned Growth. *Small* **2** (6) (2006), 700–717. doi: 10.1002/smll.200500495.

82. J. F. C. Jr, L. Stecker, and Y. Ono. Directed assembly of ZnO nanowires on a Si substrate without a metal catalyst using a patterned ZnO seed layer. *Nanotechnology* **16** (2) (2005), 292. doi: 10.1088/0957-4484/16/2/020.

83. X. Jiang, B. Tian, J. Xiang, F. Qian, G. Zheng, H. Wang, L. Mai, and C. M. Lieber. Rational Growth of Branched Nanowire Heterostructures with Synthetically Encoded Properties and Function. *Proceedings of the National Academy of Sciences* **108** (30) (2011), 12212–12216. doi: 10.1073/pnas.1108584108.

84. K. A. Dick, K. Deppert, M. W. Larsson, T. Mårtensson, W. Seifert, L. R. Wallenberg, and L. Samuelson. Synthesis of Branched Nanotrees by Controlled Seeding of Multiple Branching Events. *Nature Materials* **3** (6) (2004), 380–384. doi: 10.1038/nmat1133.

85. J. Zhu, H. Peng, A. F. Marshall, D. M. Barnett, W. D. Nix, and Y. Cui. Formation of Chiral Branched Nanowires by the Eshelby Twist. *Nature Nanotechnology* **3** (8) (2008), 477–481. doi: 10.1038/nnano.2008.179.

86. J.-S. Na, B. Gong, G. Scarel, and G. N. Parsons. Surface Polarity Shielding and Hierarchical ZnO Nano-Architectures Produced Using Sequential Hydrothermal Crystal Synthesis and Thin Film Atomic Layer Deposition. *ACS Nano* **3** (10) (2009), 3191–3199. doi: 10.1021/nn900702e.

87. D. J. Milliron, S. M. Hughes, Y. Cui, L. Manna, J. Li, L.-W. Wang, and A. Paul Alivisatos. Colloidal Nanocrystal Heterostructures with Linear and Branched Topology. *Nature* **430** (6996) (2004), 190–195. doi: 10.1038/nature02695.

88. K. Miszta, J. Graaf, G. Bertoni, D. Dorfs, R. Brescia, S. Marras, L. Ceseracciu, R. Cingolani, R. Roij, M. Dijkstra, and L. Manna. Hierarchical Self-assembly of Suspended Branched Colloidal Nanocrystals into Superlattice Structures. *Nature Materials* **10** (11) (2011), 872–876. doi: 10.1038/nmat3121.

89. S. Xu and Z. L. Wang. One-Dimensional ZnO Nanostructures: Solution Growth and Functional Properties. *Nano Research* **4** (11) (2011), 1013–1098. doi: 10.1007/s12274-011-0160-7.

90. C. Liu, J. Tang, H. M. Chen, B. Liu, and P. Yang. A Fully Integrated Nanosystem of Semiconductor Nanowires for Direct Solar Water Splitting. *Nano Letters* **13** (6) (2013), 2989–2992. doi: 10.1021/nl401615t.

91. S. H. Ko, D. Lee, H. W. Kang, K. H. Nam, J. Y. Yeo, S. J. Hong, C. P. Grigoropoulos, and H. J. Sung. Nanoforest of Hydrothermally Grown Hierarchical ZnO Nanowires for a High Efficiency Dye-Sensitized Solar Cell. *Nano Letters* **11** (2) (2011), 666–671. doi: 10.1021/nl1037962.

92. J. Y. Lao, J. G. Wen, and Z. F. Ren. Hierarchical ZnO Nanostructures. *Nano Letters* **2** (11) (2002), 1287–1291. doi: 10.1021/nl025753t.

93. N. P. Dasgupta, C. Liu, S. Andrews, F. B. Prinz, and P. Yang. Atomic Layer Deposition of Platinum Catalysts on Nanowire Surfaces for Photoelectrochemical Water Reduction. *Journal of the American Chemical Society* **135** (35) (2013), 12932–12935. doi: 10.1021/ja405680p.

94. D. Wang, F. Qian, C. Yang, Z. Zhong, and C. M. Lieber. Rational Growth of Branched and Hyperbranched Nanowire Structures. *Nano Letters* **4** (5) (2004), 871–874. doi: 10.1021/nl049728u.

95. M. Nosonovsky. Multiscale Roughness and Stability of Superhydrophobic Biomimetic Interfaces. *Langmuir* **23** (6) (2007), 3157–3161. doi: 10.1021/la062301d.

96. S. M. George. Atomic Layer Deposition: An Overview. *Chemical Reviews* **110** (1) (2009), 111–131. doi: 10.1021/cr900056b.

97. N. P. Dasgupta, S. Neubert, W. Lee, O. Trejo, J.-R. Lee, and F. B. Prinz. Atomic Layer Deposition of Al-doped ZnO Films: Effect of Grain Orientation on Conductivity. *Chemistry of Materials* **22** (16) (2010), 4769–4775. doi: 10.1021/cm101227h.

98. J. W. Elam, D. Routkevitch, P. P. Mardilovich, and S. M. George. Conformal Coating on Ultrahigh-Aspect-Ratio Nanopores of Anodic Alumina by Atomic Layer Deposition. *Chemistry of Materials* **15** (18) (2003), 3507–3517. doi: 10.1021/cm0303080.

99. A. R. Bielinski, E. Kazyak, C. M. Schlepütz, H. J. Jung, K. N. Wood, and N. P. Dasgupta. Hierarchical ZnO Nanowire Growth with Tunable Orientations on Versatile Substrates Using Atomic Layer Deposition Seeding. *Chemistry of Materials* **27** (13) (2015), 4799–4807. doi: 10.1021/acs.chemmater.5b01624.

100. L. E. Greene, M. Law, D. H. Tan, M. Montano, J. Goldberger, G. Somorjai, and P. Yang. General Route to Vertical ZnO Nanowire Arrays Using Textured ZnO Seeds. *Nano Letters* **5** (7) (2005), 1231–1236. doi: 10.1021/nl050788p.

101. H. Zhao, K. C. Park, and K. Y. Law. Effect of Surface Texturing on Superoleophobicity, Contact Angle Hysteresis, and "Robustness". *Langmuir* **28** (42) (2012), 14925–14934. doi: 10.1021/la302765t.

102. K. Golovin, M. Boban, J. M. Mabry, and A. Tuteja. Designing Self-Healing Superhydrophobic Surfaces with Exceptional Mechanical Durability. *ACS Applied Materials & Interfaces* **9** (12) (2017), 11212–11223. doi: 10.1021/acsami.6b15491.

103. M. Im, H. Im, J.-H. Lee, J.-B. Yoon, and Y.-K. Choi. A Robust Superhydrophobic and Superoleophobic Surface with Inverse-Trapezoidal Microstructures on a Large Transparent Flexible Substrate. *Soft Matter* **6** (7) (2010), 1401. doi: 10.1039/b925970h.

104. X. Tian, T. Verho, and R. H. Ras. Moving Superhydrophobic Surfaces Toward Real-World Applications. *Science* **352** (6282) (2016), 142–143. doi: 10.1126/science.aaf2073.

105. W. Jiang, H. Liu, L. Wang, S. Zhu, L. Yin, Y. Shi, B. Chen, Y. Ding, and N. An. An Effective Route for Transparent and Superhydrophobic Coating with High Mechanical Stability. *Thin Solid Films* **562** (2014), 383–388. doi: 10.1016/j.tsf.2014.04.085.

106. Y. Zhang, D. Ge, and S. Yang. Spray-Coating of Superhydrophobic Aluminum Alloys with Enhanced Mechanical Robustness. *Journal of Colloid and Interface Science* **423** (2014), 101–107. doi: 10.1016/j.jcis.2014.02.024.

107. A. Tolga, T. S. John, R. L. Andrew, M. T. Rosa, E. J. Gerald, N. I. Ilia, J. P. Stephen, A. H. Daniel, O. W. Kyle, K. C. David, R. H. Scott, and J. A. Haynes. Optically Transparent, Mechanically Durable, Nanostructured Superhydrophobic Surfaces Enabled by Spinodally Phase-Separated Glass Thin Films. *Nanotechnology* **24** (31) (2013), 315602. doi: 10.1088/0957-4484/24/31/315602.

108. Y. Li, S. Chen, M. Wu, and J. Sun. All Spraying Processes for the Fabrication of Robust, Self-Healing, Superhydrophobic Coatings. *Advanced Materials* **26** (20) (2014), 3344–3348. doi: 10.1002/adma.201306136.

109. H. Wang, Y. Xue, J. Ding, L. Feng, X. Wang, and T. Lin. Durable, Self-Healing Superhydrophobic and Superoleophobic Surfaces From Fluorinated-Decyl Polyhedral Oligomeric Silsesquioxane and Hydrolyzed Fluorinated Alkyl Silane. *Angewandte Chemie International Edition* **50** (48) (2011), 11433–11436. doi: 10.1002/anie.201105069.

110. L. Chen, X. Sun, J. Hang, L. Jin, D. Shang, and L. Shi. Large-Scale Fabrication of Robust Superhydrophobic Coatings with High Rigidity and Good Flexibility. *Advanced Materials Interfaces* **3** (6) (2016), 1500718. doi: 10.1002/admi.201500718.

111. D. Infante, K. W. Koch, P. Mazumder, L. Tian, A. Carrilero, D. Tulli, D. Baker, and V. Pruneri. Durable, Superhydrophobic, Antireflection, and Low Haze Glass Surfaces Using Scalable Metal Dewetting Nanostructuring. *Nano Research* **6** (6) (2013), 429–440. doi: 10.1007/s12274-013-0320-z.

112. J.-H. Li, R. Weng, X.-Q. Di, and Z.-W. Yao. Gradient and Weather Resistant Hybrid Super-Hydrophobic Coating Based on Fluorinated Epoxy Resin. *Journal of Applied Polymer Science* **131** (20) (2014), 40955–40962. doi: 10.1002/app.40955.

113. S. Barthwal, Y. S. Kim, and S. H. Lim. Mechanically Robust Superamphiphobic Aluminum Surface with Nanopore-Embedded Microtexture. *Langmuir* **29** (38) (2013), 11966–11974. doi: 10.1021/la402600h.

114. E. J. Lee, J. J. Kim, and S. O. Cho. Fabrication of Porous Hierarchical Polymer/Ceramic Composites by Electron Irradiation of Organic/Inorganic Polymers: Route to a Highly Durable, Large-Area Superhydrophobic Coating. *Langmuir* **26** (5) (2010), 3024–3030. doi: 10.1021/la100094y.

115. F. Su and K. Yao. Facile Fabrication of Superhydrophobic Surface with Excellent Mechanical Abrasion and Corrosion Resistance on Copper Substrate by a Novel Method. *ACS Applied Materials & Interfaces* **6** (11) (2014), 8762–8770. doi: 10.1021/am501539b.

116. L. Yin, J. Yang, Y. Tang, L. Chen, C. Liu, H. Tang, and C. Li. Mechanical Durability of Superhydrophobic and Oleophobic Copper Meshes. *Applied Surface Science* **316** (2014), 259–263. doi: 10.1016/j.apsusc.2014.08.002.

117. B. P. Dyett, A. H. Wu, and R. N. Lamb. Mechanical Stability of Surface Architecture-Consequences for Superhydrophobicity. *ACS Applied Materials & Interfaces* **6** (21) (2014), 18380–18394. doi: 10.1021/am505487r.

118. A. C. C. Esteves, Y. Luo, M. W. P. van de Put, C. C. M. Carcouët, and G. de With. Self-Replenishing Dual Structured Superhydrophobic Coatings Prepared by Drop-Casting of an All-In-One Dispersion. *Advanced Functional Materials* **24** (7) (2014), 986–992. doi: 10.1002/adfm.201301909.

119. J. Ma, X. Y. Zhang, D. P. Wang, D. Q. Zhao, D. W. Ding, K. Liu, and W. H. Wang. Superhydrophobic Metallic Glass Surface with Superior Mechanical Stability and Corrosion Resistance. *Applied Physics Letters* **104** (17) (2014), 173701. doi: 10.1063/1.4874275.

120. M. J. Nine, M. A. Cole, L. Johnson, D. N. Tran, and D. Losic. Robust Superhydrophobic Graphene-Based Composite Coatings with Self-Cleaning and Corrosion Barrier Properties. *ACS Applied Materials & Interfaces* **7** (51) (2015), 28482–28493. doi: 10.1021/acsami.5b09611.

121. B. Chen, J. Qiu, E. Sakai, N. Kanazawa, R. Liang, and H. Feng. Robust and Superhydrophobic Surface Modification by a "Paint + Adhesive" Method: Applications in Self-Cleaning after Oil Contamination and Oil-Water Separation. *ACS Applied Materials & Interfaces* **8** (27) (2016), 17659–17667. doi: 10.1021/acsami.6b04108.

122. W. S. Wong, Z. H. Stachurski, D. R. Nisbet, and A. Tricoli. Ultra-Durable and Transparent Self-Cleaning Surfaces by Large-Scale Self-Assembly of Hierarchical Interpenetrated Polymer Networks. *ACS Applied Materials & Interfaces* **8** (21) (2016), 13615–13623. doi: 10.1021/acsami.6b03414.

123. R. Yuan, S. Wu, P. Yu, B. Wang, L. Mu, X. Zhang, Y. Zhu, B. Wang, H. Wang, and J. Zhu. Superamphiphobic and Electroactive Nanocomposite toward Self-Cleaning, Antiwear, and Anticorrosion Coatings. *ACS Applied Materials & Interfaces* **8** (19) (2016), 12481–12493. doi: 10.1021/acsami.6b03961.

124. D. Gong, J. Long, D. Jiang, P. Fan, H. Zhang, L. Li, and M. Zhong. Robust and Stable Transparent Superhydrophobic Polydimethylsiloxane Films by Duplicating via a Femtosecond Laser-Ablated Template. *ACS Applied Materials & Interfaces* **8** (27) (2016), 17511–17518. doi: 10.1021/acsami.6b03424.

125. A. Steele, B. K. Nayak, A. Davis, M. C. Gupta, and E. Loth. Linear Abrasion of a Titanium Superhydrophobic Surface Prepared by Ultrafast Laser Microtexturing. *Journal of Micromechanics and Microengineering* **23** (11) (2013), 115012. doi: 10.1088/0960-1317/23/11/115012.

126. X. Tian, S. Shaw, K. R. Lind, and L. Cademartiri. Thermal Processing of Silicones for Green, Scalable, and Healable Superhydrophobic Coatings. *Advanced Materials* **28** (19) (2016), 3677–3682. doi: 10.1002/adma.201506446.

127. T. Lv, Z. Cheng, E. Zhang, H. Kang, Y. Liu, and L. Jiang. Self-Restoration of Superhydrophobicity on Shape Memory Polymer Arrays with Both Crushed Microstructure and Damaged Surface Chemistry. *Small* **13** (4) (2016), 1503402. doi: 10.1002/smll.201503402.

128. J. M. Mabry, A. Vij, S. T. Iacono, and B. D. Viers. Fluorinated Polyhedral Oligomeric Silsesquioxanes (F-POSS). *Angewandte Chemie International Edition* **120** (22) (2008), 4205–4208. doi: 10.1002/ange.200705355.

129. A. J. Guenthner, K. R. Lamison, L. M. Lubin, T. S. Haddad, and J. M. Mabry. Hansen Solubility Parameters for Octahedral Oligomeric Silsesquioxanes. *Industrial & Engineering Chemistry Research* **51** (38) (2012), 12282–12293. doi: 10.1021/ie300767p.

130. C. M. Hansen. *Hansen Solubility Parameters : A User's Handbook*. 2nd. Boca Raton: CRC Press, 2007, p. 519. doi: 10.1201/9781420006834.

131. J. Thimmasetty, C. V. S. Subrahmanyam, P. R. Sathesh Babu, M. A. Maulik, and B. A. Viswanath. Solubility Behavior of Pimozide in Polar and Nonpolar Solvents: Partial Solubility Parameters Approach. *Journal of Solution Chemistry* **37** (10) (2008), 1365–1378. doi: 10.1007/s10953-008-9317-8.

132. B. L. Karger, L. R. Snyder, and C. Eon. Expanded Solubility Parameter Treatment for Classification and Use of Chromatographic Solvents and Adsorbents. *Analytical Chemistry* **50** (14) (1978), 2126–2136. doi: 10.1021/ac50036a044.

133. F. Bottiglione and G. Carbone. Role of Statistical Properties of Randomly Rough Surfaces in Controlling Superhydrophobicity. *Langmuir* **29** (2) (2013), 599–609. doi: 10.1021/la304072p.

134. J. P. Davim, ed. *Surface Integrity in Machining*. London: Springer, 2010. doi: 10.1007/978-1-84882-874-2.

135. D. J. Whitehouse. *Surfaces and Their Measurement*. Jordan Hill, GBR: Butterworth-Heinemann, 2002.

136. J. Bico, U. Thiele, and D. Quéré. Wetting of Textured Surfaces. *Colloid Surface A* **206** (1-3) (2002), 41–46. doi: 10.1016/S0927-7757(02)00061-4.

137. R. Tadmor. Line Energy and the Relation between Advancing, Receding, and Young Contact Angles. *Langmuir* **20** (18) (2004), 7659–7664. doi: 10.1021/la049410h.

138. F. Guo, X. Su, G. Hou, and P. Li. Bioinspired Fabrication of Stable and Robust Superhydrophobic Steel Surface with Hierarchical Flowerlike Structure. *Colloids and Surfaces A: Physicochemical and Engineering Aspects* **401** (2012), 61–67. doi: 10.1016/j.colsurfa.2012.03.013.

139. J. Yang, Z. Zhang, X. Xu, X. Men, X. Zhu, and X. Zhou. Superoleophobic Textured Aluminum Surfaces. *New Journal of Chemistry* **35** (11) (2011), 2422. doi: 10.1039/c1nj20401g.

140. R. Campos, A. J. Guenthner, A. J. Meuler, A. Tuteja, R. E. Cohen, G. H. McKinley, T. S. Haddad, and J. M. Mabry. Superoleophobic Surfaces through Control of Sprayed-On Stochastic Topography. *Langmuir* **28** (25) (2012), 9834–9841. doi: 10.1021/la301480s.

141. H. Hertz. On the Contact of Elastic Solids. *Journal für die reine und angewandte Mathematik* **92** (1882), 156–171.

142. ASTM. D412 Standard Test Methods for Vulcanized Rubber and Thermoplastic Elastomers - Tension (2016). doi: 10.1520/D0412-16.

143. S. P. Kobaku, A. K. Kota, D. H. Lee, J. M. Mabry, and A. Tuteja. Patterned Superomniphobic-Superomniphilic Surfaces: Templates for Site-Selective Self-Assembly. *Angewandte Chemie International Edition* **51** (40) (2012), 10109–10113. doi: 10.1002/anie.201202823.

144. ASTM. B117-16 Standard Practice for Operating Salt Spray (Fog) Apparatus (2016).

145. M. Reyssat, A. Pépin, F. Marty, Y. Chen, and D. Quéré. Bouncing Transitions on Microtextured Materials. *Europhysics Letters* **74** (2) (2006), 306–312. doi: 10.1209/epl/i2005-10523-2.

146. R. Di Mundo, F. Bottiglione, and G. Carbone. Cassie State Robustness of Plasma Generated Randomly Nano-Rough Surfaces. *Applied Surface Science* **316** (2014), 324–332. doi: 10.1016/j.apsusc.2014.07.184.

147. J. W. Gose, K. Golovin, M. Boban, J. M. Mabry, A. Tuteja, M. Perlin, and S. L. Ceccio. Characterization of Superhydrophobic Surfaces for Drag Reduction in Turbulent Flow. *Journal of Fluid Mechanics* **845** (2018), 560–580. doi: 10.1017/jfm.2018.210.

148. K. B. Golovin, J. W. Gose, M. Perlin, S. L. Ceccio, and A. Tuteja. Bioinspired Surfaces for Turbulent Drag Reduction. *Philosophical Transactions. Series A, Mathematical, Physical, and Engineering Sciences* **374** (2073) (2016), 20160189. doi: 10.1098/rsta.2016.0189.

149. B. Streeter. Global Marine Fuel Trends 2030. *Mari-Tech 2014 Conference Proceedings*. Niagra Falls, ON, CA, 2014, 1–17.

150. S. A. Mäkiharju, M. Perlin, and S. L. Ceccio. On the Energy Economics of Air Lubrication Drag Reduction. *International Journal of Naval Architecture and Ocean Engineering* **4** (4) (2012), 412–422. doi: 10.2478/ijnaoe-2013-0107.

151. S. L. Ceccio. Friction Drag Reduction of External Flows with Bubble and Gas Injection. *Annual Review of Fluid Mechanics* **42** (1) (2010), 183–203. doi: 10.1146/annurev-fluid-121108-145504.

152. M. Perlin, D. R. Dowling, and S. L. Ceccio. Freeman Scholar Review: Passive and Active Skin-Friction Drag Reduction in Turbulent Boundary Layers. *Journal of Fluids Engineering* **138** (9) (2016), 091104. doi: 10.1115/1.4033295.

153. R. A. Bidkar, L. Leblanc, A. J. Kulkarni, V. Bahadur, S. L. Ceccio, and M. Perlin. Skin-friction Drag Reduction in the Turbulent Regime Using Random-textured Hydrophobic Surfaces. *Physics of Fluids* **26** (8) (2014), 85108. doi: 10.1063/1.4892902.

154. D. M. Bushnell and K. J. Moore. Drag Reduction in Nature. *Annual Review of Fluid Mechanics* **23** (1991), 65–79. doi: 10.1146/annurev.fluid.23.1.65.

155. R. Garcia-Mayoral and J. Jimenez. Drag Reduction by Riblets. *Philosophical Transactions. Series A, Mathematical, Physical, and Engineering Sciences* **369** (1940) (2011), 1412–1427. doi: 10.1098/rsta.2010.0359.

156. Y. C. Jung and B. Bhushan. Biomimetic Structures for Fluid Drag Reduction in Laminar and Turbulent Flows. *Journal of Physics: Condensed Matter* **22** (3) (2010), 35104. doi: 10.1088/0953-8984/22/3/035104.

157. J.-p. Zhao, X.-d. Du, and X.-h. Shi. Experimental Research on Friction-reduction with Super-hydrophobic Surfaces. *Journal of Marine Science and Application* **6** (3) (2007), 58–61. doi: 10.1007/s11804-007-7007-3.

158. K. Watanabe and H. Udagawa. Drag Reduction of Non-newtonian Fluids in a Circular Pipe with a Highly Water-repellent Wall. *AIChE Journal* **47** (2) (2001), 256–262. doi: 10.1002/aic.690470204.

159. J. P. Rothstein. Slip on Superhydrophobic Surfaces. *Annual Review of Fluid Mechanics* **42** (1) (2010), 89–109. doi: 10.1146/annurev-fluid-121108-145558.

160. B. R. K. Gruncell, N. D. Sandham, and G. McHale. Simulations of Laminar Flow Past a Superhydrophobic Sphere with Drag Reduction and Separation Delay. *Physics of Fluids* **25** (4) (2013), 43601. doi: 10.1063/1.4801450.

161. A. Busse, N. D. Sandham, G. McHale, and M. I. Newton. Change in Drag, Apparent Slip and Optimum Air Layer Thickness for Laminar Flow Over an Idealised Superhydrophobic Surface. *Journal of Fluid Mechanics* **727** (5) (2013), 488–508. doi: 10.1017/jfm.2013.284.

162. G. D. Bixler and B. Bhushan. Fluid Drag Reduction with Shark-Skin Riblet Inspired Microstructured Surfaces. *Advanced Functional Materials* **23** (36) (2013), 4507–4528. doi: 10.1002/adfm.201203683.

163. G. D. Bixler and B. Bhushan. Bioinspired Micro/Nanostructured Surfaces for Oil Drag Reduction in Closed Channel Flow. *Soft Matter* **9** (5) (2013), 1620–1635. doi: 10.1039/c2sm27070f.

164. G. D. Bixler and B. Bhushan. Shark Skin Inspired Low-Drag Microstructured Surfaces in Closed Channel Flow. *Journal of Colloid and Interface Science* **393** (2013), 384–396. doi: 10.1016/j.jcis.2012.10.061.

165. D. Jing and B. Bhushan. Boundary Slip of Superoleophilic, Oleophobic, and Superoleophobic Surfaces Immersed in Deionized Water, Hexadecane, and Ethylene Glycol. *Langmuir* **29** (47) (2013), 14691–14700. doi: 10.1021/la4030876.

166. S. Srinivasan, W. Choi, K.-C. Park, S. S. Chhatre, R. E. Cohen, and G. H. McKinley. Drag Reduction for Viscous Laminar Flow on Spray-coated Non-wetting Surfaces. *Soft Matter* **9** (24) (2013), 5691. doi: 10.1039/c3sm50445j.

167. S. Srinivasan, J. A. Kleingartner, J. B. Gilbert, R. E. Cohen, A. J. B. Milne, and G. H. McKinley. Sustainable Drag Reduction in Turbulent Taylor-Couette Flows by Depositing Sprayable Superhydrophobic Surfaces. *Physical Review Letters* **114** (1) (2015), 14501. doi: 10.1103/PhysRevLett.114.014501.

168. R. J. Daniello, N. E. Waterhouse, and J. P. Rothstein. Drag Reduction in Turbulent Flows Over Superhydrophobic Surfaces. *Physics of Fluids* **21** (8) (2009), 85103. doi: 10.1063/1.3207885.

169. B. Woolford, J. Prince, D. Maynes, and B. W. Webb. Particle Image Velocimetry Characterization of Turbulent Channel Flow with Rib Patterned Superhydrophobic Walls. *Physics of Fluids* **21** (8) (2009), 85106. doi: 10.1063/1.3213607.

170. E. Aljallis, M. A. Sarshar, R. Datla, V. Sikka, A. Jones, and C.-H. Choi. Experimental Study of Skin Friction Drag Reduction on Superhydrophobic Flat Plates in High Reynolds Number Boundary Layer Flow. *Physics of Fluids* **25** (2) (2013), 25103. doi: 10.1063/1.4791602.

171. C. Henoch, T. Krupenkin, P. Kolodner, J. Taylor, M. Hodes, A. Lyons, P. Charles, and K. Breuer. Turbulent Drag Reduction Using Superhydrophobic Surfaces. *3rd AIAA Flow Control Conference*. American Institute of Aeronautics and Astronautics, 2006, 1–5. doi: 10.2514/6.2006-319210.2514/6.2006-3192.

172. H. Park, G. Sun, and C.-J. Kim. Superhydrophobic Turbulent Drag Reduction As a Function of Surface Grating Parameters. *Journal of Fluid Mechanics* **747** (2014), 722–734. doi: 10.1017/jfm.2014.151.

173. M. P. Schultz and K. A. Flack. The Rough-Wall Turbulent Boundary Layer from the Hydraulically Smooth to the Fully Rough Regime. *Journal of Fluid Mechanics* **580** (2007), 381–405. doi: 10.1017/S0022112007005502.

174. U. O. Ünal, B. Ünal, and M. Atlar. Turbulent Boundary Layer Measurements Over Flat Surfaces Coated by Nanostructured Marine Antifoulings. *Experiments in Fluids* **52** (6) (2012), 1431–1448. doi: 10.1007/s00348-012-1262-z.

175. H. Schlichting and K. Gersten. *Boundary-Layer Theory*. Grenzschicht-Theorie.English. Berlin, Heidelberg: Springer, 2017, xxiii, 799 p. doi: 10.1007/978-3-662-52919-5.

176. M. Boban, K. Golovin, B. Tobelmann, O. Gupte, J. M. Mabry, and A. Tuteja. Smooth, All-Solid, Low-Hysteresis, Omniphobic Surfaces with Enhanced Mechanical Durability. *ACS Applied Materials & Interfaces* **10** (14) (2018), 11406–11413. doi: 10.1021/acsami.8b00521.

177. A. Milionis, I. S. Bayer, and E. Loth. Recent Advances in Oil-Repellent Surfaces. *International Materials Reviews* **61** (2) (2016), 101–126. doi: 10.1080/09506608.2015.1116492.

178. J. D. Smith, A. J. Meuler, H. L. Bralower, R. Venkatesan, S. Subramanian, R. E. Cohen, G. H. McKinley, and K. K. Varanasi. Hydrate-phobic Surfaces: Fundamental Studies in Clathrate Hydrate Adhesion Reduction. *Physical Chemistry Chemical Physics* **14** (17) (2012), 6013. doi: 10.1039/c2cp40581d.

179. X. Li, D. R. Ballerini, and W. Shen. A Perspective on Paper-Based Microfluidics: Current Status and Future Trends. *Biomicrofluidics* **6** (1) (2012), 11301–11313. doi: 10.1063/1.3687398.

180. D. P. Sanders. Advances in Patterning Materials for 193 nm Immersion Lithography. *Chemical Reviews* **110** (1) (2010), 321–60. doi: 10.1021/cr900244n.

181. K. Choi, A. H. Ng, R. Fobel, and A. R. Wheeler. Digital Microfluidics. *Annual Review of Analytical Chemistry* **5** (2012), 413–440. doi: 10.1146/annurev-anchem-062011-143028.

182. S. Anand, A. T. Paxson, R. Dhiman, J. D. Smith, and K. K. Varanasi. Enhanced Condensation on Lubricant-Impregnated Nanotextured Surfaces. *ACS Nano* **6** (11) (2012), 10122–10129. doi: 10.1021/nn303867y.

183. D. Attinger, C. Frankiewicz, A. R. Betz, T. M. Schutzius, R. Ganguly, A. Das, C.-J. Kim, and C. M. Megaridis. Surface Engineering For Phase Change Heat Transfer: A Review. *MRS Energy & Sustainability* **1** (2014), E4. doi: 10.1557/mre.2014.9.

184. W. Li and A. Amirfazli. Hierarchical Structures for Natural Superhydrophobic Surfaces. *Soft Matter* **4** (3) (2008), 462–466. doi: 10.1039/B715731B.

185. R. Hensel, C. Neinhuis, and C. Werner. The Springtail Cuticle As a Blueprint for Omniphobic Surfaces. *Chemical Society Reviews* **45** (2 2016), 323–341. doi: 10.1039/C5CS00438A.

186. H. Jin, X. Tian, O. Ikkala, and R. H. A. Ras. Preservation of Superhydrophobic and Superoleophobic Properties upon Wear Damage. *ACS Applied Materials & Interfaces* **5** (3) (2013), 485–488. doi: 10.1021/am302541f.

187. P. S. Brown and B. Bhushan. Mechanically Durable, Superomniphobic Coatings Prepared by Layer-by-layer Technique for Self-cleaning and Anti-smudge. *Journal of Colloid and Interface Science* **456** (2015), 210–218. doi: 10.1016/j.jcis.2015.06.030.

188. A. Lafuma and D. Quéré. Slippery Pre-Suffused Surfaces. *EPL (Europhysics Letters)* **96** (5) (2011), 56001. doi: 10.1209/0295-5075/96/56001.

189. J. S. Wexler, I. Jacobi, and H. A. Stone. Shear-Driven Failure of Liquid-Infused Surfaces. *Physical Review Letters* **114** (16) (2015), 168301. doi: 10.1103/PhysRevLett.114.168301.

190. Y. Liu, J. S. Wexler, C. Schönecker, and H. A. Stone. Effect of Viscosity Ratio on the Shear-driven Failure of Liquid-infused Surfaces. *Physical Review Fluids* **1** (7 2016), 074003. doi: 10.1103/PhysRevFluids.1.074003.

191. D. Barriet. Fluorinated Self-Assembled Monolayers: Composition, Structure and Interfacial Properties. *Current Opinion in Colloid & Interface Science* **8** (3) (2003), 236–242. doi: 10.1016/s1359-0294(03)00054-2.

192. W. Chen, A. Y. Fadeev, M. C. Hsieh, D. Öner, J. Youngblood, and T. J. McCarthy. Ultrahydrophobic and Ultralyophobic Surfaces: Some Comments and Examples. *Langmuir* **15** (10) (1999), 3395–3399. doi: 10.1021/la990074s.

193. A. Ulman. Formation and Structure of Self-Assembled Monolayers. *Chemical Reviews* **96** (4) (1996), 1533–1554. doi: 10.1021/cr9502357.

194. C. Haensch, S. Hoeppener, and U. S. Schubert. Chemical Modification of Self-Assembled Silane Based Monolayers by Surface Reactions. *Chemical Society Reviews* **39** (6) (2010), 2323–2334. doi: 10.1039/B920491A.

195. S. S. Chhatre, J. O. Guardado, B. M. Moore, T. S. Haddad, J. M. Mabry, G. H. McKinley, and R. E. Cohen. Fluoroalkylated Silicon-Containing Surfaces: Estimation of Solid-Surface Energy. *ACS Applied Materials & Interfaces* **2** (12) (2010), 3544–54. doi: 10.1021/am100729j.

196. D. Anton. Surface-Fluorinated Coatings. *Advanced Materials* **10** (15) (1998), 1197–1205. doi: 10.1002/(sici)1521-4095(199810)10:15<1197::aid-adma1197>3.0.co;2-f.

197. C. Dorrer and J. Rühe. Some Thoughts on Superhydrophobic Wetting. *Soft Matter* **5** (1) (2009), 51–61. doi: 10.1039/b811945g.

198. K. Rykaczewski, A. T. Paxson, M. Staymates, M. L. Walker, X. Sun, S. Anand, S. Srinivasan, G. H. McKinley, J. Chinn, J. H. J. Scott, and K. K. Varanasi. Dropwise Condensation of Low Surface Tension Fluids on Omniphobic Surfaces. *Scientific Reports* **4** (2014), 661–667. doi: 10.1038/srep04158.

199. ASTM. D3359 Standard Test Methods for Measuring Adhesion by Tape Test (2016). doi: 10.1520/D3359-09E02.

200. M. P. Schultz, J. M. Walker, C. N. Steppe, and K. A. Flack. Impact of Diatomaceous Biofilms on the Frictional Drag of Fouling-release Coatings. *Biofouling* **31** (9-10) (2015), 759–773. doi: 10.1080/08927014.2015.1108407.

201. ASTM. D6540 - 12: Standard Test Method for Accelerated Soiling of Pile Yarn Floor Covering 1 (2012). doi: 10.1520/D6540-12.

202. M. J. Kreder, J. Alvarenga, P. Kim, and J. Aizenberg. Design of Anti-icing Surfaces: Smooth, Textured or Slippery? *Nature Reviews Materials* **1** (2016), 15003. doi: 10.1038/natrevmats.2015.3.

203. P. S. Brown and B. Bhushan. Durable, Superoleophobic Polymer-nanoparticle Composite Surfaces with Re-entrant Geometry Via Solvent-induced Phase Transformation. *Scientific Reports* **6** (2016), 21048. doi: 10.1038/srep21048.

204. T. P. Nhung Nguyen, P. Brunet, Y. Coffinier, and R. Boukherroub. Quantitative Testing of Robustness on Superomniphobic Surfaces by Drop Impact. *Langmuir* **26** (23) (2010), 18369–18373. doi: 10.1021/la103097y.

205. A. K. Kota, W. Choi, and A. Tuteja. Superomniphobic Surfaces: Design and Durability. *MRS Bulletin* **38** (05) (2013), 383–390. doi: 10.1557/mrs.2013.101.

206. S. M. Kang, S. M. Kim, H. N. Kim, M. K. Kwak, D. H. Tahk, and K. Y. Suh. Robust Superomniphobic Surfaces with Mushroom-Like Micropillar Arrays. *Soft Matter* **8** (33) (2012), 8563. doi: 10.1039/c2sm25879j.

207. A. T. Paxson, J. L. Yague, K. K. Gleason, and K. K. Varanasi. Stable Dropwise Condensation for Enhancing Heat Transfer Via the Initiated Chemical Vapor Deposition (icvd) of Grafted Polymer Films. *Advanced Materials* **26** (3) (2014), 418–423. doi: 10.1002/adma.201303065.

208. P. Kim, T. S. Wong, J. Alvarenga, M. J. Kreder, W. E. Adorno-Martinez, and J. Aizenberg. Liquid-Infused Nanostructured Surfaces with Extreme Anti-Ice and Anti-Frost Performance. *ACS Nano* **6** (8) (2012), 6569–6577. doi: 10.1021/nn302310q.

209. R. Dou, J. Chen, Y. Zhang, X. Wang, D. Cui, Y. Song, L. Jiang, and J. Wang. Anti-icing Coating with an Aqueous Lubricating Layer. *ACS Applied Materials & Interfaces* **6** (10) (2014), 6998–7003. doi: 10.1021/am501252u.

210. S. B. Subramanyam, K. Rykaczewski, and K. K. Varanasi. Ice Adhesion on Lubricant-impregnated Textured Surfaces. *Langmuir* **29** (44) (2013), 13414–13418. doi: 10.1021/la402456c.

211. H. Murase and K. Nanishi. On the Relationship of Thermodynamic and Physical Properties of Polymers with Ice Adhesion. *Annals of Glaciology* **6** (1985), 146–149. doi: 10.3189/1985AoG6-1-146-149.

212. P. Irajizad, M. Hasnain, N. Farokhnia, S. M. Sajadi, and H. Ghasemi. Magnetic Slippery Extreme Icephobic Surfaces. *Nature Communications* **7** (2016), 13395. doi: 10.1038/ncomms13395.

213. S. Ozbay, C. Yuceel, and H. Y. Erbil. Improved Icephobic Properties on Surfaces with a Hydrophilic Lubricating Liquid. *ACS Applied Materials & Interfaces* **7** (39) (2015), 22067–22077. doi: 10.1021/acsami.5b07265.

214. M. K. Chaudhury and K. H. Kim. Shear-induced Adhesive Failure of a Rigid Slab in Contact with a Thin Confined Film. *The European Physical Journal E: Soft Matter and Biological Physics* **23** (2) (2007), 175–183. doi: 10.1140/epje/i2007-10171-x.

215. K. Golovin, S. P. R. Kobaku, D. H. Lee, E. T. DiLoreto, J. M. Mabry, and A. Tuteja. Designing Durable Icephobic Surfaces. *Science Advances* **2** (3) (2016), e1501496–e1501496. doi: 10.1126/sciadv.1501496.

216. K. Kendall. The Adhesion and Surface Energy of Elastic Solids. *Journal of Physics D: Applied Physics* **4** (8) (1971), 320. doi: 10.1088/0022-3727/4/8/320.

217. D. L. Beemer, W. Wang, and A. K. Kota. Durable Gels with Ultra-Low Adhesion to Ice. *Journal of Materials Chemistry A* **1** (2016), 15003. doi: 10.1039/C6TA07262C.

218. C. Wang, T. Fuller, W. Zhang, and K. J. Wynne. Thickness Dependence of Ice Removal Stress for a Polydimethylsiloxane Nanocomposite: Sylgard 184. *Langmuir* **30** (43) (2014), 12819–12826. doi: 10.1021/la5030444.

219. A. J. Meuler, J. D. Smith, K. K. Varanasi, J. M. Mabry, G. H. McKinley, and R. E. Cohen. Relationships between Water Wettability and Ice Adhesion. *ACS Applied Materials & Interfaces* **2** (11) (2010), 3100–3110. doi: 10.1021/am1006035.

220. S. Chernyy, M. Järn, K. Shimizu, A. Swerin, S. U. Pedersen, K. Daasbjerg, L. Makkonen, P. Claesson, and J. Iruthayaraj. Superhydrophilic Polyelectrolyte Brush Layers with Imparted Anti-Icing Properties: Effect of Counter ions. *ACS Applied Materials & Interfaces* **6** (9) (2014), 6487–6496. doi: 10.1021/am500046d.

221. J. Chen, J. Liu, M. He, K. Li, D. Cui, Q. Zhang, X. Zeng, Y. Zhang, J. Wang, and Y. Song. Superhydrophobic Surfaces Cannot Reduce Ice Adhesion. *Applied Physics Letters* **101** (11) (2012), 111603. doi: 10.1063/1.4752436.

222. K. K. Varanasi, T. Deng, J. D. Smith, M. Hsu, and N. Bhate. Frost Formation and Ice Adhesion on Superhydrophobic Surfaces. *Applied Physics Letters* **97** (23) (2010), 234102. doi: 10.1063/1.3524513.

223. M. Nosonovsky and V. Hejazi. Why Superhydrophobic Surfaces Are Not Always Icephobic. *ACS Nano* **6** (10) (2012), 8488–8491. doi: 10.1021/nn302138r.

224. L. Gao and T. J. McCarthy. A Perfectly Hydrophobic Surface (θA/θR= 180°/180°). *Journal of the American Chemical Society* **128** (28) (2006), 9052–9053. doi: 10.1021/JA062943N.

225. A. Y. Fadeev and T. J. McCarthy. Trialkylsilane Monolayers Covalently Attached to Silicon Surfaces: Wettability Studies Indicating that Molecular Topography Contributes to Contact Angle Hysteresis. *Langmuir* **15** (11) (1999), 3759–3766. doi: 10.1021/LA981486O.

226. A. Y. Fadeev and T. J. McCarthy. Self-Assembly Is Not the Only Reaction Possible between Alkyltrichlorosilanes and Surfaces: Monomolecular and Oligomeric Covalently Attached Layers of Dichloro- and Trichloroalkylsilanes on Silicon. *Langmuir* **16** (18) (2000), 7268–7274. doi: 10.1021/la000471z.

227. D. H. Flagg and T. J. McCarthy. Rapid and Clean Covalent Attachment of Methylsiloxane Polymers and Oligomers to Silica Using B(C6F5)3 Catalysis. *Langmuir* **33** (33) (2017), 8129–8139. doi: 10.1021/acs.langmuir.7b01751.

228. J. N. Lee, C. Park, and G. M. Whitesides. Solvent Compatibility of Poly(dimethylsiloxane)-Based Microfluidic Devices. *Analytical Chemistry* **75** (23) (2003), 6544–6554. doi: 10.1021/ac0346712.

229. K. Efimenko, W. E. Wallace, and J. Genzer. Surface Modification of Sylgard-184 Poly(dimethyl siloxane) Networks by Ultraviolet and Ultraviolet/Ozone Treatment. *Journal of Colloid and Interface Science* **254** (2) (2002), 306–315. doi: 10.1006/jcis.2002.8594.

230. S. K. Thanawala and M. K. Chaudhury. Surface Modification of Silicone Elastomer Using Perfluorinated Ether. *Langmuir* **16** (3) (2000), 1256–1260. doi: 10.1021/la9906626.

231. M. Lee, N. Lee, J. Lim, J. Kim, M. Kim, H. Baik, and Y. Kim. Antiadhesion Surface Treatments of Molds for High-Resolution Unconventional Lithography. *Advanced Materials* **18** (23) (2006), 3115–3119. doi: 10.1002/adma.200601268.

232. D. L. Schmidt, R. F. Brady, K. Lam, D. C. Schmidt, and M. K. Chaudhury. Contact Angle Hysteresis, Adhesion, and Marine Biofouling. *Langmuir* **20** (7) (2004), 2830–2836. doi: 10.1021/la035385o.

233. J. E. Mark. *Polymer Data Handbook*. 2nd. Vol. 131. 44. Oxford ; New York: Oxford University Press, 2009, vii, 1250 p. doi: 10.1021/ja907879q.

234. C. Navier. Memoire Sur Les Lois Du Mouvement Des Fluides. *Mémoires de l'Académie (royale) des sciences de l'Institut (imperial) de France* **6** (1823), 389–440.

235. W. Ostwald. Ueber die rechnerische Darstellung des Strukturgebietes der Viskosität. *Kolloid-Zeitschrift* **47** (2) (1929), 176–187. doi: 10.1007/BF01496959.

236. D. Hadjistamov. Determination of the Onset of Shear Thinning of Polydimethylsiloxane. *Journal of Applied Polymer Science* **108** (4) (2008), 2356–2364. doi: 10.1002/app.27685.

237. T. Podgorski, J.-M. Flesselles, and L. Limat. Corners, Cusps, and Pearls in Running Drops. *Physical Review Letters* **87** (3) (2001), 036102. doi: 10.1103/PhysRevLett.87.036102.

238. R. P. Garrod, L. G. Harris, W. C. E. Schofield, J. McGettrick, L. J. Ward, D. O. H. Teare, and J. P. S. Badyal. Mimicking a Stenocara Beetle's Back for Microcondensation Using Plasmachemical Patterned Superhydrophobic-Superhydrophilic Surfaces. *Langmuir* **23** (2) (2007), 689–693. doi: 10.1021/la0610856.

239. H. Schmid and B. Michel. Siloxane Polymers for High-Resolution, High-Accuracy Soft Lithography. *Macromolecules* **33** (8) (2000), 3042–3049. doi: 10.1021/ma982034l.

240. T. W. Odom, J. C. Love, D. B. Wolfe, K. E. Paul, and G. M. Whitesides. Improved Pattern Transfer in Soft Lithography Using Composite Stamps. *Langmuir* **18** (13) (2002), 5314–5320. doi: 10.1021/la020169l.

241. Gelest Incorporated. *Gelest hPDMS 2-Part High Modulus Reprographic Silicone Elastomer (1:1 kit)*. url: https://www.gelest.com/wp-content/uploads/PP2-RG07-Gelest%C2%AE-hPDMS-TDS.pdf.

242. G. Li, L. Wang, H. Ni, and C. U. Pittman. Polyhedral Oligomeric Silsesquioxane (POSS) Polymers and Copolymers: A Review. *Journal of Inorganic and Organometallic Polymers* **11** (3) (2001), 123–154. doi: 10.1023/A:1015287910502.

243. L. Matějka, A. Strachota, J. Pleštil, P. Whelan, M. Steinhart, and M. Šlouf. Epoxy Networks Reinforced with Polyhedral Oligomeric Silsesquioxanes (POSS). Structure and Morphology. *Macromolecules* **37** (25) (2004), 9449–9456. doi: 10.1021/ma0484577.

244. L. Matějka, I. A. Kroutilová, J. Lichtenhan, and T. Haddad. Structure Ordering and Reinforcement in POSS Containing Hybrids. *European Polymer Journal* **52** (2014), 117–126. doi: 10.1016/j.eurpolymj.2014.01.005.

245. M. Tolinski. Overview of Fillers and Fibers. *Additives for Polyolefins*. Elsevier, 2009, pp. 93–119. doi: 10.1016/B978-0-8155-2051-1.00007-8.

246. V. Joshi, M. Srividhya, M. Dubey, A. K. Ghosh, and A. Saxena. Effect of Functionalization on Dispersion of POSS-silicone Rubber Nanocomposites. *Journal of Applied Polymer Science* **130** (1) (2013), 92–99. doi: 10.1002/app.39112.

247. D. Chen, J. Nie, S. Yi, W. Wu, Y. Zhong, J. Liao, and C. Huang. Thermal Behaviour and Mechanical Properties of Novel RTV Silicone Rubbers Using Divinyl-hexa[(trimethoxysilyl)ethyl]-POSS As Cross-linker. *Polymer Degradation and Stability* **95** (4) (2010), 618–626. doi: 10.1016/j.polymdegradstab.2009.12.002.

248. C. Li, M. Boban, S. A. Snyder, S. P. R. Kobaku, G. Kwon, G. Mehta, and A. Tuteja. Paper-Based Surfaces with Extreme Wettabilities for Novel, Open-Channel Microfluidic Devices. *Advanced Functional Materials* **26** (33) (2016), 6121–6131. doi: 10.1002/adfm.201601821.

249. J. P. Rolland and D. A. Mourey. Paper As a Novel Material Platform for Devices. *MRS Bulletin* **38** (4) (2013), 299–305. doi: 10.1557/mrs.2013.58.

250. A. W. Martinez, S. T. Phillips, M. J. Butte, and G. M. Whitesides. Patterned paper as a platform for inexpensive, low-volume, portable bioassays. *Angewandte Chemie International Edition* **46** (8) (2007), 1318–20. doi: 10.1002/anie.200603817.

251. P. N. Nge, C. I. Rogers, and A. T. Woolley. Advances in Microfluidic Materials, Functions, Integration, and Applications. *Chemical Reviews* **113** (4) (2013), 2550–2583. doi: 10.1021/cr300337x.

252. A. W. Martinez, S. T. Phillips, G. M. Whitesides, and E. Carrilho. Diagnostics for the Developing World: Microfluidic Paper-based Analytical Devices. *Analytical Chemistry* **82** (1) (2010), 3–10. doi: 10.1021/ac9013989.

253. A. W. Martinez. Microfluidic Paper-based Analytical Devices: From POCKET to Paper-based ELISA. *Bioanalysis* **3** (23) (2011), 2589–92. doi: 10.4155/bio.11.258.

254. X. Li, J. Tian, G. Garnier, and W. Shen. Fabrication of Paper-based Microfluidic Sensors by Printing. *Colloids and Surfaces B* **76** (2) (2010), 564–70. doi: 10.1016/j.colsurfb.2009.12.023.

255. D. M. Cate, J. A. Adkins, J. Mettakoonpitak, and C. S. Henry. Recent Developments in Paper-based Microfluidic Devices. *Analytical Chemistry* **87** (1) (2015), 19–41. doi: 10.1021/ac503968p.

256. E. Carrilho, A. W. Martinez, and G. M. Whitesides. Understanding Wax Printing A Simple Micropatterning Process for Paper Based Microfluidics. *Analytical Chemistry* **81** (16) (2009), 7091–7095. doi: 10.1021/ac901071p.

257. Z. Nie, C. A. Nijhuis, J. Gong, X. Chen, A. Kumachev, A. W. Martinez, M. Narovlyansky, and G. M. Whitesides. Electrochemical Sensing in Paper-based Microfluidic Devices. *Lab on a Chip* **10** (4) (2010), 477–83. doi: 10.1039/b917150a.

258. X. Li, J. Tian, T. Nguyen, and W. Shen. Paper-based Microfluidic Devices by Plasma Treatment. *Analytical Chemistry* **80** (23) (2008), 9131–4. doi: 10.1021/ac801729t.

259. J. Olkkonen, K. Lehtinen, and T. Erho. Flexographically Printed Fluidic Structures in Paper. *Analytical Chemistry* **82** (24) (2010), 10246–10250. doi: 10.1021/ac1027066.

260. D. M. Cate, W. Dungchai, J. C. Cunningham, J. Volckens, and C. S. Henry. Simple, Distance-Based Measurement for Paper Analytical Devices. *Lab on a Chip* **13** (12) (2013), 2397–404. doi: 10.1039/c3lc50072a.

261. M. Santhiago, J. B. Wydallis, L. T. Kubota, and C. S. Henry. Construction and Electrochemical Characterization of Microelectrodes for Improved Sensitivity in Paper-Based Analytical Devices. *Analytical Chemistry* **85** (10) (2013), 5233–9. doi: 10.1021/ac400728y.

262. A. W. Martinez, S. T. Phillips, and G. M. Whitesides. Three-Dimensional Microfluidic Devices Fabricated in Layered Paper and Tape. *Proceedings of the National Academy of Sciences of the United States of America* **105** (50) (2008), 19606–11. doi: 10.1073/pnas.0810903105.

263. A. W. Martinez, S. T. Phillips, Z. Nie, C. M. Cheng, E. Carrilho, B. J. Wiley, and G. M. Whitesides. Programmable Diagnostic Devices Made from Paper and Tape. *Lab on a Chip* **10** (19) (2010), 2499–504. doi: 10.1039/c0lc00021c.

264. G. G. Lewis, M. J. DiTucci, and S. T. Phillips. Quantifying Analytes in Paper-based Microfluidic Devices without Using External Electronic Readers. *Angewandte Chemie International Edition* **51** (51) (2012), 12707–12710. doi: 10.1002/anie.201207239.

265. K. M. Schilling, D. Jauregui, and A. W. Martinez. Paper and Toner Three-Dimensional Fluidic Devices: Programming Fluid Flow to Improve Point-of-Care Diagnostics. *Lab on a Chip* **13** (4) (2013), 628–31. doi: 10.1039/c2lc40984d.

266. H. Liu and R. M. Crooks. Three-Dimensional Paper Microfluidic Devices Assembled Using the Principles of Origami. *Journal of the American Chemical Society* **133** (44) (2011), 17564–17566. doi: 10.1021/ja2071779.

267. L. Ge, S. Wang, X. Song, S. Ge, and J. Yu. 3D Origami-Based Multifunction-integrated Immunodevice: Low-cost and Multiplexed Sandwich Chemiluminescence Immunoassay on Microfluidic Paper-based Analytical Device. *Lab on a Chip* **12** (17) (2012), 3150–8. doi: 10.1039/c2lc40325k.

268. A. K. Yetisen, M. S. Akram, and C. R. Lowe. Paper-Based Microfluidic Point-of-Care Diagnostic Devices. *Lab on a Chip* **13** (12) (2013), 2210–2251. doi: 10.1039/c3lc50169h.

269. J. L. Osborn, B. Lutz, E. Fu, P. Kauffman, D. Y. Stevens, and P. Yager. Microfluidics without Pumps: Reinventing the T-sensor and H-filter in Paper Networks. *Lab on a Chip* **10** (20) (2010), 2659–65. doi: 10.1039/c004821f.

270. E. Fu, S. A. Ramsey, P. Kauffman, B. Lutz, and P. Yager. Transport in Two-Dimensional Paper Networks. *Microfluidics and Nanofluidics* **10** (1) (2011), 29–35. doi: 10.1007/s10404-010-0643-y.

271. P. Spicar-Mihalic, B. Toley, J. Houghtaling, T. Liang, P. Yager, and E. Fu. CO_2 Laser Cutting and Ablative Etching for the Fabrication of Paper-based Devices. *Journal of Micromechanics and Microengineering* **23** (6) (2013), 067003. doi: 10.1088/0960-1317/23/6/067003.

272. P. Lisowski and P. K. Zarzycki. Microfluidic Paper-Based Analytical Devices (muPADs) and Micro Total Analysis Systems (muTAS): Development, Applications and Future Trends. *Chromatographia* **76** (2013), 1201–1214. doi: 10.1007/s10337-013-2413-y.

273. A. C. Glavan, R. V. Martinez, A. B. Subramaniam, H. J. Yoon, R. M. D. Nunes, H. Lange, M. M. Thuo, and G. M. Whitesides. Omniphobic "RFPaper" Produced by Silanization of Paper with Fluoroalkyltrichlorosilanes. *Advanced Functional Materials* **24** (1) (2014), 60–70. doi: 10.1002/adfm.201300780.

274. J. Wang, M. R. Monton, X. Zhang, C. D. Filipe, R. Pelton, and J. D. Brennan. Hydrophobic Sol-Gel Channel Patterning Strategies for Paper-based Microfluidics. *Lab on a Chip* **14** (4) (2014), 691–5. doi: 10.1039/c3lc51313k.

275. W. J. Lan, E. J. Maxwell, C. Parolo, D. K. Bwambok, A. B. Subramaniam, and G. M. Whitesides. Paper-Based Electroanalytical Devices with an Integrated, Stable Reference Electrode. *Lab on a Chip* **13** (20) (2013), 4103–8. doi: 10.1039/c3lc50771h.

276. X. Liu, Y. Liang, F. Zhou, and W. Liu. Extreme Wettability and Tunable Adhesion: Biomimicking beyond Nature? *Soft Matter* **8** (7) (2012), 2070–2086. doi: 10.1039/c1sm07003g.

277. G. Kwon, E. Post, and A. Tuteja. Membranes with Selective Wettability for the Separation of Oil-Water Mixtures. *MRS Communications* **5** (3) (2015), 475–494. doi: 10.1557/mrc.2015.61.

278. E. W. Washburn. The Dynamics of Capillary Flow. *Physical Review* **17** (3) (1921), 273–283. doi: 10.1103/PhysRev.17.273.

279. M. A. Croxen, R. J. Law, R. Scholz, K. M. Keeney, M. Wlodarska, and B. B. Finlay. Recent Advances in Understanding Enteric Pathogenic *Escherichia coli*. *Clinical Microbiology Reviews* **26** (4) (2013), 822–80. doi: 10.1128/CMR.00022-13.

280. S. R. Nugen and A. J. Baeumner. Trends and Opportunities in Food Pathogen Detection. *Analytical and Bioanalytical Chemistry* **391** (2) (2008), 451–4. doi: 10.1007/s00216-008-1886-2.

281. P. Tallon, B. Magajna, C. Lofranco, and K. T. Leung. Microbial Indicators of Faecal Contamination in Water: A Current Perspective. *Water, Air, and Soil Pollution* **166** (1) (2005), 139–166. doi: 10.1007/s11270-005-7905-4.

282. J. C. Jokerst, J. A. Adkins, B. Bisha, M. M. Mentele, L. D. Goodridge, and C. S. Henry. Development of a Paper-based Analytical Device for Colorimetric Detection of Select Foodborne Pathogens. *Analytical Chemistry* **84** (6) (2012), 2900–7. doi: 10.1021/ac203466y.

283. Y. Zhang, T. Ren, T. Li, J. He, and D. Fang. Paper-Based Hydrophobic/Lipophobic Surface for Sensing Applications Involving Aggressive Liquids. *Advanced Materials Interfaces* **3** (22) (2016), 1600672. doi: 10.1002/admi.201600672.

284. K. Yamada, T. G. Henares, K. Suzuki, and D. Citterio. Paper-Based Inkjet-printed Microfluidic Analytical Devices. *Angewandte Chemie International Edition* **54** (18) (2015), 5294–310. doi: 10.1002/anie.201411508.

285. V. Rajendra, C. Sicard, J. D. Brennan, and M. A. Brook. Printing Silicone-based Hydrophobic Barriers on Paper for Microfluidic Assays Using Low-cost Ink Jet Printers. *Analyst* **139** (24) (2014), 6361–5. doi: 10.1039/c4an01626b.

286. T. M. Schutzius, M. Elsharkawy, M. K. Tiwari, and C. M. Megaridis. Surface Tension Confined (STC) Tracks for Capillary-Driven Transport of Low Surface Tension Liquids. *Lab on a Chip* **12** (24) (2012), 5237–42. doi: 10.1039/c2lc40849j.

287. L. E. Scriven and C. V. Sternling. The Marangoni Effects. *Nature* **187** (4733) (1960), 186–188. doi: 10.1038/187186a0.

288. R. D. Deegan, O. Bakajin, T. F. Dupont, G. Huber, S. R. Nagel, and T. A. Witten. Capillary Flow As the Cause of Ring Stains from Dried Liquid Drops. *Nature* **389** (6653) (1997), 827–829. doi: 10.1038/39827.

289. A. Jobe and S. Bourgeois. Lac Represser-operator Interaction: VIII. Lactose Is an Anti-inducer of the Lac Operon. *Journal of Molecular Biology* **75** (2) (1973), 303–313. doi: 10.1016/0022-2836(73)90023-5.

290. A. C. Glavan, R. V. Martinez, E. J. Maxwell, A. B. Subramaniam, R. M. D. Nunes, S. Soh, and G. M. Whitesides. Rapid Fabrication of Pressure-Driven Open-Channel Microfluidic Devices in Omniphobic R^F Paper. *Lab on a Chip* **13** (15 2013), 2922–2930. doi: 10.1039/C3LC50371B.

291. A. Rompré, P. Servais, J. Baudart, M.-R. de-Roubin, and P. Laurent. Detection and Enumeration of Coliforms in Drinking Water: Current Methods and Emerging Approaches. *Journal of Microbiological Methods* **49** (1) (2002), 31–54. doi: 10.1016/S0167-7012(01)00351-7.

292. C. Li, M. Boban, and A. Tuteja. Open-Channel, Water-in-oil Emulsification in Paper-based Microfluidic Devices. *Lab on a Chip* **17** (8) (2017), 1436–1441. doi: 10.1039/c7lc00114b.

293. A. A. Darhuber, S. M. Troian, and W. W. Reisner. Dynamics of Capillary Spreading along Hydrophilic Microstripes. *Physical Review E - Statistical, Nonlinear, and Soft Matter Physics* **64** (3 Pt 1) (2001), 031603. doi: 10.1103/PhysRevE.64.031603.

294. B. Zhao, J. S. Moore, and D. J. Beebe. Surface-Directed Liquid Flow inside Microchannels. *Science* **291** (5506) (2001), 1023–1026. doi: 10.1126/science.291.5506.1023.

295. P. Lam, K. J. Wynne, and G. E. Wnek. Surface-Tension-Confined Microfluidics. *Langmuir* **18** (3) (2002), 948–951. doi: 10.1021/la010589v.

296. H. Y. Holman, R. Miles, Z. Hao, E. Wozei, L. M. Anderson, and H. Yang. Real-time Chemical Imaging of Bacterial Activity in Biofilms Using Open-channel Microfluidics and Synchrotron FTIR Spectromicroscopy. *Analytical Chemistry* **81** (20) (2009), 8564–70. doi: 10.1021/ac9015424.

297. K. Loutherback, L. Chen, and H. Y. Holman. Open-Channel Microfluidic Membrane Device for Long-term FT-IR Spectromicroscopy of Live Adherent Cells. *Analytical Chemistry* **87** (9) (2015), 4601–6. doi: 10.1021/acs.analchem.5b00524.

298. G. V. Kaigala, R. D. Lovchik, and E. Delamarche. Microfluidics in the "Open Space" for Performing Localized Chemistry on Biological Interfaces. *Angewandte Chemie International Edition* **51** (45) (2012), 11224–40. doi: 10.1002/anie.201201798.

299. D. J. Guckenberger, T. E. de Groot, A. M. Wan, D. J. Beebe, and E. W. Young. Micromilling: A Method for Ultra-Rapid Prototyping of Plastic Microfluidic Devices. *Lab on a Chip* **15** (11) (2015), 2364–78. doi: 10.1039/c5lc00234f.

300. E. Ueda and P. A. Levkin. Emerging Applications of Superhydrophilic-superhydrophobic Micropatterns. *Advanced Materials* **25** (9) (2013), 1234–1247. doi: 10.1002/adma.201204120.

301. E. K. Sackmann, A. L. Fulton, and D. J. Beebe. The Present and Future Role of Microfluidics in Biomedical Research. *Nature* **507** (7491) (2014), 181–9. doi: 10.1038/nature13118.

302. L. J. Barkal, A. B. Theberge, C. J. Guo, J. Spraker, L. Rappert, J. Berthier, K. A. Brakke, C. C. Wang, D. J. Beebe, N. P. Keller, and E. Berthier. Microbial Metabolomics in Open Microscale Platforms. *Nature Communications* **7** (2016), 10610. doi: 10.1038/ncomms10610.

303. S. Y. Teh, R. Lin, L. H. Hung, and A. P. Lee. Droplet Microfluidics. *Lab on a Chip* **8** (2) (2008), 198–220. doi: 10.1039/b715524g.

304. H. N. Joensson and H. Andersson Svahn. Droplet Microfluidics: A Tool for Single-cell Analysis. *Angewandte Chemie International Edition* **51** (49) (2012), 12176–12192. doi: 10.1002/anie.201200460.

305. R. K. Shah, H. C. Shum, A. C. Rowat, D. Lee, J. J. Agresti, A. S. Utada, L.-Y. Chu, J.-W. Kim, A. Fernandez-Nieves, C. J. Martinez, and D. A. Weitz. Designer Emulsions Using Microfluidics. *Materials Today* **11** (4) (2008), 18–27. doi: 10.1016/s1369-7021(08)70053-1.

306. S. L. Anna, N. Bontoux, and H. A. Stone. Formation of Dispersions Using "Flow Focusing" in Microchannels. *Applied Physics Letters* **82** (3) (2003), 364. doi: 10.1063/1.1537519.

307. R. Dreyfus, P. Tabeling, and H. Willaime. Ordered and Disordered Patterns in Two-Phase Flows in Microchannels. *Physical Review Letters* **90** (14) (2003), 144505. doi: 10.1103/PhysRevLett.90.144505.

308. D. Dendukuri and P. S. Doyle. The Synthesis and Assembly of Polymeric Microparticles Using Microfluidics. *Advanced Materials* **21** (41) (2009), 4071–4086. doi: 10.1002/adma.200803386.

309. E. Brouzes, M. Medkova, N. Savenelli, D. Marran, M. Twardowski, J. B. Hutchison, J. M. Rothberg, D. R. Link, N. Perrimon, and M. L. Samuels. Droplet Microfluidic Technology for Single-cell High-throughput Screening. *Proceedings of the National Academy of Sciences of the United States of America* **106** (34) (2009), 14195–200. doi: 10.1073/pnas.0903542106.

310. A. W. Martinez, S. T. Phillips, B. J. Wiley, M. Gupta, and G. M. Whitesides. FLASH: A Rapid Method for Prototyping Paper-based Microfluidic Devices. *Lab on a Chip* **8** (12) (2008), 2146–2150. doi: 10.1039/b811135a.

311. P. D. Haller, C. A. Flowers, and M. Gupta. Three-Dimensional Patterning of Porous Materials Using Vapor Phase Polymerization. *Soft Matter* **7** (6) (2011), 2428. doi: 10.1039/c0sm01214a.

312. M. P. Sousa and J. F. Mano. Superhydrophobic Paper in the Development of Disposable Labware and Lab-on-Paper Devices. *ACS Applied Materials & Interfaces* **5** (9) (2013), 3731–7. doi: 10.1021/am400343n.

313. R. Almeida and J. W. Kwon. Virtual Walls Based on Oil-Repellent Surfaces for Low-Surface-Tension Liquids. *Langmuir* **29** (4) (2013), 994–8. doi: 10.1021/la3040038.

314. D. Chandler. Interfaces and the Driving Force of Hydrophobic Assembly. *Nature* **437** (7059) (2005), 640–7. doi: 10.1038/nature04162.

315. B. P. Casavant, E. Berthier, A. B. Theberge, J. Berthier, S. I. Montanez-Sauri, L. L. Bischel, K. Brakke, C. J. Hedman, W. Bushman, N. P. Keller, and D. J. Beebe. Suspended Microfluidics. *Proceedings of the National Academy of Sciences of the United States of America* **110** (25) (2013), 10111–6. doi: 10.1073/pnas.1302566110.

316. C. Renault, X. Li, S. E. Fosdick, and R. M. Crooks. Hollow-channel Paper Analytical Devices. *Analytical Chemistry* **85** (16) (2013), 7976–9. doi: 10.1021/ac401786h.

317. A. Ghosh, R. Ganguly, T. M. Schutzius, and C. M. Megaridis. Wettability Patterning for High-rate, Pumpless Fluid Transport on Open, Non-planar Microfluidic Platforms. *Lab on a Chip* **14** (9) (2014), 1538–50. doi: 10.1039/c3lc51406d.

318. B. Gnapareddy, S. R. Dugasani, T. Ha, B. Paulson, T. Hwang, T. Kim, J. H. Kim, K. Oh, and S. H. Park. Chemical and Physical Characteristics of Doxorubicin Hydrochloride Drug-Doped Salmon DNA Thin Films. *Scientific Reports* **5** (2015), 12722. doi: 10.1038/srep12722.

319. O. Tacar, P. Sriamornsak, and C. R. Dass. Doxorubicin: An Update on Anticancer Molecular Action, Toxicity and Novel Drug Delivery Systems. *Journal of Pharmacy and Pharmacology* **65** (2) (2013), 157–70. doi: 10.1111/j.2042-7158.2012.01567.x.

320. D. Dendukuri, K. Tsoi, T. A. Hatton, and P. S. Doyle. Controlled Synthesis of Nonspherical Microparticles Using Microfluidics. *Langmuir* **21** (6) (2005), 2113–2116. doi: 10.1021/la047368k.

321. J. Shieh, S. Ravipati, F.-H. Ko, and K. Ostrikov. Plasma-made Silicon Nanograss and Related Nanostructures. *Journal of Physics D: Applied Physics* **44** (17) (2011), 174010. doi: 10.1088/0022-3727/44/17/174010.

322. M. Steglich, T. Käsebier, M. Zilk, T. Pertsch, E.-B. Kley, and A. Tünnermann. The Structural and Optical Properties of Black Silicon by Inductively Coupled Plasma Reactive Ion Etching. *Journal of Applied Physics* **116** (17) (2014), 173503. doi: 10.1063/1.4900996.

323. S. P. R. Kobaku, G. Kwon, A. K. Kota, R. G. Karunakaran, P. Wong, D. H. Lee, and A. Tuteja. Wettability Engendered Templated Self-assembly (WETS) for Fabricating Multiphasic Particles. *ACS Applied Materials & Interfaces* **7** (7) (2015), 4075–4080. doi: 10.1021/am507964k.

324. M. Vinci, S. Gowan, F. Boxall, L. Patterson, M. Zimmermann, W. Court, C. Lomas, M. Mendiola, D. Hardisson, and S. A. Eccles. Advances in Establishment and Analysis of Three-Dimensional Tumor Spheroid-based Functional Assays for Target Validation and Drug Evaluation. *BMC Biology* **10** (1) (2012), 29. doi: 10.1186/1741-7007-10-29.

325. S. Breslin and L. O'Driscoll. Three-Dimensional Cell Culture: The Missing Link in Drug Discovery. *Drug Discovery Today* **18** (5) (2013), 240–249. doi: 10.1016/j.drudis.2012.10.003.

326. J. W. Haycock. 3D Cell Culture: A Review of Current Approaches and Techniques. *3D Cell Culture: Methods and Protocols*. Ed. by J. W. Haycock. Totowa, NJ: Humana Press, 2011, pp. 1–15. doi: 10.1007/978-1-60761-984-0_1.

327. P. Mehta, C. Novak, S. Raghavan, M. Ward, and G. Mehta. Self-Renewal and CSCs In Vitro Enrichment: Growth as Floating Spheres. *Cancer Stem Cells: Methods and Protocols*. Ed. by G. Papaccio and V. Desiderio. New York, NY: Springer New York, 2018, pp. 61–75. doi: 10.1007/978-1-4939-7401-6_6.

328. S. Raghavan, P. Mehta, M. R. Ward, M. E. Bregenzer, E. M. A. Fleck, L. Tan, K. McLean, R. J. Buckanovich, and G. Mehta. Personalized Medicine–Based Approach to Model Patterns of Chemoresistance and Tumor Recurrence Using Ovarian Cancer Stem Cell Spheroids. *Clinical Cancer Research* **23** (22) (2017), 6934–6945. doi: 10.1158/1078-0432.ccr-17-0133.

329. F. Hirschhaeuser, H. Menne, C. Dittfeld, J. West, W. Mueller-Klieser, and L. A. Kunz-Schughart. Multicellular Tumor Spheroids: An Underestimated Tool Is Catching up Again. *Journal of Biotechnology* **148** (1) (2010), 3–15. doi: 10.1016/j.jbiotec.2010.01.012.

330. S. Raghavan, P. Mehta, E. N. Horst, M. R. Ward, K. R. Rowley, and G. Mehta. Comparative Analysis of Tumor Spheroid Generation Techniques for Differential in Vitro Drug Toxicity. *Oncotarget* **7** (13) (2016), 16948–16961. doi: 10.18632/oncotarget.7659.

331. E. Fennema, N. Rivron, J. Rouwkema, C. van Blitterswijk, and J. de Boer. Spheroid Culture As a Tool for Creating 3D Complex Tissues. *Trends in Biotechnology* **31** (2) (2013), 108–115. doi: 10.1016/j.tibtech.2012.12.003.

332. Y.-C. Tung, A. Y. Hsiao, S. G. Allen, Y.-s. Torisawa, M. Ho, and S. Takayama. High-throughput 3D Spheroid Culture and Drug Testing Using a 384 Hanging Drop Array. *Analyst* **136** (3 2011), 473–478. doi: 10.1039/C0AN00609B.

333. Y. Xue, S. Chu, P. Lv, and H. Duan. Importance of Hierarchical Structures in Wetting Stability on Submersed Superhydrophobic Surfaces. *Langmuir* **28** (25) (2012), 9440–9450. doi: 10.1021/la300331e.

334. M. Xu, G. Sun, and C.-J. Kim. Infinite Lifetime of Underwater Superhydrophobic States. *Physical Review Letters* **113** (13 2014), 136103. doi: 10.1103/PhysRevLett.113.136103.

335. P. R. Jones, X. Hao, E. R. Cruz-Chu, K. Rykaczewski, K. Nandy, T. M. Schutzius, K. K. Varanasi, C. M. Megaridis, J. H. Walther, P. Koumoutsakos, H. D. Espinosa, and N. A. Patankar. Sustaining Dry Surfaces Under Water. *Scientific Reports* **5** (1) (2015), 12311. doi: 10.1038/srep12311.

336. R. G. Karunakaran, C.-H. Lu, Z. Zhang, and S. Yang. Highly Transparent Superhydrophobic Surfaces from the Coassembly of Nanoparticles (≤ 100 nm). *Langmuir* **27** (8) (2011), 4594–4602. doi: 10.1021/la104067c.

337. Y. Rahmawan, L. Xu, and S. Yang. Self-Assembly of Nanostructures Towards Transparent, Superhydrophobic Surfaces. *Journal of Materials Chemistry A* **1** (9 2013), 2955–2969. doi: 10.1039/C2TA00288D.

338. J. Zhang and S. Seeger. Superoleophobic Coatings with Ultralow Sliding Angles Based on Silicone Nanofilaments. *Angewandte Chemie International Edition* **50** (29) (2011), 6652–6656. doi: 10.1002/anie.201101008.

339. B. I. Tarnowski, F. G. Spinale, and J. H. Nicholson. DAPI as a Useful Stain for Nuclear Quantitation. *Biotechnic & Histochemistry* **66** (6) (1991), 296–302. doi: 10.3109/10520299109109990.

340. E. C. W. Perryman. Grain Boundary Attack on Aluminum in Hydrochloric Acid and Sodium Hydroxide. *JOM: The Journal of The Minerals, Metals & Materials Society* **5** (7) (1953), 911–917. doi: 10.1007/BF03397566.

341. F. Zaera. Probing Liquid/Solid Interfaces at the Molecular Level. *Chemical Reviews* **112** (5) (2012), 2920–2986. doi: 10.1021/cr2002068.

342. B. P. Lloyd, P. N. Bartlett, and R. J. K. Wood. Active Gas Replenishment and Sensing of the Wetting State in a Submerged Superhydrophobic Surface. *Soft Matter* **13** (7) (2017), 1413–1419. doi: 10.1039/C6SM02820A.